

NON-CONVENTIONAL SOLUTIONS TO PHYSICAL AND  
ENGINEERING PROBLEMS FACING MICROFLUIDICS

Dissertation

zur Erlangung des Grades

des Doktors der Naturwissenschaften

der Naturwissenschaftlich- Technischen Fakultät

Der Universität des Saarlandes

von

Jonathan Soren O'Connor

Saarbrücken

2022

Tages des Kolloquiums: 17/08/2022

Dekan: Prof. Jörn Walter

Berichterstatter:

Prof. Andreas Manz

Prof. Dirk Bähre

Vorsitz: Prof. Michael Vielhaber

Akad. Mitarbeiter: Dr. Haibin Gao

## Abstract

Microfluidics is a vital tool for scientific research utilising micrometre scale features to provide unparalleled control of micro-, nano- and pico-litres of fluid. Planar lithographic design and fabrication techniques have become more versatile and refined over time. However, stagnation of novel designs, fabrication methodologies and experimental conditions is increasing due to the current limitations. 3D printing is approaching the resolution required in microfluidics, whilst also providing greater freedom of design, materials and fabrication techniques. This thesis seeks to overcome the traditional limitations using 3D printing to innovate design and production, enabling rapid prototyping methodologies and truly 3D structures, which are typically expensive and labour intensive.

The first system discussed within this work generates cells-laden gelatin microdroplets and featured heating and cooling water channels, with a performance comparative to commercial devices. Secondly, a flow cell for the screening of extracellular lectins via glycomimetic liposomes was produced. Additionally, stereolithographic printing was used to produce a bioinspired monolithic droplet generator which featured intertwined channels. Finally, a Van de Graaff generator-based electrophoresis system was developed, in order to generate record breaking separation resolutions whilst extended capillary lifespan compared to other experimental systems.



## Zusammenfassung

Die Mikrofluidik ist ein wichtiges Werkzeug für die wissenschaftliche Forschung, das Merkmale im Mikrometerbereich nutzt, um eine beispiellose Kontrolle von Mikro-, Nano- und Pikolitern von Flüssigkeiten zu ermöglichen. Planare lithografische Konstruktions- und Herstellungstechniken sind im Laufe der Zeit vielseitiger und verfeinert worden. Aufgrund der derzeitigen Einschränkungen nimmt jedoch die Stagnation neuartiger Designs, Herstellungsmethoden und experimenteller Bedingungen zu. Der 3D-Druck nähert sich der in der Mikrofluidik erforderlichen Auflösung und bietet gleichzeitig eine größere Freiheit bei Design, Materialien und Herstellungstechniken. Diese Dissertation versucht, die traditionellen Einschränkungen bei der Verwendung von 3D-Druck zu überwinden, um Design und Produktion zu erneuern und schnelle Prototyping-Methoden und echte 3D-Strukturen zu ermöglichen, die normalerweise teuer und arbeitsintensiv sind.

Das erste in dieser Arbeit diskutierte System erzeugt mit Zellen beladene Gelatine-Mikrotröpfchen und verfügt über Heiz- und Kühlwasserkanäle mit einer Leistung, die mit kommerziellen Geräten vergleichbar ist. Zweitens wurde eine Durchflusszelle für das Screening von extrazellulären Lektinen über glykomimetische Liposomen hergestellt. Darüber hinaus wurde stereolithografischer Druck verwendet, um einen bioinspirierten monolithischen Tröpfchengenerator herzustellen, der ineinander verschlungene Kanäle aufweist. Schließlich wurde ein auf einem Van-de-Graaff-Generator basierendes Elektrophoresesystem entwickelt, um rekordverdächtige Trennauflösungen zu erzeugen und gleichzeitig die Kapillarlebensdauer im Vergleich zu anderen experimentellen Systemen zu verlängern.



“A scientist in his laboratory is not a mere technician: he is also a child confronting natural phenomena that impress him as though they were fairy tales.”

Marie Curie

"Madame Curie: A Biography". Book by Eve Curie Labouisse, November 30, 1936

To my loving family and friends,

All my achievements are only possible because of your support.

Thank you now and forever.

&

In memory of Keith Sutton,

You saw an inquisitive yet frustrated child who struggled to verbalise himself to the world, but also saw the potential for a scientist. I just needed the encouragement and pointing in the right direction. I would have never started this journey of discovery and understanding if not for your teaching early in my life. While I will never be able to pay you back for the incredible effect you have had on my life, I promise to pay it forward for the rest of mine.

Thank you.

The research described in this dissertation was funded by KIST Europe GmbH.





## Contents

Chapter 1 – Introduction .....	1
1.1 Description of the current fabrication techniques .....	1
1.2 Advantages and disadvantages of current microfluidic processes .....	2
1.3 The promise of 3D printing.....	2
1.4 Research Question.....	2
1.5 Thesis structure .....	3
Chapter 2 – 3D printed moulds for the production of microgel liver cell encapsulation devices. .....	3
Chapter 3 – Rapidly prototyped 3D printed flow cell the screening of extracellular lectins via glycomimetic liposomes. ....	3
Chapter 4 – Three-dimensional bioinspired intertwining channel multiplexed droplet generator. ....	3
Chapter 5 – Development of an ultra-high voltage electrophoresis system using a Van de Graaff generator capable of $10^7$ theoretical plates.....	3
Chapter 2 – 3D printed moulds for the production of microgel liver cell encapsulation devices. ..	5
2.1 Abstract .....	5
2.2 Introduction.....	5
2.2.1 Bioassays.....	5
2.2.2 3D cell cultures .....	6
2.2.3 Microfluidic development, fabrication and 3D printing.....	6
2.3 Theory.....	8
2.4 Experimental.....	9
2.4.1 Materials.....	9
2.4.2 Equipment .....	9
2.4.3 Chip Fabrication.....	10
2.4.4 Gelatin microgel preparation .....	11
2.4.5 Heating and cooling systems .....	11
2.5 Results .....	12
2.5.1 Commercial chip.....	12
2.5.2 PDMS-glass chip quality and channel roughness .....	14
2.5.3 Chip design evolution .....	15
2.5.4 Device heating and cooling systems.....	16
2.5.5 Flow rate Optimisations .....	18
2.5.6 Cell viability and microgel morphology .....	21

2.6 Discussion.....	21
2.6.1 Issues with commercial devices.....	21
2.6.2 Comparison of 3D printed mould chip surface roughness and resolution vs commercialised device.....	22
2.6.3 Chip design evolution.....	23
2.6.4 Comparing heating and cooling systems .....	23
2.6.5 Flow rate optimisations .....	24
2.6.6 Coalescence of droplets.....	25
2.6.7 Surfactant free generation of gelatin microgels with encapsulated HepG2 cells outlooks and possibilities.....	25
2.6.8 Batch production of droplets.....	26
2.7 Conclusions .....	26
Chapter 3 – Rapidly prototyped 3D printed flow cell the screening of extracellular lectins via glycomimetic liposomes.....	29
3.1 Abstract.....	29
3.2 Introduction .....	29
3.2.1 Targeted drug delivery to biofilms.....	29
3.2.2 Microfluidic assay.....	30
3.3 Theory .....	30
3.4 Experimental .....	31
3.4.1 Materials .....	31
3.4.2 Equipment.....	31
3.4.3 Chip Fabrication .....	31
3.5 Results.....	32
3.5.1 Chip configuration optimisations.....	32
3.5.2 Lectin targeting liposome targeting on fabricated flow cells. ....	33
3.6 Discussion.....	35
3.7 Conclusions .....	36
Chapter 4 – Three-dimensional bioinspired intertwining channel multiplexed droplet generator. ....	37
4.1 Abstract.....	37
4.2 Introduction .....	37
4.3 Theory .....	38
4.4 Experimental .....	40
4.4.1 Materials .....	40

4.4.2 Equipment .....	40
4.4.3 Device design.....	40
4.4.4 Device Fabrication .....	42
4.5 Results .....	42
4.5.1 Planar 3D printed device .....	42
4.5.2 3D printed 64 outlet device with intertwining channels.....	45
4.5.3 Singular outlet device with 3D channels .....	48
4.6 Discussion .....	49
4.7 Conclusions.....	51
Chapter 5 – Development of an ultra-high voltage electrophoresis system using a Van de Graaff generator capable of $10^7$ theoretical plates.....	53
5.1 Abstract .....	53
5.2 Introduction.....	53
5.3 Theory.....	54
5.4 Experimental.....	56
5.4.1 Chemicals and materials.....	56
5.4.2 Electronics .....	57
5.4.3 Capillary .....	57
5.4.4 Detection .....	58
5.4.5 3D Printer, materials and settings .....	58
5.5 Results .....	58
5.5.1 Implementation of 3D printed parts and dry air system.....	58
5.5.2 Capillary lifetime verification.....	59
5.5.3 Separations.....	60
5.5.4 Characterisation of the electric field and migration times.....	62
5.5.5 Injection optimisation and separation improvement .....	63
5.5.6 Capillary degradation .....	65
5.6 Discussion .....	66
5.7 Conclusion .....	68
Chapter 6 – Conclusions and Outlook .....	71
6.1 Chapter 2 – 3D printed moulds for the production of microgel liver cell encapsulation devices.....	71
6.2 Chapter 3 – Rapidly prototyped 3D printed flow cell the screening of extracellular lectins via glycomimetic liposomes. ....	71

6.3 Chapter 4 – Three-dimensional bioinspired intertwining channel multiplex generator. ....	71
6.4 Chapter 5 – Development of an ultra-high voltage electrophoresis system using a Van de Graaff generator capable of $10^7$ theoretical plates. ....	72
6.5 Summary .....	72
6.6 Outlook.....	73
Appendices.....	75
Chapter 2 Support Information.....	75
Chapter 3 Support Information.....	79
Chapter 4 Support Information.....	80
Chapter 5 Support material .....	91
5.1 Experimental setup .....	91
5.2 Additional experimental data .....	94
Bibliography .....	97
Acknowledgements.....	107

## Chapter 1 – Introduction

Microfluidics is the study of manipulating liquids on the micro-, nano- and pico-litre scale. Photolithographic technology pioneered the development of integrated circuits in the 1950's by J. Kilby and R. Noyce.<sup>1,2</sup> This technology was adopted to fabricate micro-structured silicon for microfluidic devices, leading to the development of the first “lab-on-chip” device by S. Terry in 1979. Here, a gas chromatograph was etched into a silicon wafer.<sup>3</sup> Since then microfluidics has flourished and become an essential technology within molecular biology (e.g. bioassays and flow cells) and molecular analysis (e.g. electrophoresis) as well as other fields such as micro-propulsion, thermal technologies, and micro-bioreactors.<sup>4-8</sup> Many of these technologies still use the same principles of design as the original two-dimensional (2D) integrated circuit boards. This sets limitations on design, such as overlapping channels, leading to the more recent seeking of device optimisations over truly novel innovation. However, this thesis seeks to describe different methods to approach microfluidics which, whilst still following microfluidic principles, uses innovative approaches to solve current limitations. Recent developments in additive manufacturing technologies could provide new fabrication techniques to allow for the advancement of the field. High resolution microfluidics is resource intensive; faces expensive start-up costs and can be difficult to access. Yet, additive manufacturing simply requires someone who can generate computer aided drawings (CAD) and a three-dimensional (3D) printer with a comparable resolution, which is far more rapid and cheaper. 3D structures have always been difficult to manufacture using the powerful planar technologies of photolithography or micro-milling. But this is regarded as effortless and natural for 3D printing. The easier a new dimension is to access for the design, the more possibilities of advantageous devices will be inevitably generated by the scientific community. Alternatively, what could be considered an outdated technology, a Van de Graaff generator, could be applied in combination with 3D printed elements to perform record breaking electrophoretic separations in terms of theoretical plates. 3D printing is a growing field and may hold the key for the natural evolution of microfluidics.

### 1.1 Description of the current fabrication techniques

As previously stated, microfluidic fabrication is based upon the same principles as integrated circuits. Typically, an open microfluidics device is produced by bonding a structured surface to either an unstructured or another structured surface. Here is a brief introduction of microfluidic fabrication techniques, however a more detailed description is provided in “Microfluidics and Lab-on-a-chip” by J. S. O'Connor, A. Manz, P. Neuzil and G. Simone, in particular chapters 2 and 4.<sup>9</sup>

Photolithography is used to generate structures onto a surface, typically glass or silicon. Masked photolithography uses masks, often photo-resistive layers, to block an excitation light which either chemically alters the surface of the substrate or excites an etching chemical which then generates the structure. Mask-less photolithography uses more refined optics to pattern surfaces without a masking photoresist layer. Laser based techniques, such as electron beam lithography, focused ion beam, laser interference, zone-plate/light-emitting-diode array; are available and boast higher resolution and flexibility than their masked counterparts. Micro-milling has also seen use for the fabrication of devices, whereby the structures are generated from the direct removal of material from the substrate.

Soft lithographic fabrication methods focus on using polymers as the key material of the device. Replica moulding combines a liquid polymer, typically curable via a cross-linker or ultraviolet (UV) light, with a prefabricated mould. The resultant stabilised polymer is then peeled off the mould and bonded to another flat substrate. Hot embossing and injection moulding use a similar process but replaces the curing polymer for a molten polymer. Micro-milling and direct laser cutting are also applicable to soft materials.

## 1.2 Advantages and disadvantages of current microfluidic processes

General advantages of microfluidics compared to bulk processes include greater control of micro volume liquids; more detailed analysis within the device; devices can be produced from a wide variety of materials; higher throughput; continuous processing; regimentation and standardising conditions where random factors could be more prevalent, e.g., cell cultures. As previously mentioned, many of the fabrication techniques and design structure are adopted from integrated circuit board technology, even the same computer aided drawing software and library can be used. This rapidly speeds up the development time of a device. Commercialised devices are easily accessible and common place in many modern laboratories, with cartridges and well plates being common examples.<sup>10-12</sup> Such strengths are why microfluidics is currently a 17.9 billion dollar (USD) market with a projected compound annual growth rate of 16.3% from 2021 to 2028.<sup>13</sup>

However, there are naturally some disadvantageous elements to microfluidics. With an increase in resolution comes an increase in the start-up costs. Clean rooms are employed to eliminate any dust or dirt from disrupting the production, resulting in even greater costs, and reducing availability. Rapid prototyping is limited and costly. Whilst the design software employed is incredibly powerful for their tasks, many are limited to 2D design and fabrication, yet we live in a 3D world. Limiting designs to 2D structures aids in simplifying the predictability of a model but limits the representative power of a model trying to replicate a system that is 3D in nature.

## 1.3 The promise of 3D printing

3D printing has been a growing field for the past 20 years with increasingly accessible technologies coming to market. With that comes development in the printer's resolution, particularly those on the micrometre scale, making it a technology fostering immense potential for microfluidic device fabrication. Additionally, support components of an experiment could be 3D printed as the user required. With the correct knowledge, skills and way of thinking, a scientist only requires access to some CAD software and a 3D printer to access the world of microfluidics, regardless of laboratory equipment, conditions, or training.

## 1.4 Research Question

With this line of thinking, this thesis seeks to answer the question:

### **HOW COULD ALTERNATIVE TECHNOLOGIES BE IMPLEMENTED TO OVERCOME CURRENT LIMITATIONS IN MICROFLUIDICS?**

To provide some answers to this question, the thesis is divided into four chapters which investigate how 3D printing and other technologies could be implemented to solve the issues at hand.

## 1.5 Thesis structure

### Chapter 2 – 3D printed moulds for the production of microgel liver cell encapsulation devices.

Chip development and fabrication can be expensive. This makes iterative prototyping frameworks unsuitable for microfluidic systems. Chapter 2 investigates the development of a novel microdroplet generating device for the encapsulation of liver cells within gelatin. The devices were fabricated using a 3D printed mould, allowing for a constant production of iterative designs and new device testing with comparable performance to commercial devices at a fraction of the price.

Whilst electronic heating is a simple process on the microfluidic scale, cooling is a far more difficult process requiring more power and additional elements to transfer the heat to. Heat control is essential when fabricating microgels. A water heating and cooling system was integrated into the device and compared to an electronic heating and cooling system. Here, the water-based system performed as well as the Peltier system whilst allowing observations through the glass substrate, unlike the Peltier based counterpart, and with a smaller heat diffuse area.

### Chapter 3 – Rapidly prototyped 3D printed flow cell for the screening of extracellular lectins via glycomimetic liposomes.

*(Publication title: Targeting extracellular lectins of Pseudomonas aeruginosa with glycomimetic liposomes)*

Chapter 3 also demonstrates the applicability of 3D printed moulds for polydimethylsiloxane(PDMS)-glass devices but optimised for producing a flow cell device. In addition to this, the issue of selective surface coating was also overcome. It is difficult to only coat one specific wall of the channel, and excess coating and non-selective surface coating results in background noise. Flow cell to flow cell variation of hydrogel coating density is also an issue causing signal variation. Here, a pre-coated glass slide was bonded to structured PDMS resulting in multiple flow cells with one evenly coated hydrogel surface. Surfaces could be regenerated after use allowing multiple uses from the same device.

### Chapter 4 – Three-dimensional bioinspired intertwining channel multiplexed droplet generator.

*(Patent title: Monodisperse micro droplet producing device and method of producing the same as.)*

Design and fabrication of current 3D microfluidic structures is restricted. Manufacturing is time intensive and costly with current 2D based technologies. The majority of designs are still folded, intersecting, or stacked 2D structures, creating artificial 3D features. Chapter 4 presents a conceptual droplet generator device which houses 64 parallel droplet generators, which are inspired by natural 3D geometrical sequences of splitting and recombining structures, e.g., veins, arteries, and trees. The device features intertwining structures, which are integral to the function of the device, unlike prior supposedly 3D structures. A simplified singular droplet focus flow intersection device, both planar and 3D, is fabricated and evaluated to allow for extrapolated operation conditions of the 64 generators to be estimated.

### Chapter 5 – Development of an ultra-high voltage electrophoresis system using a Van de Graaff generator capable of $10^7$ theoretical plates.

Electric field strength, hence, the applied voltage, is proportional to the performance of electrophoresis separations. Higher resolution capillary electrophoresis demands higher applied voltages, but this incurs joule heating, which is severely detrimental to performance. Previous

experimentation with a Van de Graaff generator showed promise, as the generator is a low current generator with a resultant high voltage but suffered from capillary degradation and failure due to dielectric breakdown. Chapter 5 discusses the implementation of insulating 3D printed plastic parts, a wooden cabinet and dry air system allowed for longer capillary lifespans. These improvements allowed for more experimental conditions to be optimised and the observation of record high resolution separations.

## Chapter 2 – 3D printed moulds for the production of microgel liver cell encapsulation devices.

### 2.1 Abstract

In this chapter, a rapid prototyping of 3D printed moulds for a microfluidic droplet generator is described; which would be implemented for the production of surfactant free HepG2 cell-encapsulated microgels, thus providing 3D biomimetic environments for high-throughput cytotoxicity screenings within the device; at oil flow rates of 75  $\mu\text{L}/\text{min}$  and water flow rates equal to 8  $\mu\text{L}/\text{min}$ ,  $\phi = 0.107$ , at a rate of 26 droplets per second. Gelatin droplets were produced with similar conditions. Integrated heating and cooling water channels controlled the viscosity and gelation of gelatin within the device, with the device's heated region maintained at 37 °C and the cooled region maintained at 15 °C. Genipin crosslinking of the microdroplets was performed outside of the chip. Encapsulated HepG2 cells were found to have a viability of 96% post production. The same system was applied to provide cell-laden microgels for other projects, and the fabrication method was applied in Chapter 3. Successful prototyping and application implementing 3D printed moulds results in a versatile device ready for production at a fraction of the time and cost compared to traditional methods.

### 2.2 Introduction

#### 2.2.1 Bioassays

Bioassays are defined as a procedure to determine the relation between a physiological agent and the effect which it produces in a living organism.<sup>14</sup> Stimuli and responses may be physical, chemical, biological, physiological or psychological and must be compared to a control population.<sup>15</sup> The main goal of utilising assays is to simplify a real world biological system, allowing researchers to determine the cause and effect of stimuli on the biological system, either by direct<sup>16</sup> or indirect assays.<sup>17</sup> Innumerable amounts of bioassays and their applications are available<sup>5,18,19</sup> but simple ones that are commonly used are enzyme-linked immunosorbent assays, such as pregnancy tests<sup>20</sup> and HIV screenings.<sup>21</sup> A more recent test that is widely discussed among the public are rapid lateral flow assays for the detection of COVID-19.<sup>22</sup>

This desire to simplify complicated biological systems led to the development of direct 2D *in-vitro* systems, whereby a cell culture is grown as a monolayer in a petri dish or culture flask attached to a plastic surface.<sup>23</sup> A simple example would be the direct treatment of cancer cells in a 2D well plate with different anticancer drugs and comparing the viability over time.<sup>24</sup> Such assays provide valuable information and are often simple to use and multiplex, allowing for the theorising and initial development of automated systems.<sup>25</sup> This chapter shall mainly focus on millifluidic and microfluidic bioassays, particularly comparing 2D and 3D cellular microgel assays.

Often, cellular bioassays implement 2D systems as a cheap, rapid, and low maintenance way of avoiding testing on whole living organisms. However, 2D cultured cells do not mimic natural structures and intracellular interactions in tissues. Such factors are essential for measuring cell viability, proliferation, differentiation, morphology, response to external stimuli and drug metabolism leading to non-representative gene and protein expression.<sup>26–29</sup> 3D cell cultures do mimic natural structures and as such do not have the previous drawbacks,<sup>30–33</sup> but this is at the

cost of being more time consuming, costly, decreased reproducibility and less commercially available.<sup>34–37</sup>

### **2.2.2 3D cell cultures**

The promise of 3D cell cultures has still garnered attention despite these disadvantages with research developing to minimise the drawbacks. Implementation of biomimetic microgels has been developing over the years for several purposes using materials such as collagen, fibrin, agarose, alginate, and many others.<sup>38–42</sup> These applications seek to provide a more in-vivo like response from the encapsulated samples whilst also decreasing time and costs. Most implement microgels or microbeads to instil a greater degree of uniformity amongst the prepared sample. Hydrogels allow for the diffusion of nutrients and stimuli through the network to the cells, whilst extracellular signals; such as extracellular vesicles; may diffuse out of the droplets and be analysed.<sup>43</sup> Controlling the bead size means that all the cells within the microgels should experience similar diffusion times, therefore the time to receive a stimulus and respond should be constant across the population. Additionally, extracellular fibres, such as filopodia and actin, are more prevalent in 3D hydrogel systems containing gelatin demonstrating more behaviours that are more representative of in-vivo conditions.<sup>44,45</sup>

Gelatin is a naturally occurring protein polymer, a derivative of collagen, and has an extensive history as biomedical material in assays and drug delivery due to its biodegradability and biocompatibility in physiological environments.<sup>46–48</sup> Since then, gelatin has become another versatile tool for microencapsulation methodologies.<sup>49–54</sup> Gelatin is described to have poor mechanical properties, as gel relies upon hydrogen bonding between polymer chains to maintain its form (gelation), and undergoes a sol-gel transition between 31 to 40 °C, depending greatly on the concentration and Bloom number/average molecular mass.<sup>55–57</sup> Crosslinking is essential to create microgels that are physically more stable and rigid. Crosslinking is achieved using UV light activated crosslinkers, oxidative chemical crosslinkers or enzymes.<sup>58–60</sup> Genipin is a naturally derived crosslinker that is commonly used. Crosslinking can be controlled by controlling the genipin concentration and crosslinking time. As the degree of crosslinking increases, the Young's modulus increases resulting in a more rigid gel, furthermore, the microgels swell less in physiological solutions and have enhanced thermal stabilities.<sup>61</sup> Customisation of the microgel stiffness can promote cell viability and proliferation and outperform 2D cell cultures.<sup>62</sup>

*Chapter 2.2.3 – Microfluidic development, fabrication and 3D printing*

### **2.2.3 Microfluidic development, fabrication and 3D printing**

Microfluidic devices; typically fabricated using glass, silicon or polymers, feature sub-millimetre structures to allow for the manipulation of small volumes of liquids in highly precise and controlled way.<sup>9</sup> Microfluidics has been implemented many times for the generation of droplets and microgels with the intent of encapsulating living cells since the early 2000's<sup>63</sup>, which go on to be used as bioassays, either within the device or outside.<sup>64–66</sup> Microfluidics are naturally advantageous over bulk emulsion methods as the produced microgels are smaller; reduced variation; reduced waste; more controllable in size; reduced shear stress on encapsulated cells; contain multiple fabrication steps in one device and allow for a higher and continuous throughput of generated devices.<sup>67,68</sup> All of these favour a microfluidic total analysis system to be fabricated where droplet generation, crosslinking, microgel cleaning and bioassay assessment to be performed in one device.<sup>69–75</sup> Commercial devices are available with predetermined flow rates, allowing for intuitive and user-friendly operation from companies, such as Micronit, ChipShop and

Dolomite, being widely and readily available. However, custom devices must be designed for when experiments diverge and explore new encapsulation materials, especially when working with hydrogels.

Prototyping of high-resolution microfluidics often relies upon developing a design based on simulations, compartmentalising the separate functions of the device into separate designs, followed by the photolithographic fabrication of either a silicon or glass device for functional testing.<sup>76-78</sup> As this is a costly process; several designs are fabricated from one wafer. Each of these designs then requires complete fabrication. All of which takes time and incurs cost. Systematic errors are common in prototyping, such as a minor design flaw not apparent in simulations or optical requirements; thermal properties; mechanical properties; chemical incompatibilities of the devices with the required function are also commonplace. Cheaper prototyping methodologies with reduced resolution also exist, such as; PDMS soft lithography, micro-milling, hot embossing, or rapid etching techniques (laser or reactive-ion etching (RIE) or dry RIE) are implemented.<sup>79-81</sup> However, these can still be resource or labour intensive and require many steps just to produce one prototype device. Once all the components have been individually tested, several prototypes are then produced to combine the components and end in with a functional complete device.

One growing field in microfluidic fabrication and prototyping is the implementation of additive manufacturing techniques. 3D printed moulds for microfluidics were first implemented by the Whitesides group in 2002, using inkjet printing to produce a soft lithographic mould.<sup>82</sup> Several examples of moulds produced via different 3D printing techniques have been fabricated and shown to have comparative performance to typical devices,<sup>83-87</sup> but at the cost of a reduced resolution and surface quality. PDMS devices using 3D printed moulds have also been fabricated, with droplet generating devices capable of generating droplet sizes as little as 80  $\mu\text{m}$ .<sup>88</sup> Alternatively, a method that produced 350  $\mu\text{m}$  and 100  $\mu\text{m}$  wide interconnecting channel scaffolds to produce droplets sized  $310 \pm 24$  and  $120 \pm 9$   $\mu\text{m}$ , respectively.

There is also compatibility issues depending on the printer and methodology employed.<sup>89</sup> However, these are outweighed by the massively reduced cost, prototype fabrication speed and cycle, ease of accessibility of the technology, ease of use for untrained users and reduced material. Iterative design cycles are much easier to employ with faster fabrication techniques. Prototyping does not seek to fabricate the perfect device but allow us to learn more about the design by action. Therefore, the more cycles and changes one can make in a smaller time, the quicker one learns about the nature of the device and the criteria required in fabricating a perfect device.

With this in mind, the following will describe the development of a PDMS-glass gelatin microgel generating device without the need for surfactants. 3D printing is implemented to enable rapid prototyping to produce a device with comparative performance to a commercial glass device. Cells encapsulated within dispersed gelatin microgels will present high viabilities, with the intent of further experimentation as bioassays. Integrated heating and cooling channels will control viscosity within the device. Controlling the temperature allows for gelatin sol-gel transitions to allow for a) liquid gelatin droplets to be produced and b) droplets to undergo gelation and form stable microgels.

### 2.3 Theory

Droplet generation depends on fluid instabilities. In open capillary microfluidic systems, two immiscible phases are flowed into the same channel. Whichever phase is flowed at a higher rate act as a continuous phase whilst the other phase is the discontinuous/dispersed phase. There are many of configurations to generate droplets<sup>90</sup>, but for the purpose of simplicity, this chapter shall only consider 2D focus flow configurations. Dimensionless numbers are used to describe and predict different flow forces and stresses. The capillary number ( $Ca$ ) is independent of the device length, whilst the Reynolds ( $Re$ ), Bond ( $Bo$ ) and Weber ( $We$ ) numbers are very small in microfluidics (Eq. 2.1-4).

$$\text{Capillary number} = Ca = \frac{\eta u}{\gamma} \quad (\text{Eq. 2.1})$$

$$\text{Reynolds number} = Re = \frac{\rho u L}{\eta} \quad (\text{Eq. 2.2})$$

$$\text{Bond number} = Bo = \frac{\Delta \rho g L^2}{\gamma} \quad (\text{Eq. 2.3})$$

$$\text{Weber number} = We = \frac{\rho u^2 L}{\gamma} \quad (\text{Eq. 2.4})$$

Microscale characteristic lengths results in viscous forces being dominant over inertial forces, where  $\eta$  is the viscosity,  $u$  is the bulk flow velocity,  $\gamma$  is the surface tension between the continuous and discontinuous phase,  $\rho$  is the density,  $L$  is the channel length and  $g$  is gravitational force.  $L$  is so such a small value that that, in droplet generation, only the  $Ca$  is significant as it is a function of the viscosity ratio between phases ( $\lambda$ ) and the flow rate ratio of the two phases ( $\phi$ ) and not  $L$ . The values of  $Ca$ ,  $\lambda$  and  $\phi$  can used to determine the droplet generation regime, which is categorised as squeezing, dripping, jetting, tip streaming and tip multi-breaking. Tip-streaming provides the smallest possible droplets and is characterised by using relatively high flow rates, hence high  $Ca$ . A tip-streaming regime is observed when both the continuous and discontinuous  $Re \ll 1$ ,  $Ca_c > Ca_{cri}$  and  $\phi \ll 1$ , where  $Ca_c$  is the  $Ca$  of the continuous phase and  $Ca_{cri}$  is an equal to  $F_n/F_v F_\eta / F_\gamma$  (viscous and surface tensions forces respectively). Understanding these factors and the regime is essential when it comes to designing droplet generating systems that implement hydrogels, as the higher viscosity immediately leads to more problematic droplet generation and stabilisation.

Stability and production rates can be improved by implementing surfactants to decrease the surface tension of the discontinuous phase. Such a reduction leads to an increase in droplet frequency, as the shear force required to generate a droplet is reduced, as well as stabilising generated droplets leading into a reduction of droplet size dispersity.<sup>91,92</sup> However, this comes at the cost of requiring more post-production cleaning steps as well as toxicity effects upon the encapsulated biological material.<sup>93–95</sup> Passive surfactant-free droplet generation methods has been previously demonstrated<sup>96</sup>; however, it is more common to include the application of external forces to droplet generators, e.g. coacervation<sup>97</sup> and centrifugal<sup>98</sup>, to overcome the viscous forces.

An alternative method to reduce the surface tension is to selectively heat the device at the site of droplet generation. Thermally controlled devices have been implemented for the purpose of droplet generators before but found that an apparent trend of exponentially larger droplets as temperature increases.<sup>99</sup> This was only observed when the device was heated by 20 K higher than the ambient temperature. Further developments were made using liquids with immensely different viscosities, where the droplet diameter as a function of temperature,  $D(T)$  in m, is inversely proportional to the  $Ca$  of the continuous phase (Eq. 2.5).<sup>100</sup>

$$D(T) \propto Ca^{-1} = \left(\frac{\eta_c(T)u_c}{\gamma_c(T)}\right)^{-1} = \frac{\gamma_c(T)}{\eta_c(T)u_c} \quad (\text{Eq. 2.5})$$

where,  $\eta_c(T)$  is the viscosity of the continuous phase in  $\text{kg m}^{-1} \text{s}^{-1}$ ;  $u_c$  is the velocity of the continuous phase in  $\text{m s}^{-1}$ ; and  $\gamma_c(T)$  is the surface tension of the continuous phase in  $\text{N m}^{-1}$ . This relation directly reinforces the prior understanding of how the  $Ca$ ,  $\lambda$  and  $\phi$  are integral to understanding droplet generation. These confirmed that the surface tension had a near linear relationship to the change in temperature whilst the viscosity had a steep dependence, as typically seen in sol-gel transitions.<sup>101</sup> Therefore, systems that can control both temperature and flow rates possess a far greater number of variations than systems where only the flow rate can be controlled. Alternatively, cooling a droplet would increase the viscosity and surface tension, stabilising the droplet against coalescence in accordance to the literature.<sup>102</sup> Since then, several devices have been developed that implement either heating or cooling zones into the droplet generation.<sup>66,103–105</sup>

## 2.4 Experimental

### 2.4.1 Materials

Chip moulds were produced using polylactic acid (PLA) filament, 1.75 mm diameter, Raise3D, USA; Iron-filled metal composite PLA, 1.75 mm, Proto-Pasta, USA. Devices were fabricated using polydimethylsiloxane, as Slygard 184, and black Slygard 170 (Dow Chemical Co., Michigan, USA). Both purchased from Sigma-Aldrich. UHU plus endfest 90 min (UHU GmbH & Co. KG, Germany) was purchased from a commercial supplier. All silicone tubing (ID x OD, 1/16 x 1/8 inch) was purchased from Sigma-Aldrich (produced by Saint-Gobain, USA). Droplet generation experiments used deionised water with a commercial food dye to aid visualisation. Silicone oil, 350 cSt (25 °C), was used as the continuous phase, purchased from Sigma-Aldrich, USA. Gelatin droplet generation used the following: Gelatin type A (porcine skin, ~300 g Bloom); HepG2 cell line; ATCC formulated Eagle's minimum essential medium; 10% foetal bovine serum; 10000 U/mL Penicillin; 10000  $\mu\text{g}/\text{mL}$  streptomycin; genipin ( $\geq 98\%$ ), phosphate buffered saline (PBS) and Pluronic® L-64 (Mn~2,900); which were all purchased from Sigma-Aldrich.

*Chapter 2 – 3D printed moulds for the production of microgel liver cell encapsulation devices.*

### 2.4.2 Equipment

A commercial device and side-connect holder, 15 mm x 15 mm, was purchased from Micronit, Netherlands. The device was the DGFF.SC.75, a side inlet droplet generating device with 75  $\mu\text{L}$  channels with hydrophobic fluorinated polymer coatings. Polyether ether ketone (PEEK) tubing (1/16" OD, 0.5 mm ID) and ferrules were also purchased from Micronit, Netherlands. 3D printed elements were drawn using the computer aided design software Autodesk Fusion 360, Autodesk, USA. These were exported as .STL files and sliced into GCode using ideaMaker, Raise3D, USA. The GCode was then printed using a fused filament 3D printer, a Raise3D E2, Raise3D, USA. All moulds

were fabricated using a 0.2 mm nozzle. The print speed was 10 mm/s, layer height was equal to 0.1 mm, print temperature of 200 °C and a bed temperature equal to 60 °C. A PICO low pressure plasma system (Diener Electronic GmbH & Co. KG, Germany) was used for the plasma treatment of PDMS and glass. Two separate Aladdin syringe pumps, AL-2000, World precision instruments, USA were used for the injection of oil and water into the Micronit and fabricated devices. Water heating and cooling control systems used separate peristaltic pumps, Masterflex® Ismatec® REGLO 78018-10, Avantor®, USA. Two Peltier elements (TEC1-12706) were purchased from a commercial supplier and used in the Peltier based system. Microscope images were captured using a Stemi 508, Zeiss, Germany coupled with a digital single-lens reflex (DSLR) camera, EOS 80D, Canon, Japan, for single image collection and a mobile phone camera, 10E, Samsung, South Korea, for 960 frames per second video capture. SEM images were observed using a Quanta 250 FEG, FEI Company, Holland, at an accelerating voltage of 7.00 kV, 1200x magnification and 166 Pa using an LFD.

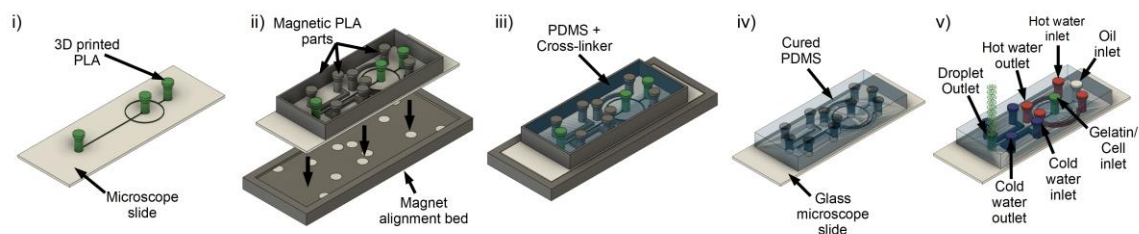


Figure 1.1: Schematic of PDMS-glass device fabrication. i) 3D printing (filament) directly onto a microscope slide forming the mould; ii) Magnetic mould parts alignment on magnet bed, iii) PDMS casting of the mould, iv) Cured PDMS is plasma treated and bonded to a microscope slide; v) Droplet generation. Droplets are collected externally and then centrifuged to extract the droplets into a water phase. Cross-linking using genipin (1% w/v) for 10 minutes and cleaned. Schematic shown in Support Figure: 1.1 to 1.7.

### 2.4.3 Chip Fabrication

Moulds were fabricated by the direct 3D printing of PLA onto cleaned microscope slides. The print height of the first layer was adjusted by the height of the microscope used, approximately 100 µm plus 10 µm for nozzle clearance. The total print time for the droplet channel mould was 14 minutes. Total print time for an entire mould (droplet channel, heating and cooling channels and outer support) would be 2 hours and 50 minutes. An outer ring was printed at first to hold the microscope in place. A pause sequence was put into the GCode to pause the print at 1 mm. The slide would then be manually loaded into the support ring and the print resumed. Once the heating, cooling and outer frame components were optimised, these were printed using thicker more durable magnetic PLA parts. Magnetic parts are placed on top of the 3D printed mould and aligned on custom 3D printed alignment bed with imbedded magnets. The PLA outer ring was sealed in place using hot glue to avoid leakage. PDMS was prepared in a 10:1 ratio (polymer:crosslinker) by weight, degassed, and poured into the mould. The PDMS was left to cure overnight at 40 °C. The PDMS was peeled off the mould and cleaned with deionised water and isopropanol. Once dry, the PDMS and a cleaned glass microscope slide was plasma treated with pure oxygen at 350 W for 1 minute and immediately brought into contact with one another. The PDMS-glass device was then placed under a 2 kg mass and baked at 40 °C for 2 hours. Epoxy was used as a sealant around the PDMS-glass edge to improve device durability. The droplet channel

was cleaned with deionised water and isopropanol. A sodium hydroxide solution was flushed through the droplet generation channel and dried with compressed air. The channel was filled with undiluted Sigmacote® and allowed to dry. The siliconized chip was then washed with isopropanol and water and allowed to dry. Silicone tubing was inserted into the devices inlets and outlets and sealed in place by black PDMS. This process is depicted in Figure 1.1.

#### 2.4.4 Gelatin microgel preparation

Gelatin/cell samples were prepared by mixing a 15% (w/v) gelatin type A (porcine skin, ~300 g Bloom; Sigma-Aldrich, USA). A suspension of HepG2 cells ( $1 \times 10^6$  cells/mL) in a medium of ATCC formulated Eagle's minimum essential medium, 10% foetal bovine serum, 10000 U/mL Penicillin, 10000 µg/mL streptomycin. The two prepared solutions were mixed in a 1:1 ratio and gently mixed at 37 °C for 20 mins, 400 rpm in a thermomixer. The gelatin/cell mixture was then pumped through the droplet generator device with the continuous silicone oil phase, 350 cSt (25 °C). The generated microdroplets were then washed out of the oil phase via centrifugation (8000 rounds per minute (rpm), 1 min, 4 °C) and the oil phase is removed by decanting. 1 mL of the cleaning solution with Pluronic® L-64 is added to the solution, shaken on a vortex mixer, and then centrifuged again (8000 rpm, 1 min, 4 °C). This cleaning step is repeated twice. 1 mL of 0.5% genipin in PBS solution is added to the microdroplets and left to crosslink for 15 minutes. Samples are shaken gently once every minute to ensure better distribution of the genipin solution. After crosslinking, the genipin solution is removed by centrifugation (8000 rpm, 1 min, 20 °C) and the subsequent decantation. A cleaning wash with pure PBS was performed. A Live/Dead™ cell double staining kit was purchased from Sigma-Aldrich, USA, for viability assessment of cells.

#### 2.4.5 Heating and cooling systems

A hot water reserve was prepared by placing a water reservoir upon a hot plate set to 60 °C. A cold water reservoir was prepared by preparing an ice:salt bath (1:1). Both the heating and cooling channels had their respective temperature water pumped through the device at 0.45 mL/min using a peristaltic pump. Additionally, a water heated syringe holster was 3D printed and included to the hot water flow cycle, as shown in Figure 1.2.

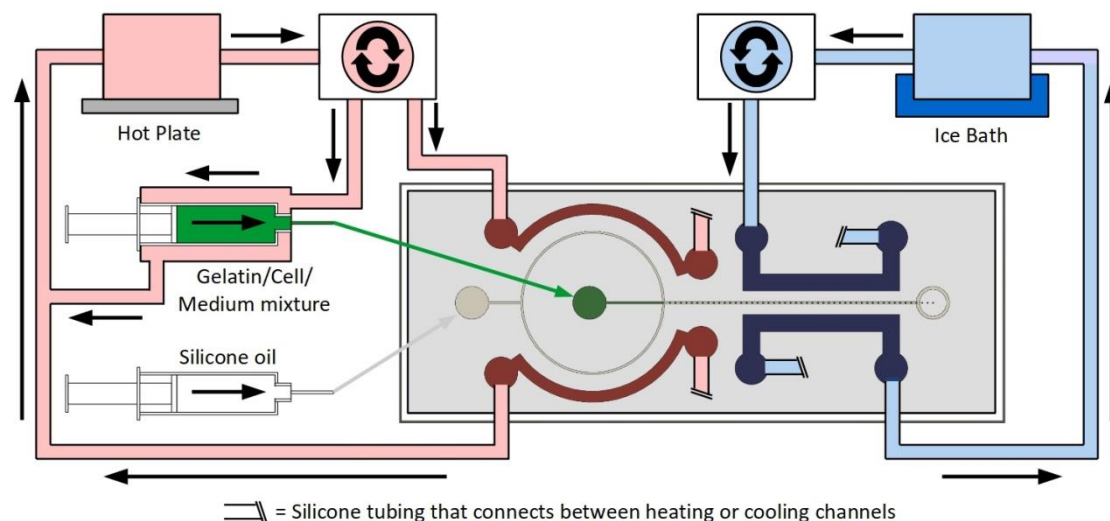


Figure 1.2: Water heating and cooling system schematic. Microscope slide sized device with integrated heating and cooling channels. Water heated syringe jacket is also included. Not to scale.

A Peltier heating and cooling system was constructed to compare the water-based system too, as per Figure 1.3. The heating Peltier was controlled to 40.5 °C whilst the cooling politer was measured 4 °C, as per the provided data sheets. Between 0.7 - 1.5 Watts was applied to achieve this.

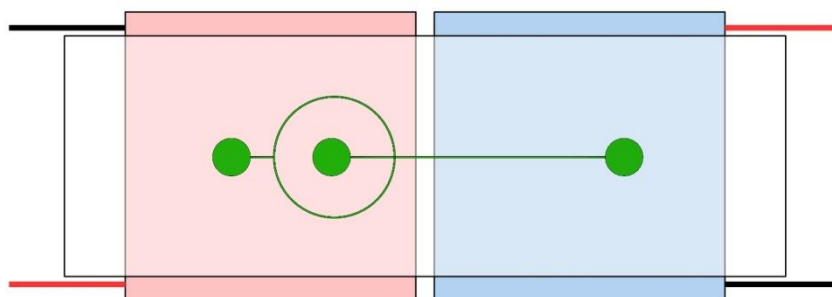


Figure 1.3: Schematic for the Peltier heating and cooling system. The microscope sized device is resting on top of the heating and cooling elements. Not to scale.

## 2.5 Results

### 2.5.1 Commercial chip

The purchased droplet generator from Micronit was operated as per the provided instructions. A variety of flow rates was implemented. Figure 1.4 shows the device under operation with an oil flow rate ( $Q_{oil}$ ) and a water flow rate ( $Q_{water}$ ) of 10  $\mu\text{L}/\text{min}$ . Droplets were observed to be generated in a jetting formation. Droplet generation was measured once the droplets had stably separated from the stream, where the outlet channel was widest. This is considered as the 0 mm mark, i). The second line, ii), is 2.5 mm from the point of droplet generation, where the instable droplets collide with one another and coalesce. At 0 mm, the mean droplet diameter is  $78 \pm 9 \mu\text{m}$ ,  $n = 100$ , at a rate of  $215 \pm 1$  droplets per second, Figure 1.5, whilst droplets 2.5 mm after production have a mean droplet diameter equal to  $150 \pm 44 \mu\text{m}$ ,  $n = 100$ , Figure 1.6.

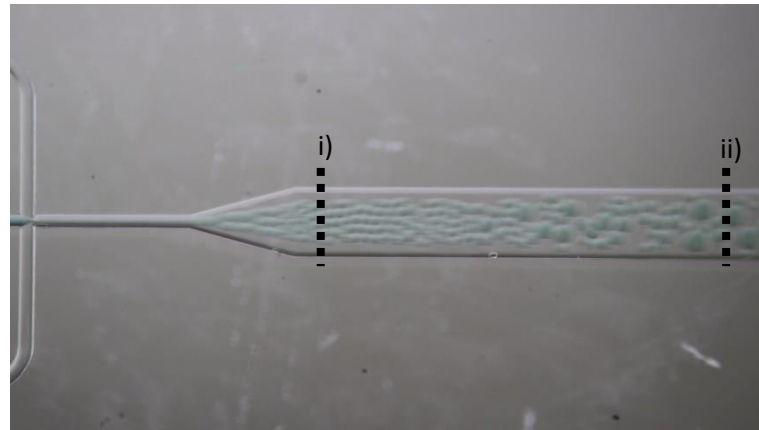


Figure 1.4: Micronit side inlet chip generating water oil droplets.  $Q_{oil}$  and  $Q_{water}$  of 10  $\mu\text{L}/\text{min}$ . i) Origin point of droplet generation, considered 0 mm. ii) 2.5 mm from droplet generation. Link to video - <https://youtu.be/-qUTahGCEAQ>.

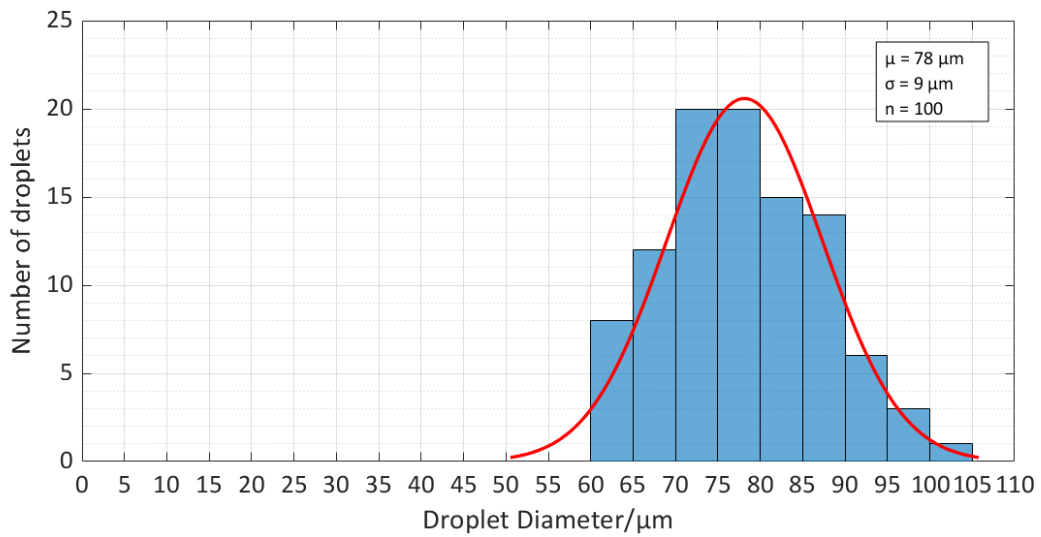


Figure 1.5: Distribution of droplets generated at origin point of droplet generation (Figure 1.4 line i)).  $\mu = 78 \mu\text{m}$ ,  $\sigma = 9 \mu\text{m}$  and  $n = 100$ .

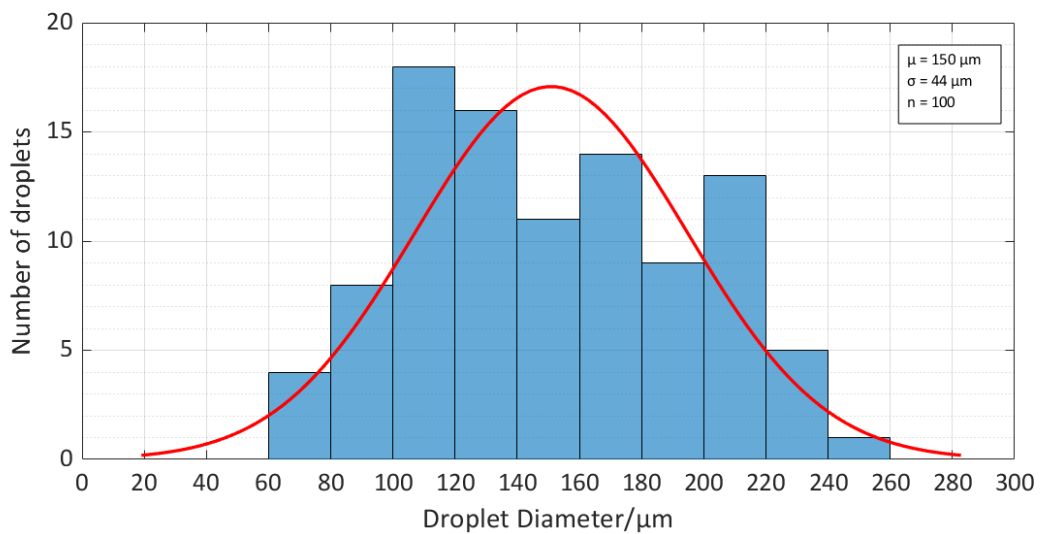


Figure 1.6: Distribution of droplets generated at 2.5mm (Figure 1.4 line ii)).  $\mu = 150 \mu\text{m}$ ,  $\sigma = 44 \mu\text{m}$  and  $n = 100$ .

As with any glass microfluidic device that features channels smaller than 100  $\mu\text{m}$ , blockages and partial clogging by fibres, Figure 1.7, or unfiltered and non-homogenous liquids are prevalent and can hinder device operation and optimisation. Such blockages require more intensive cleaning methods to remove the blockages, such as acid washes or burning out material in a furnace. Such processes remove the hydrophobic coating applied to the channels and require the devices to undergo surface treatment after each wash. Gelatin is solid at room temperature and would block the commercial device, even in concentrations as low as 5%. External heating elements would be required to the channels are also too small to allow for high pressures to overcome the high viscosity of such low concentrations.

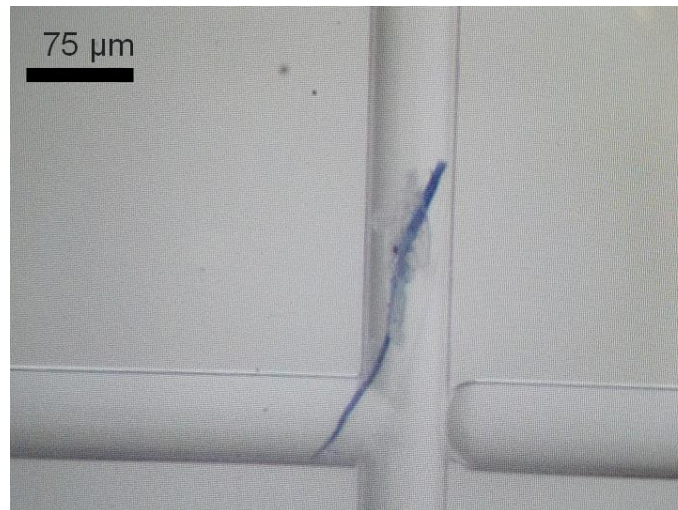


Figure 1.7: Paper fibre within the channel. In this location, it interrupts the droplet generating intersection and would require acid treatment or furnace treatment to remove.

### 2.5.2 PDMS-glass chip quality and channel roughness

Glass-PDMS devices were produced as described, as seen in Figure 1.8. PLA was printed directly onto glass so that the bonding surface of the casted PDMS had a glass smooth surface. The layered structure of the PLA moulds was present in the channel walls, as shown in Figure 1.9. The PDMS channel measured a height of  $190 \pm 3 \mu\text{m}$  and a width equal to  $162 \pm 22 \mu\text{m}$ . Channel roughness did vary depending on the face of the channel. The bottom of the channels was glass, hence considered smooth.

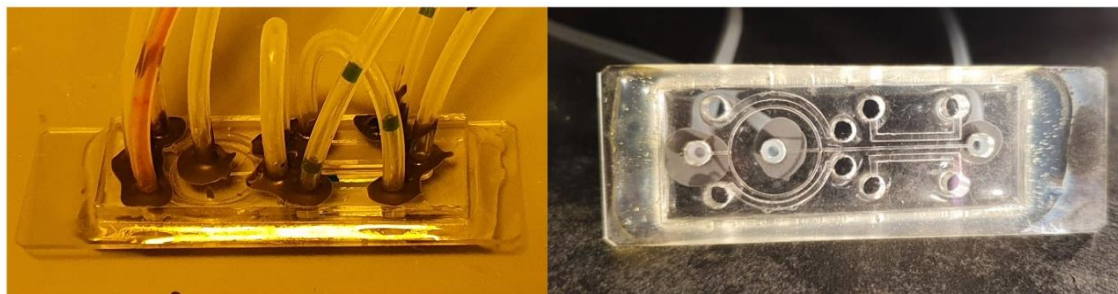


Figure 1.8: Completed device with integrated heating and cooling channels. Left) “Top” of the device. Here the inlet and outlet tubing can be observed, along with the heating and cooling feed tubing, as well as the interconnecting tubing. Right) “Bottom” of an incomplete device. Droplet generating experiments were observed through the glass “bottom” as the 1 mm glass provides better working distances.

The top of the channel showed minor variation, as this is the top of the extruded plastic, and experienced an “ironing” effect which smooths the surface, as shown in Figure 1.10. However, this smoothness is only observed in channels which are as wide as the nozzle, specifically the droplet generation channel. Additionally, locations where intersecting print paths would also result in a rougher top surface as the heated nozzle would drag upon the surface. Areas where the PLA would be retracted, and the nozzle would lift off the print would also show a distinct roughness. Model slicing and tool pathing was manipulated to ensure no lift off occurred during the printing of the droplet generation channel. The largest variation was that in the channel width. Here the effect of depositing one PLA layer on top of the other causes the curved structure leading to the “pinching” of width in the centre of the channel mould.

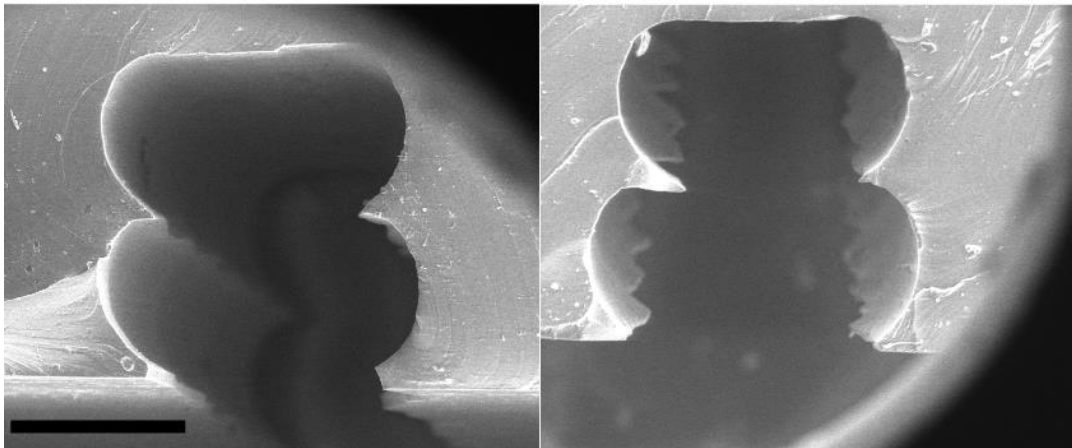


Figure 1.9: SEM images of the droplet generation channel - Side. Side surfaces are curved showing the layered material squeezing between the nozzle and the glass slider. The top of the channel is relatively flat. Tearing of this central structure is seen throughout, caused by trapped PDMS remaining on the channels during lift off. PDMS channel height =  $190 \pm 3 \mu\text{m}$  and width =  $162 \pm 22 \mu\text{m}$ . Scale bar =  $100 \mu\text{m}$ .

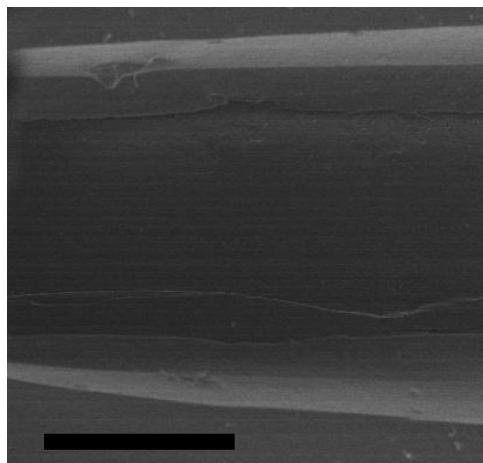


Figure 1.10: SEM images of the droplet generation channel - Top. Side surfaces variation is apparent. The ironing effect is apparent on the top of the channel, resulting in a relatively smooth surface. Scale bar =  $100 \mu\text{m}$ .

### 2.5.3 Chip design evolution

Five key droplet generation designs were implemented during the development of the 3D printed moulded devices. The initial design, Figure 1.11, was to mimic typical cross designs. Here, the intersection was rough, due to the tool pathing, and the variation in the channels and connecting

inlet tubing resulted in inconsistent droplet generation. This led to development of design b) where the circular inlet channels allowed for the even splitting of the oil inlet, therefore an even flow pressure at both sides of the device. The intersection was tapered to try and promote encapsulation, but this was removed to reduce roughness. The sudden widening of the outlet is typical of microfluidic droplet generators, as the sudden increase in width reduces the internal velocity, enhancing localised instabilities in the discontinuous phase. This was found to also promote droplet collisions and coalescence, so this was removed for design c). Here stable droplets were generated as the continuous channel dimensions keep constant velocity, so no collisions occur. Cooling channels introduced, design d), to induce the physical gelation of the gelatin droplets. Cooling is transferred by the glass, resulting in gelation to occur at the intersection and blocking the devices. Heating channels were then introduced to compensate for the cooling effect, both ambient and on the device, allowing for gelatin be kept above its melting point within the device. 97 different iterations of these designs have been implemented with varying dimensions and configurations over the period of 3 months of development.

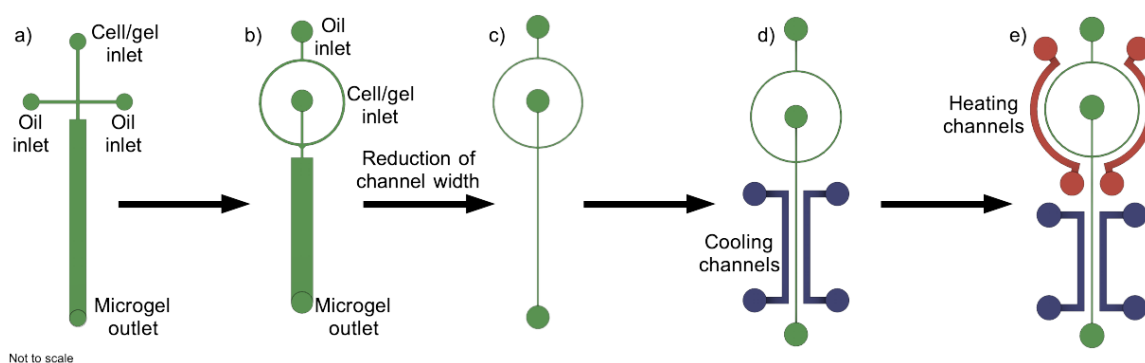
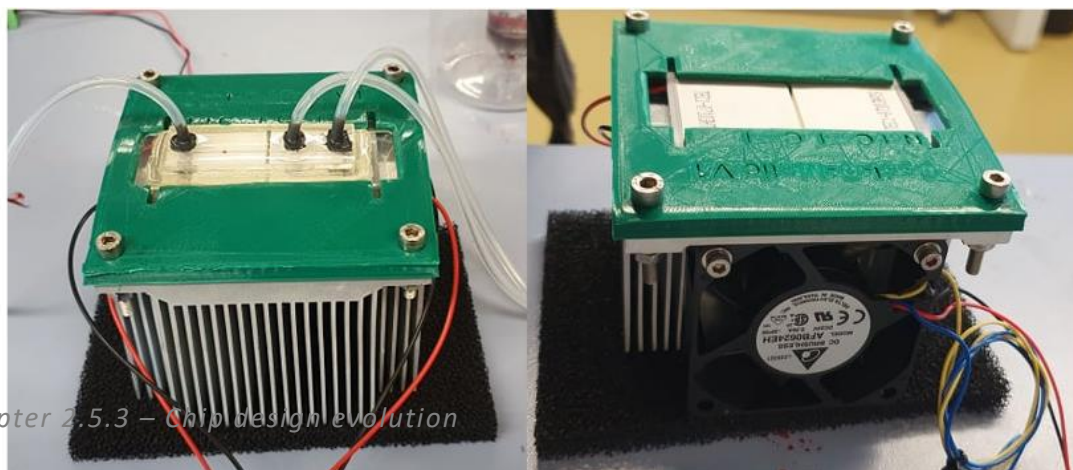


Figure 1.11: 5 Key iterations of droplet generating device. a) Basic cross design; b) Circular oil inlet channels; c) Constant channel dimensions; d) Inclusion of cooling channels and e) Inclusions of heating channels.

#### 2.5.4 Device heating and cooling systems



Chapter 2.5.3 – Chip design evolution

Figure 1.12: Peltier heating and cooling system. The system consists of the two Peltier elements mounted on top of a metal block. The elements are pinned in place by the 3D printed frame, ensuring contact to the metal block. Droplet observations were taken from the top of the device, through the PDMS. Left) Front of the setup. Here the droplet generating device is loaded into the top of the frame and rests upon the heating and cooling

elements. Right) Back of the Peltier system. The metal block has a cooling fan to disperse the transferred heat from the cooling element.

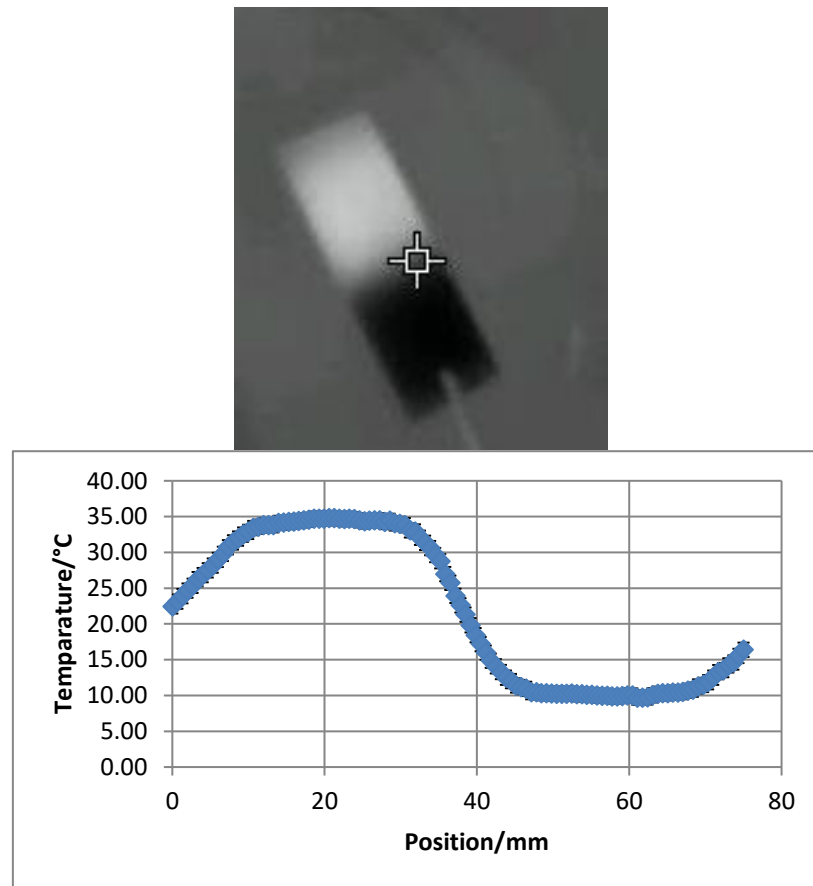


Figure 1.13: Peltier heating and cooling system performance. Left: FLIR image of glass slide briefly removed from Peltier heating and cooling system. Heated areas are white and cooled areas are black. Right: Temperature as a function of the position on the slide, from the top edge to the bottom edge. The effective heated region is approximately 20 mm long and 34 °C. A transition length of approximately 16 mm is observed. The effective cooling region is 20 mm long with a temperature of 10 °C.

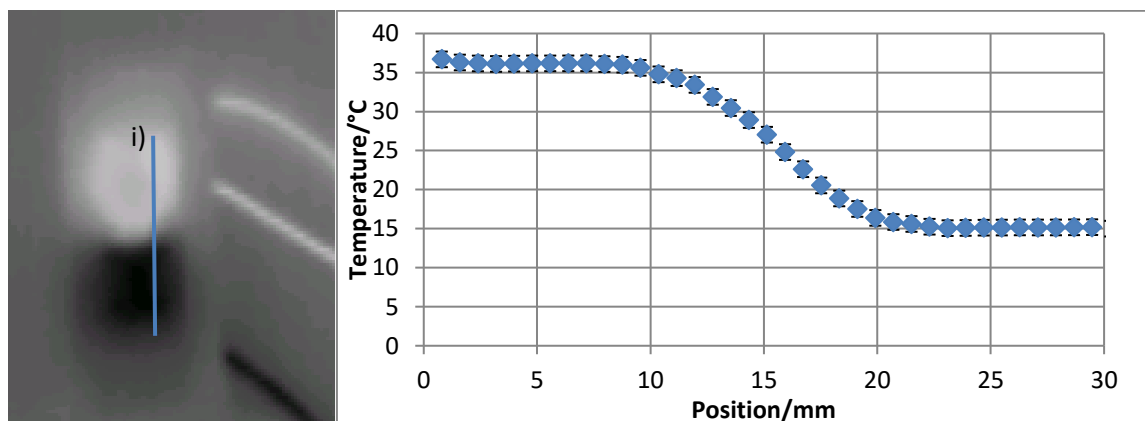


Figure 1.14: Water heating and cooling system performance. Left: FLIR image of the operational device with integrated water heating and cooling system. Heated areas are white and cooled areas are black. Right: Temperature as a function of the position on the slide, along line i). The effective heated region is approximately 10 mm long and 37 °C. A

transition length of approximately 10 mm is observed. The effective cooling region is 20 mm long with a temperature of 15 °C.

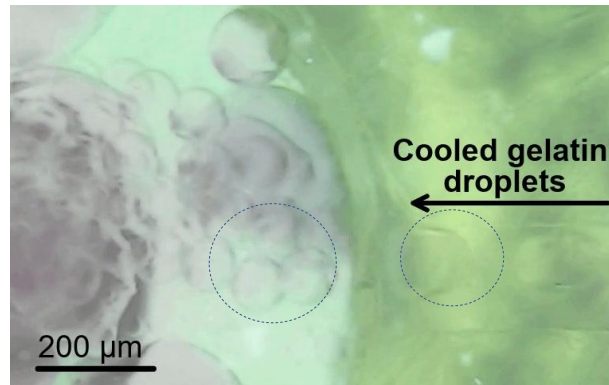


Figure 1.15: Cooled droplets approaching the outlet (right circle), colliding with other droplets (left circle), and not coalescing. Droplets then move to the centre of the outlet and pass out of the chip. Waste material can be seen as the large amorphous shapes. The QR code and following link direct to a video showing the elastic collisions - <https://youtu.be/7jxi1ZhMHq4>.

Both Peltier and water heating and cooling systems were trailed. The Peltier system, shown in Figure 1.12, achieved an effective heated region that is approximately 20 mm long and 34 °C. A transition length of approximately 16 mm is observed. The effective cooling region is 20 mm long with a temperature of 10 °C, Figure 1.13. Meanwhile, the water system achieved an effective heated region of approximately 10 mm in length and 37 °C. A transition length of approximately 10 mm is observed. The effective cooling region is 20 mm long with a temperature of 15 °C, Figure 1.14. Droplets were cooled enough so that elastic collisions were observed at the outlet, as shown in Figure 1.15.

### 2.5.5 Flow rate optimisations

Optimisations of the flow rates were performed and reported in Figure 1.16 and 1.17. Optimisations were performed using water in oil generation. The optimal condition was considered to be where the smallest and most frequent droplets occurred with least variance. The optimum flow rate ratio was determined to be 0.107. Gelatin/water experiments would require minor adjustments to this ratio, but under ideal conditions, the gelatin would be water like in viscosity, hence the same ratio required. Surfactant free gelatin/cell medium in oil droplets were produced, which were  $91 \pm 5 \mu\text{m}$  in diameter within the device; at flow rates of  $Q_{\text{Oil}}$  equal to 75  $\mu\text{L}/\text{min}$  and  $Q_{\text{Water}}$  equal to 8  $\mu\text{L}/\text{min}$ ,  $\phi = 0.107$ , at a rate of 26 droplets per second, Figure 1.18.

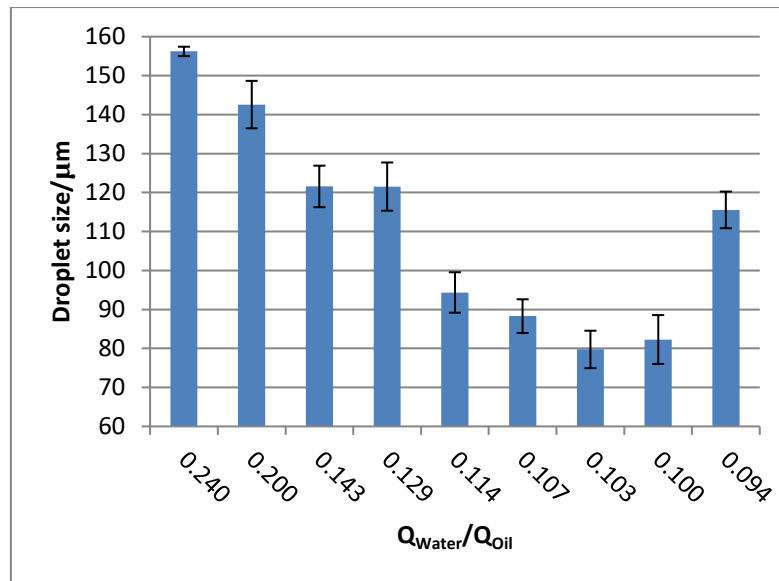


Figure 1.16: Droplet size as a function of the ratio of the water and oil flow rates. Flow rate ratio 0.1 represents  $Q_{\text{Water}} = 8 \mu\text{L}/\text{min}$  and  $Q_{\text{Oil}} = 80 \mu\text{L}/\text{min}$ .

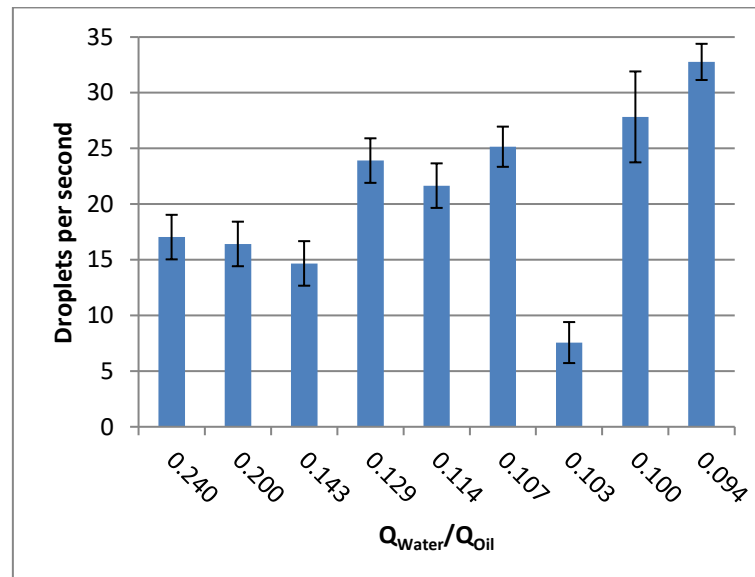


Figure 1.17: Rate of droplets produced as a function of the ratio of the water and oil flow rates. Flow rate ratio 0.1 represents  $Q_{\text{Water}} = 8 \mu\text{L}/\text{min}$  and  $Q_{\text{Oil}} = 80 \mu\text{L}/\text{min}$ .



### 2.5.6 Cell viability and microgel morphology

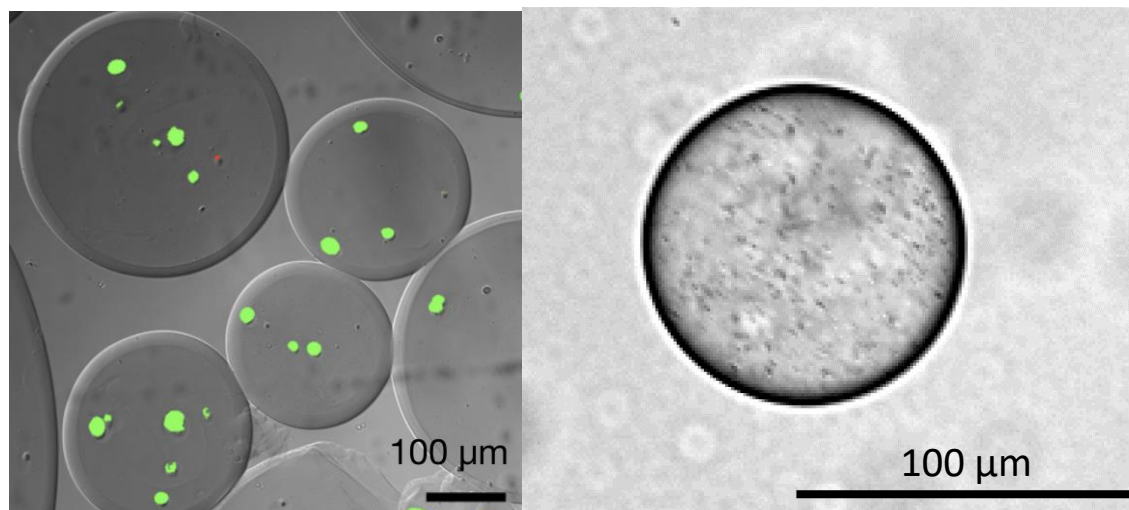


Figure 1.19: Left) Crosslinked gelatin microgel with encapsulated HepG2 cells. Viability rate is based upon cell counting from DIC and fluorescence microscopy with Live/Dead™ staining; calcein-AM (green) and propidium iodide (red). Cell viability 2 hours after microgel generation was found to be 96%. Additional examples are shown in Support Figure 1.10. Right) Example of others using the droplet generating devices. Gelatin microdroplet laden with probiotic bacteria (black dots) prior to crosslinking (Produced by Nina Apushinkina).

Cells that underwent encapsulation and gelatin crosslinking survived the process with a rate of 98% viability after generation, an example of the Live/Dead staining™ assessment shown in Figure 1.19 Left. Unstained inclusions are assumed to be air bubbles or dust trapped in the droplet. Diameter variation prior to and post crosslinking is assumed to be caused by coalescence outside of the chip, due to the crosslinking procedure introducing surfactants and centrifugal forces, assumed by comparing the post- and pre-crosslinked microgels in Figure 1.19 left and right respectively. Also, the droplets are elastically squeezed between the microscope slide and cover slip, thus the larger diameter and “contact ring” observed on every microgel.

## 2.6 Discussion

### 2.6.1 Issues with commercial devices

As expected, the commercial device delivered on its promise of ease of use and being able to replicate similar droplet rates and sizes of given flow rates. However, there is a competition between the stabilising effects of a surfactant against the toxicity of the surfactant. The previous work had stated that the used concentration of Pluronic® L-64 was 100 ppm, as in the Micronit experiment. The LD50 for rats is 5000 ppm. Often, the toxicological concentration to observe the LD50 for rats is far above the lethal dose for individualised cells, however here the experiment was only a factor 50 below so it was assumed that many of the resultant encapsulated cells would be dead but has not been fully assessed. Additionally, stabilisation was not observed indicating the surfactant concentration was too low in the system, as shown by the droplet coalescence between 0 mm and 2.5 mm (Figure 1.5 and 1.6). Initial experiments with the PDMS-glass device also used the same concentration of L64 but observed no stabilisation and an increase in droplet size variation, Support Figure 1.8 and 1.9.

Even if the water in oil droplets were stabilised; the second persistent issue would then become apparent immediately. The lack of temperature control meant that gelatin/cell/medium mixtures would block with solidified gelatin at the intersection and gelatin/cell mixture inlet as gelatin undergoes gelation at room temperature. This would result in varying injection flow rates, as the gelation would increase the viscosity and alter the viscosity ratio, until the device would eventually be blocked by solidified gelatin. To control the flow rate, modification to the chip or external micro-heating and -cooling elements would be required. This would significantly increase development and fabrication costs of the device, especially for the customised chip configurations with integrated temperature control systems from commercial service providers. Cheaper external heating and cooling elements could be attached to the device however these would then cause optical issues, such as background noise, refractive or reflective, and reduce image quality. These chips are also small, so the heating and cooling elements would also have to be miniaturised too. Miniaturised Peltier cooling systems struggle with a reduction in size, as these rely upon the opportunity to transfer heat to an external mass, hence smaller elements reduce the area for this exchange to occur.

Both issues bring forth the major issue that gelatin systems often require customised systems of incredibly specialised design. Device fabrication per device can be costly, which are then easily multiplied if an iterative design approach was taken. Modelling is often implemented to reduce erroneous designs; however, the addition of manipulating gelatin makes it far more difficult and time consuming to do so. Each time a device was blocked, Figure 1.7, it would require harsh treatment (furnace/acid) and reapplication of the surface treatment. This would be time consuming and costly, especially coupled with the heating and cooling issue.

### **2.6.2 Comparison of 3D printed mould chip surface roughness and resolution vs commercialised device**

Whilst the 3D printed mould allowed for the production of droplets on the micrometre scale, it is only appropriate to compare the channel quality and droplet quality against the commercial device. As previously stated, channel size determines droplet generation for squeezing and dripping systems regimes, often resulting in droplets that are only slightly smaller than the channel diameter. But we do not observe this in the 3D moulded devices. We observe a narrow tip jetting regime due to the relatively high flow rates and low flow rate ratio. Here the droplet size is a function of the protruding cone geometry, an extremely low Reynolds number, the continuous fluid viscous stress being greater than the capillary pressure of the injection nozzle and thin jet region to have a velocity equal to the continuous flow's velocity. All these conditions cause the centre of the jet to be able to protrude into the injection nozzle area, experience shear forces from the continuous phase flow that in turn pinches the droplet behind the protrusion and in turn generate a droplet smaller than the channel diameter. The pinning location of the dispersed phase does matter as this defines the widest area of the cone. Therefore, whilst the rough channel walls would be a hindrance in dripping, squeezing, and jetting regimes, it is not so apparent in the tip jetting regime, where the tip is localised into the centre of the channel and independent of the surface quality. Such a regime is only as possible in focus flow devices.

All these conditions being met allowed for the PDMS-glass devices, with channels that are approximately  $162 \pm 22 \mu\text{m}$  in width and  $190 \pm 3 \mu\text{m}$  in height, to produce low variance droplets that were  $91 \pm 5 \mu\text{m}$ , Figure 1.18. The commercial droplet generating device operated in a jetting

regime at high flow rates but with similar flow rates. The well-defined channel width of 75  $\mu\text{m}$  resulted in droplets that were  $78\pm 9$   $\mu\text{m}$  in diameter, agreeing with the supporting material and previous literature on jetting stream droplet generation variation and diameter in comparison to the channel size. It is possible to compare the droplets generated in the commercial device,  $78\pm 9$   $\mu\text{m}$ , and the 3D printed mould,  $91\pm 5$   $\mu\text{m}$ . In terms of size, there is an overlap in the droplets generated however the differences lie in the droplet production rate and stability. The commercial device generates more droplets by a factor 7 to 10 however these droplets are far less stable. By 2.5 mm, the droplets are coalescing, and variation is far higher than in the 3D printed mould device. For the purposes of our intended users, the slower but more stable droplet generation was favoured. Additionally, droplets generated in the 3D moulded device are competitive with other 3D printed droplet generating devices described in the literature.

### 2.6.3 Chip design evolution

3D printing offers a far more rapid production of many distinct designs in a short span of time for a fraction of the cost, at the compromise of a reduced resolution. As shown by Figure 1.11, several iterative designs can be fabricated. Each design functioned to solve one specific issue with the structure. Beginning with the simple cross it was possible to observe the bias that can occur when there is variation between the two separate oil inlets, either by different tubing length, surface variation or intersection quality. So, the second design, b), eliminated this bias by introducing the single oil inlet and circular structure to split and recombine the oil with no apparent bias. Yet, the variation in channel width caused the decrease in velocity. Whilst in the literature, this promotes jetting instability and droplet generation; in this device it promoted droplet collision. With or without surfactant stabilisation, droplet collisions still resulted in droplet coalescence and so larger than intended droplets were produced. Hence, design c); which maintained a constant droplet generation channel, allowed for the production of droplets which would not collide until the outlet. Therefore, the time to travel to the outlet became the possible area for cooling and gelation of the microdroplets. Once sufficiently cooled, the microdroplets could collide with one another and not coalesce. This allowed for the initial flow rate optimisations to occur, Figure 1.16 and 1.17.

### 2.6.4 Comparing heating and cooling systems

Two separate heating and cooling systems were prepared, an integrated water system and an external Peltier system. The Peltier system was dependant on the glass being in contact with the Peltier elements. Water heating and cooling achieved a maximum temperature of 37  $^{\circ}\text{C}$  and minimum of 15  $^{\circ}\text{C}$  with a transition length of approximately 10 mm, Figure 1.14. Peltier heating and cooling achieved a maximum temperature of 34  $^{\circ}\text{C}$  and minimum of 10  $^{\circ}\text{C}$  with a transition length of approximately 20 mm, Figure 1.13.

Peltier elements are well defined and seen many different applications in microfluidics for temperature control. As shown in the FLIR, the heating and cooling are very defined blocks, and the temperature is maintained well throughout operation. However, there are some drawbacks of this system. The chip must be in constant contact with the Peltier. However, the cooling element would often form condensation. If this formed a thin layer between the glass and the Peltier, then the cooling efficiency would significantly decrease with it. To compensate for this, dry air would have had to be blown over the system. Additionally, the glass-PDMS device had to be heated or cooled through the glass. Therefore, the droplet generation within the device had to

be observed through the PDMS, which was 6.44 mm thick to allow for the tubing insertion. Whilst PDMS is transparent, a thicker layer means a greater working distance which in turn limits the magnification. Peltier cooling systems rely upon the transfer of the thermal energy from one side to the other. Hence, the thermal energy of the device is drawn into a metal block that is then cooled using fans. The block does have a thermal capacity that would be reachable during operation. At this point, the cooling effect would cease until the block cooled, another limiting factor of operation. As previously mentioned, the Peltier elements provide well defined regions of heating and cooling; however, the proximity of the elements causes the 20 mm thermal transition region, despite the 1 mm space between the two elements. More power would be required to reduce this region of competition but then one must consider the chip channel structure and if this region needs to be so small. In an ideal system, the region would be smaller to allow for more freedom in the channel structure.

Water based heating and cooling systems are uncommon in microfluidics but more common in general mechanical or electrical engineering designs. Considering the implementation of 3D printing for the mould fabrication, it only then seemed natural to include the heating and cooling mechanism into the design. Water temperature systems require millifluidic channels which would imply additional masks and alignment in typical microfluidic systems, and additional fabrications time and costs. Meanwhile, 3D printing allowed for a greater freedom of design without additional fabrication time and costs, just more printer time. One advantage over the Peltier system is the integration of the heating and cooling channels into the PDMS layer, allowing for observations through the 1 mm glass layer. This provides a flat smooth surface with a smaller working distance and so higher resolution images are possible. With regards to the performance of the two systems, both are capable of heating and cooling the devices enough to manipulate the gelation within, however the water systems allow for more specified heating/cooling regions that allow for a reduction of the temperature diffusion region. Generated droplets are cooled sooner and hence cooled for longer in the water-based system, allowing for a greater degree of gelation and reduced chance of coalescence occurring.

In accordance with Eq. 2.5, a higher temperature results in larger droplets at a constant flow rate ratio ( $\phi$ ), as the change in viscosity is greater than surface tension. However, the operational temperature must be both high enough to allow the gelatin to undergo the gel-sol transition whilst not too high so that the encapsulated cells are damaged. Fortunately, the 7.5% gelatin/cell mixture is heated to 37 °C with the water system. This is above the melting point of the gel and well within the HepG2 cells viable temperature range. Whilst higher temperatures would lower the viscosity allowing for higher flow rates, this would be detrimental to both the cell viability and increase the size of the droplets produced, as per Eq. 2.5.

### **2.6.5 Flow rate optimisations**

In accordance with the literature, a tip streaming regime is observed in Figure 1.18. There is an optimum  $\phi$  which lies where the smallest and most frequent droplet generation occurs.  $\phi$  must be decrease so that  $Ca_c$  exceeds the  $Ca_{cri}$  to establish the tip streaming regime. Decreasing  $\phi$  results in smaller droplets until a critical point, where the flow of the oil is too great, resulting in the water phase to become trapped and for larger droplets to be generated in a pulse where the water channel pressure was greater than the oil pressure. This is shown by the gradual decrease in droplet size as the flow ratio decreased, Figure 1.16, as well as the increase in droplet

generation rate, Figure 1.17, until the ratio equals 0.107. As shown by Figure 1.18, droplets were  $91 \pm 5 \mu\text{m}$  in diameter within the device and produced at a rate of 26 droplets per second. After 0.107, the flows become more inconstant and show smaller droplets at a reduced droplet generation rate or larger droplets at larger droplet generation rates. Therefore, the flow rate ratio of 0.107 was considered the optimum as it provided one of the smallest and fastest droplet generations with the lowest variation. Variations to this selected flow rate ratio would become apparent when using the higher viscosity gelatin/cell/water mixture. Cooling and heating systems could then begin to be considered for the droplet generation device. Cooling channels and heating could then be included in the 3D printed mould, whilst an external Peltier system was fabricated to compare the two.

### 2.6.6 Coalescence of droplets

By comparing the droplets generated, Figure 1.18, against the post- and pre-crosslinked microgels, Figure 1.19a and 1.19 b respectively, it is assumed that coalescence does occur once the droplets leave the device and undergoes crosslinking. This could be in the interim of the droplets leaving the device into the chilled receptacle or during the crosslinking stage which requires many centrifuge washes. Application of the centripetal forces could easily force the droplets to merge. Also, a lack of temperature control during the crosslinking stage results in the droplets to warm up, hence decrease in their degree of gelation providing a lowered barrier for coalescences. Such a lack of control undermines the purpose of creating such small droplets and should be eliminated in future iterations of this experiment. The purpose of using microfluidics to generate droplets is to create uniform microenvironments for the encapsulated sample, thus controlling many factors that could have more variation in 2D systems e.g., diffusion length. The more variation in microgel size, the greater the variation in biological responses one would observe. A single cell in a  $90 \mu\text{m}$  microdroplet will not respond to stimuli in the same way that multiple cells would in a  $400 \mu\text{m}$  microdroplet. If the gelation microgel is loaded with fine nanoparticles or bacteria for drug or smart food delivery, different sized microgels will release at different rates, have different material loads and different residence time in the body. Such variance is not acceptable in many fields. Additionally, contact lines between the microgels and cover slide can be observed in Figure 1.19 (left). Such deformations mean that the optical assessment of the microgels becomes more difficult as well as demonstrating inconsistencies between the droplets.

### 2.6.7 Surfactant free generation of gelatin microgels with encapsulated HepG2 cells outlooks and possibilities

Gelatin microgels with encapsulated HepG2 cells were produced with a viability of 98%. This demonstrates that the process does not significantly damage or kill the cells and further experiments can then be performed. This work acted as an opportunity to develop a tool to be used in collaboration with others to generate microgels with encapsulated biological samples. As previously discussed, cells in biomimetic environments display more in-vivo like responses. One initial study by Nina Apushinkina for her Master project was the application of encapsulating probiotic bacteria for smart food delivery.<sup>106</sup> Simply put most of probiotic bacteria in commercial food stuffs, e.g., Yakult & Activia, never reach the lower gut, as the strong stomach acids and enzymes digest whatever passes through. Her work found that encapsulated bacteria have a significantly improved viability in acid conditions for up to 2 hours, compared to non-encapsulated samples. Proposed protective mechanisms are the buffering effect observed within the hydrogel, sacrificial destruction of the gel shell as the acid approaches the bacteria and finally the droplets

generated in this experiment were purposefully large, approximately 300  $\mu\text{m}$ , and so the diffusion pathway was increased hence the longer survival times. This requires further investigation as the supporting literature is rife with conflicting protective mechanisms. Such research is of interest for industry, as reducing the genetically modified bacterial load per serving means a cheaper product. Another investigation performed with Eunheui Gwag investigated the toxicity exposure of HepG2 to silver nanoparticles and silver ions.<sup>107</sup> Silver nanoparticles in the environment may undergo a breakdown and release silver ions. Therefore, a way to distinguish between the effects of the two is required. Eunheui found that encapsulation of the HepG2 cells eliminated the toxicity observed from nanoparticles, whilst the effect of silver ions was still observed. This model would provide a way to assess the cytotoxic effect of ion release from nanoparticles, which is impossible to do normally to do with 2D cell cultures.

### **2.6.8 Batch production of droplets**

One major concern for these 3D printed moulded devices is batch processing. Each 3D print has minor variations, resulting in minor adjustments having to be made from chip to chip. This is far from ideal, as commercial devices are provided with reliable flow rate vs droplet size or production rate data. Additionally, the devices produce droplets at a significantly slower rate than the glass-glass counterparts. This is due to the smaller channels experiencing a higher velocity for the same flow rate. However, the purpose of 3D printing was not for the mass production of droplets or devices. 3D printing was utilised for rapid prototyping of a design that functioned for the user's needs. Once the design was finalised, it would be advantageous to utilise traditional methods, such as a SU-8 mould produced via lithography, to create a master mould that would allow for the reproducible reproduction of an identical structure. The mould would also be far more stable than the PLA on glass, which would often detach during the peel off step. A SU-8 mould would not be able to recreate the tapered features of the 3D printed mould without some form of post-production milling, assembly, or multiple masks during photolithography. The droplet generators are also currently limited to one focus flow intersection per microscope slide. Commercial devices that have several integrated and connected droplet generators are entering the market and becoming more common place. Whilst the resolution of the filament printer used would allow for multiple droplet generating nozzles to be printed on one microscope slide, the crowding issues arise due to the requirement of the integrated heating and cooling channels. These require relatively wide channels and large surface areas to maximise the heating or cooling effects. Multiplexing the droplet generation, either by parallelisation or serialisation would be fruitless if there is no temperature control for the gelatin droplet formation. Additionally, often the formulation of the gelatin droplets would be altered by changing the encapsulated biological sample and different sized droplets are required. These experiments did not require industrial quantities of microgels, just small batches. Some strengths of the microfluidic device are the simplicity and its flexibility in how the device can be used, especially if one intends to produce many different microgels with many different compositions.

## **2.7 Conclusions**

To conclude, 3D printed moulds were used to produce microfluidic droplet generating devices with integrated heating and cooling channels. Devices were developed using rapid prototyping frameworks, unlike traditional microfluidic development. This allowed for 5 key designs, with 97 different iterations, to be implemented over a 10-week period. The final fabricated devices had

channels that were  $190 \pm 3 \mu\text{m}$  in height and  $162 \pm 22 \mu\text{m}$  in width, the large variance in the width due to the stacking of two extruded layers of plastic. Viscosity was controlled within the device using integrated water heating and cooling channels. The device's heated region was maintained at  $37 \text{ }^\circ\text{C}$  and the cooled region maintained  $15 \text{ }^\circ\text{C}$ . There was an approximately 10 mm diffusion region between the two. The heating allowed for the gelatin to be liquid during droplet generation and the cooling resulted in the physical gelation of the droplets allowing droplet collision without coalescence, hence a surfactant free process. A temperature system controlled with Peltier heating and cooling elements was prototyped but found to be less favourable than the water system. Surfactant free gelatin/cell medium in oil droplets were produced, which were  $91 \pm 5 \mu\text{m}$  in diameter within the device; at flow rates of  $Q_{\text{oil}}$  equal to  $75 \mu\text{L}/\text{min}$  and  $Q_{\text{water}}$  equal to  $8 \mu\text{L}/\text{min}$ ,  $\phi = 0.107$ , at a rate of 26 droplets per second. Droplet size generated was comparative to a commercial device but greatly reduced production rates. HepG2 cell laden gelatin droplets of the same size were produced. Crosslinked with genipin was performed outside of the device. Coalescence was observed once the droplets left the device. HepG2 cell viability was found to be 96% post encapsulation and microgel crosslinking. The device was then implemented for the fabrication of cell laden microgels for nanoparticle toxicity screening, smart food delivery, encapsulation of pH sensitive bacteria for a bioluminescence sensor and a model for fatty liver disease of encapsulated HepG2 cells. The method of prototyping was also applied to the production of a flow cell device, as described in Chapter 3.



## Chapter 3 – Rapidly prototyped 3D printed flow cell the screening of extracellular lectins via glycomimetic liposomes.

*(Publication title: Targeting extracellular lectins of Pseudomonas aeruginosa with glycomimetic liposomes)*

### 3.1 Abstract

Novel solutions are required for the approaching antimicrobial resistance crisis, and particularly true for biofilm forming Gram-negative pathogens. Biofilms for such pathogens can be targeted via the extracellular matrix, in particular the two lectins, LecA and LecB. This chapter describes a collaborative project in which the development of a microfluidic flow cell for the purpose of providing a homogenous lectin density surface for in-vitro lectin-targeting liposomes assessment. Devices were produced via a rapid and cost-effective prototyping cycle using a 3D printed mould. Several different configurations were tested with the final design presenting four separate flow cells on one hydrogel coated microscope slide: with dimensions of 1 mm x 0.5 mm x 5.75 mm and a cell volume of 2.825  $\mu\text{L}$ , similar to medium sized capillaries. All the hydrogel covered sections of the channels were coated with either LecA or LecB. Analysis by confocal microscopy confirmed devices produced no background signal. Fluorescent liposomes coated with lectin targeting ligands along with competitive inhibitors (isopropyl  $\beta$ -D-thiogalactoside (IPTG) and L-Fucose) at different concentrations. Devices underwent surface regeneration with EDTA allowing for repetitive uses. Further discussion of lectin targeting liposomes for selective drug delivery to overcome antimicrobial resistance is presented in the published work with O. Metalkina and B. Huck in the Journal of Material Chemistry B.

### 3.2 Introduction *Chapter 3 – Rapidly prototyped 3D printed flow cell the screening of extracellular lectins via glycomimetic liposomes.*

#### 3.2.1 Targeted drug delivery to biofilms

Antimicrobial resistance in bacterium is a rising risk to public health on a global level. As bacteria evolve to survive, so must the methods to eradicate them. One difficulty to overcome is the formation of biofilms by ESKAPE pathogens. *Pseudomonas aeruginosa*, a Gram-negative bacteria, is difficult to treat because of the host immune defence and antibiotic treatment resistant biofilm that forms, creating a self-producing resistance conferring matrix.<sup>108,109</sup> There are five general methods to treat bacteria with antibiotics that focus on inhibiting; cell wall synthesis, protein synthesis, nucleic acid synthesis, or disrupting bacterial metabolism or cell membranes.<sup>110</sup> However, the biofilm reduces the effectiveness of these treatments resulting in need for more specialised treatments.<sup>111</sup> Nanotechnology has provided several methods to improve drug delivery, with liposomes, nano-emulsions, cyclodextrins, metallic nanoparticles and many others being developed over the years.<sup>112,113</sup> Site specific drug delivery has always been of interest with nanostructured lipid carriers, e.g. liposomes, and have been of keen interest as method for improving the efficacy by improving where and how the drug is applied in-vivo, whilst also reducing dosage volumes and side effects.<sup>114–116</sup> In general, liposomes are of interest because of broad physicochemical property range, stability and large volume to surface area ratio. Liposomes are implemented in non-covalent drug encapsulation, a method of delivering an

unmodified drug to a specific location within a liposome that is modified to bind to a specific surface group. Liposomes modified with glycomimetic surface ligands have been reported for a vector for site specific delivery.<sup>117</sup> Lectin type A (LecA) and lectin type B (LecB) contributes to the formation of *P. aeruginosa*<sup>118</sup> therefore liposomes presenting the corresponding carbohydrates to target lectins have also been developed.<sup>119–121</sup>

In-vitro testing is essential to any drug delivery development, especially for the investigation of lectin-carbohydrate interactions. These often require fluorescence assays, enzyme-linked lectin assays or isothermal titration calorimetry.<sup>122</sup> However, multivalence liposomes are prone to aggregation and precipitation, reducing the accuracy of such methods. Surface plasmon resonance assays avoid these issues but are more time-consuming with regards to data evaluation.

### 3.2.2 Microfluidic assay

Microfluidic assays have been an invaluable tool for developing new in-vitro systems, particularly those focusing on biofilm formation in circulatory systems.<sup>123–125</sup> While it is important to ensure the target specific liposomes bind to the correct site; an assay should also model conditions within the body. Specifically, the laminar flow and pressure within a capillary is a result of the high flows but incredibly small channel diameters, resulting in low Reynold numbers.<sup>126</sup> Medium sized arteries inner diameters range from 0.8 mm up to 1.8 mm, with resting heart rates resulting in veins observing flow rates of 1.2 mL/min and arteries observing 3 mL/min.<sup>127</sup> Microfluidics has an extensive history of mimicking these conditions.<sup>128,129</sup>

### 3.3 Theory

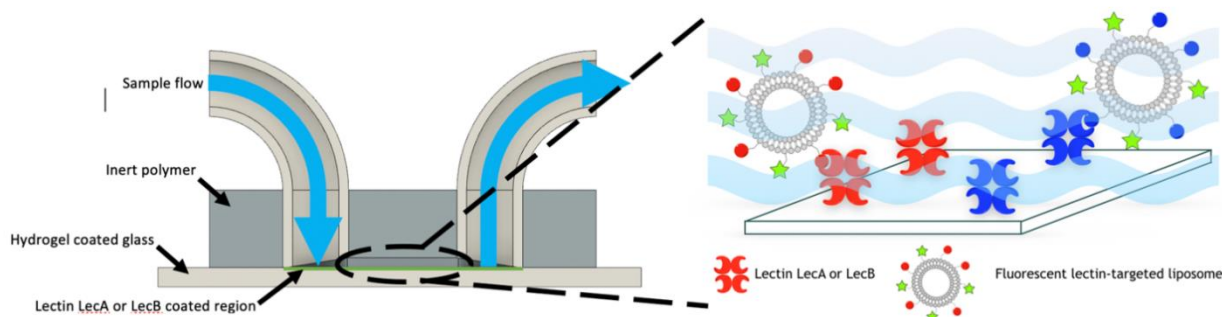


Figure 2.1: Model flow cell device. Hydrogel coated substrate with a bonded channel structure allowing for the selective treatment of the surfaces. Lectin grafting to the hydrogel surface would then allow for the selective targeting of a liposome drug delivery system which could be analysed in-situ.

Microfluidic assays to study biofilm formation, mimicking and drug delivery must control the laminar flow within, as the flow is an influential factor which effects molecular flux, shear stress and concentration gradients in and outside the biofilm.<sup>130–134</sup> Assays that seek to mimic a biofilm for drug delivery screening must also present a surface that consists of the same or similar targeting groups. The application of surface coatings in microfluidics is common.<sup>135–137</sup> For the purpose of this chapter, only hydrogel coatings of PDMS and glass shall be considered. There are two routes to fabricate devices with hydrogel coatings, prior or post fabrication. Post fabrication has the simple method of taking a hydrogel, filling the device, crosslinking the hydrogel in situ, e.g. via UV, and removing the un-crosslinked material.<sup>138,139</sup> Whilst such processes are rapid and

provide an entirely coated surface regardless of the microfluidic chips material, such methods can result in significantly varied coating thickness. Sometimes, a device requires coating on one surface to reduce background noise. Pre-coating hydrogels onto a substrate using spin coating followed by photolithographic methods.<sup>140–142</sup> This provides a uniform and higher resolution hydrogel surface but such fabrication costs more and other fabrication steps could damage the prepared surface.

A device that incorporates both methodologies into one device is considered in Figure 2.1. Taking a bulk hydrogel coated material, bonding a channel structure to the surface, and then performing surface treatments to the inside of the channel. The applied material presenting the channel structure would be inert to the treatment, whilst the hydrogel coated surface would be readily available. This way, a lectin presenting hydrogel surface could be fabricated with an even coating, mimicking a biofilm and in turn allow for the modelling of a selective liposome drug delivery system.

It is with this in mind, a flow cell microfluidic device with hydrogel specifically coated onto one surface was fabricated, acting as another example of how 3D printing can be implemented for rapidly prototyped microfluidic device. The device would then go on to be used for screening fluorescent glycomimetic liposomes binding to surface lectins, mimicking the targeted drug delivery to biofilms modelled to be evenly coated and show no variation in the performance of the lectin-hydrogel coating when comparing neighbouring flow cells.

## 3.4 Experimental

### 3.4.1 Materials

Devices were fabricated using polydimethylsiloxane, as Slygard 184, and black Slygard 170 (Dow Chemical Co., Michigan, USA). Both purchased from Sigma-Aldrich. HC polycarboxylate hydrogel NHS-activated (HCX) glass slides were purchased from XanTec bioanalytics GmbH (Germany). UHU plus endfest 90 min epoxy (UHU GmbH & Co. KG, Germany) was purchased from a commercial supplier. All silicone tubing (ID x OD, 1/16 x 1/8 inch) was purchased from Sigma-Aldrich (produced by Saint-Gobain, USA). Rupture experiments used deionised water with a commercial food dye to aid visualisation. Description of liposome synthesis and experimentation is described in the attached manuscript written with O. Metalkina and B. Huck.

### 3.4.2 Equipment

3D computer aided drawings were drawn on Autodesk Fusion 360 (Autodesk, USA), exported as .STL files and sliced into GCode by Ultimaker Cura (Ultimaker, Netherlands) and printed using a fused filament 3D printer (Ultimaker2 Extended+, Ultimaker, Netherlands) fitted with a 0.25 mm nozzle. The print speed was 20 mm/s, layer height was 0.1 mm, print temperature was 210 °C, bed temperature was set to 60 °C. A PICO low pressure plasma system (Diener Electronic GmbH & Co. KG, Germany) was used for the plasma treatment of PDMS. Description of equipment used for confocal and surface plasmon resonance experimentation is described in the attached manuscript written with O. Metalkina and B. Huck.

### 3.4.3 Chip Fabrication

Moulds were fabricated by the direct 3D printing of PLA onto cleaned microscope slides. The print height of the first layer was adjusted by the height of the microscope slide used, approximately 1

mm plus 10  $\mu\text{m}$  for nozzle clearance. The total print time for the mould was 51 minutes using the Ultimaker2 Extended+. An outer ring was printed at first to hold the microscope in place. The print was timed and stopped at 11 minutes. The slide would then be manually loaded into the support ring and the print resumed. Once the heating, cooling and outer frame components were optimised, these were printed using thicker more durable magnetic PLA parts. Magnetic parts are placed on top of the 3D printed mould and aligned on custom 3D printed alignment bed with imbedded magnets. The PLA outer ring was sealed in place using hot glue to avoid leakage. PDMS was prepared in a 10:1 ratio (polymer:crosslinker) by weight, degassed, and poured into the mould. The PDMS was left to cure overnight at 40 °C. The PDMS was peeled off the mould and cleaned with deionised water and isopropanol. Once dry, the PDMS was plasma treated with pure oxygen at 350 W for 1 minute and immediately brought into contact with the HCX slide. The PDMS-glass device was then placed under a 2 kg mass and baked for 2 hours at 40 °C. Epoxy was used as a sealant around the PDMS-glass edge to improve device durability. The droplet channel was cleaned with deionised water and isopropanol and air dried. Silicone tubing was inserted into the devices inlets and outlets and sealed in place by black PDMS.

### 3.5 Results

#### 3.5.1 Chip configuration optimisations

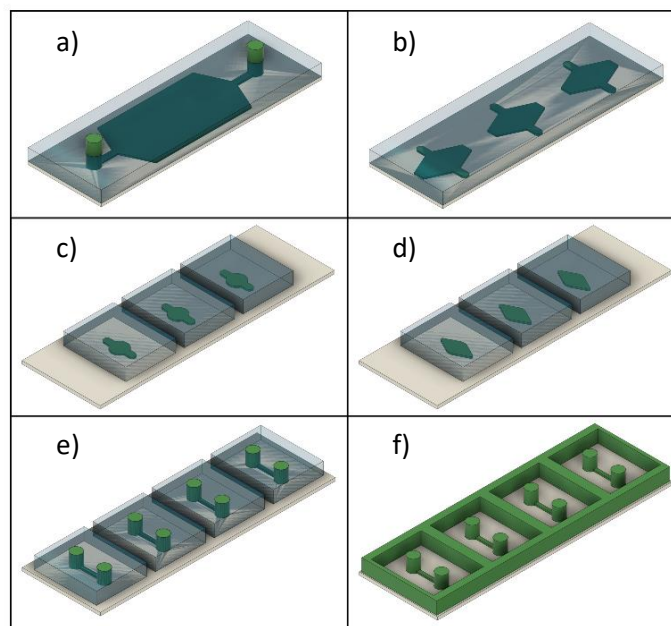


Figure 2.2: Chip models and final mould. White material = microscope slide, green = 3D printed mould and resultant chamber, blue = PDMS. a) Initial design – Chamber dimensions (CD) = 20 mm x 32.5 mm x 0.5 mm. b) Three in one PDMS block – CD = 9.5 mm x 16.5 mm x 0.5 mm. c) Separation of circular chambered flow cells – CD = Diameter = 5 mm and thickness = 0.5 mm. d) Diamond variation of c). Widest point = 5 mm, outlet diameter = 2 mm and thickness = 0.5 mm. e) Final design – CD = 5.75 mm x 1 mm x 0.5 mm. Outlet diameter = 3.4 mm. f) 3D printed mould used in chip fabrication. Bulk structure is the PDMS block mould. Outer dimensions are 74.4 mm x 24 mm x 4 mm. The inner blocks were 16 mm x 20 mm x 4 mm. Detailed schematic provided in Support figure 2.1 to 2.3.

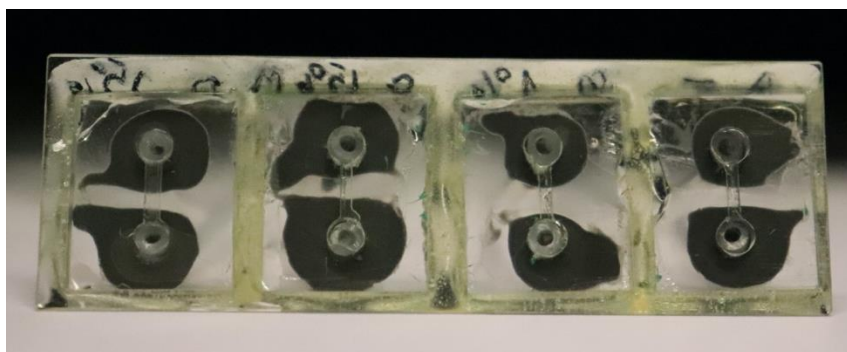


Figure 2.3: Picture of the fabricated device observed from the glass side. The device was fabricated from the mould shown in Figure 2.2f). Here the epoxy sealant can be observed as well as the Black PDMS used to seal the tubing in place. Max flow rate for normal glass-PDMS devices was 38 mL/min, (<https://youtu.be/i5rrJARfj0g>) but found to be 2.4 mL/min with the hydrogel covered slides.

Chip development was performed using a rapid iterative design approach. Each mould, shown in Figure 2.2, was fabricated, and assessed upon the performance and improved upon per design. From a) to b), the number of flow cells increased to allow for more tests to be performed upon the same hydrogel/lectin density. The key development of b) to c) was the separation of the flow cells. This removed an observed flow between flow cells as well as ensuring that a rupturing in one flow cell did not disrupt the operation of another flow cell. Different tubing that was, at the time, more compatible was suggested, hence the transition of the outlet size between c) to d). The change to the diamond shape was to remove the roughness caused by a circular path the print head would take. The design improved further when larger tubing was implemented and 4 flow cells were fabricated onto one slide, d) to e) and f). The flow cells also took a rectangular shape, Figure 2.3. It was found the larger channels could withstand higher flow rates and less irregular flow patterns. Smaller flow cells would fill as per the path tool roughness, where the ridges would act as phase guides. Max flow rate for normal glass-PDMS devices was 38 mL/min but found to be 2.4 mL/min when implementing the hydrogel covered microscope slides. All liposome testing was performed at 500  $\mu\text{L}/\text{min}$  and experienced laminar flow.

### 3.5.2 Lectin targeting liposome targeting on fabricated flow cells.

The device performed as expected with regards to the targeted liposomes binding to lectin modified surface. As shown by Figure 2.4 and 2.5, the control channels showed negligible signal, whilst the experimental channels demonstrated that increasing the targeting liposome concentration increased the signal. Lectin-liposome binding was reported to be highly stable as the signal remained constant after 1 hour of washing with buffer. For the LecA chip, the competitive inhibitor Isopropyl  $\beta$ -D-thiogalactoside (IPTG) was flowed through the different channels at different concentrations to access the carbohydrate-dependency of the targeting process. The same was repeated for LecB using the inhibitor L-fucose. As the concentration of the inhibitor increases, the more liposomes are displaced as expected to prior theory and literature. The device was unable to quantify the binding affinity, so additional experimentation using a surface plasmon resonance (SPR) biosensor assay was performed. This is not a weakness of the device demonstrated within this chapter, as it was not designed to assess the kinetic or the thermodynamic parameters of liposome-ligand binding, simply to provide a cheap and rapid method to fabricate a device that could allow for qualitative assessment of the liposome; thus provide an inclination for the potential of the synthesised liposomes. It also provided an

opportunity to observe LecA's affinity to form aggregates within the flow cell, an issue that would persist throughout SPR experimentation but could be negated.

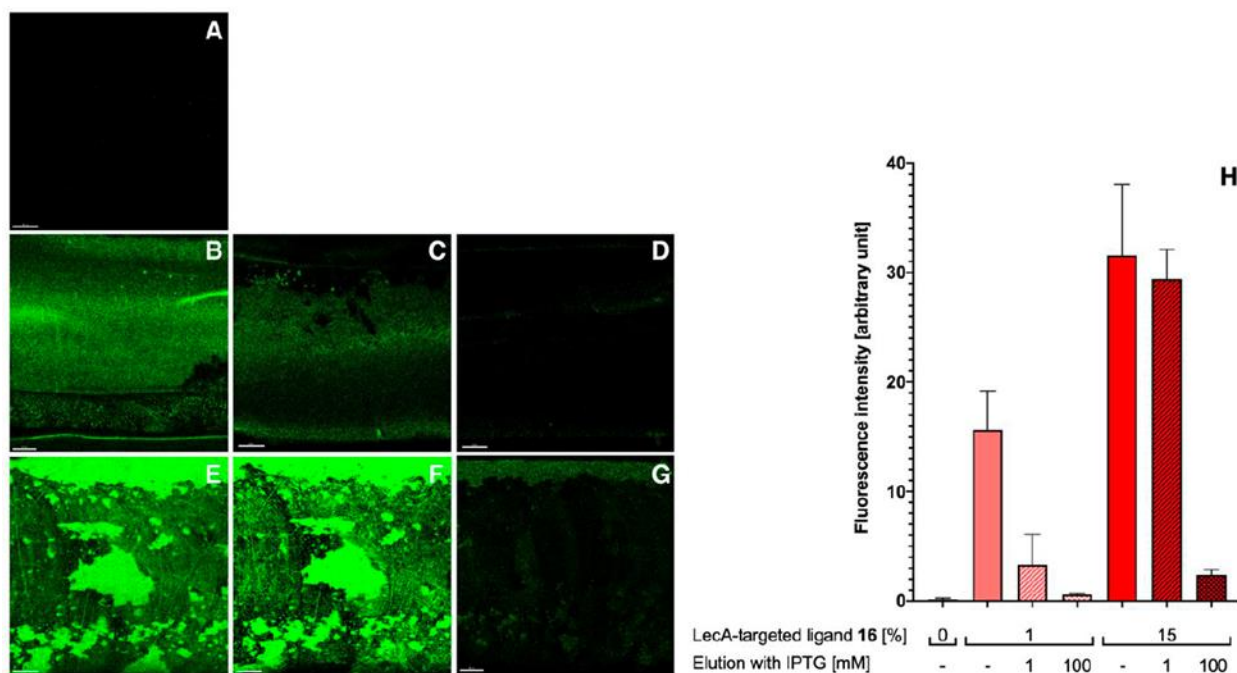


Figure 2.4: Targeting liposomes to a LecA-coated surface under flow. Injection of liposomes (5 min) and analysis by confocal microscopy after washing out unbound liposomes with buffer (5 min): Fluorescent liposomes without targeting ligand (A); fluorescent liposomes with 1% LecA-targeted phospholipid 16 (B); fluorescent liposomes with 1% LecA-targeted phospholipid 16 eluted with 1 mM IPTG (C) and 100 mM IPTG (D); fluorescent liposomes with 15% LecA-targeted phospholipid 16 (E); fluorescent liposomes with 15% LecA-targeted phospholipid after elution with 1 mM IPTG (F) and 100 mM IPTG (G); quantification of the interaction between LecA-targeted liposomes with LecA-modified surface under flow conditions. Averages from 3 independent experiments with 9–12 technical replicates, error bars correspond to standard deviation. For A-G: scale bar = 50  $\mu$ m.

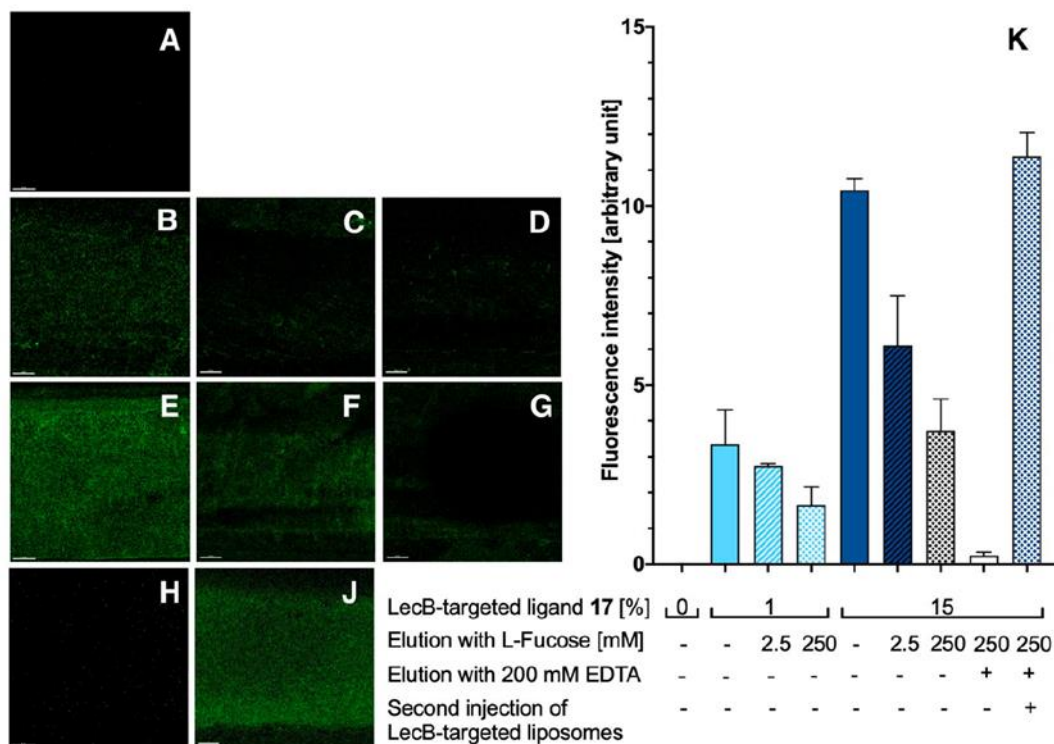


Figure 2.5: Targeting liposomes to a LecB-coated surface under flow. Injection of liposomes (5 min) and analysis by confocal microscopy after washing out unbound liposomes with buffer (5 min): Fluorescent liposomes without targeting ligand (A); fluorescent liposomes with 1% LecB-targeted phospholipid 17 (B); fluorescent liposomes with 1% LecB-targeted phospholipid 17 eluted with 2.5 mM L-fucose (C) and 250 mM L-fucose (D); fluorescent liposomes with 15% LecB-targeted phospholipid 17 (E); fluorescent liposomes with 15% LecB-targeted phospholipid 17 after elution with 250 mM L-fucose for 5 min (F) and 10 min (G); fluorescent liposomes with 15% LecB-targeted phospholipid 17 eluted with 200 mM EDTA to regenerate the glass surface (H); regenerated chamber after equilibration with PBS/Ca for 10 min and repeated injection of the liposomes with 15% LecB10 targeted phospholipid 17 (J); quantification of the fluorescence image analyses to assess the interaction between LecB-targeted liposomes with LecB-coated surface using the microfluidic device (K). Averages from 3 independent experiments with 9-12 technical replicates, error bars correspond to standard deviation. Scale bars correspond to 50  $\mu\text{m}$ .

### 3.6 Discussion

As previously discussed in Chapter 2, rapid prototyping allows for the development of novel designs at a significantly reduced cost. It also allows for the inclusion of structures that are far more difficult to produce via typical methodologies, such as the pillars that would provide holes for the inlet and outlet tubing. Original iterations of the designs relied upon using sample punches to carve out the inlet and outlet tubing holes. Original flow cell designs were thin, wide, and only one flow cell per slide, Figure 2.2 a). Such a wide and thin channel was prone to collapsing. From A to F, the design progressed to allow for more flow cells per slide, separation of the flow cells so that the rupturing of one would not affect the others, inclusion of the inlet and outlet holes to reduce positional and size variation from cutting the holes out and constant channel size to allow for uniform flow and internal pressure across the flow cell, Figure 2.2 e) and f). Such variations are possible with other technologies, however these result in the need for additional moulds (SU-8, hot press stamps, etc.), which incur additional production time and costs. 3D printing allowed for the design of the flow cell to change several times from day to day.

One major concern around the device was about the adhesion between the plasma treated PDMS and the hydrogel coated glass. Typically, both would be plasma treated so that both surfaces present reactive groups to form covalent bonds. Higher degrees of bonding results in more stable devices that can withstand higher flow rates and pressures. However, the fabricated devices would have a reduced adhesion due to the lowered degree of bonding; as plasma treatment of the HCX hydrogel slides would result in degradation of the hydrogel functional groups, resulting in a decrease in lectin density. Microfluidic systems that seek to mimic the flow rates within the body must be able to withstand similar or the same flow rate observed in the body, which is considered high. Early designs suffered from having a smaller flow cell volume, which in turned increased the internal pressure to the point of rupture. The final design overcame this by having a larger flow cell volume that was still comparable with medium sized capillaries. The device ruptured when flow rates exceeded 2.4 mL/min. Comparatively sized arteries experience blood flow rates up to 3 mL/min whilst veins experience 1.2 mL/min at a resting heart rate. Therefore, the model is comparative to medium sized veins. The epoxy sealant around the flow cell reduced lift off and peeling effects by providing a rigid protective structure around the edge.

### 3.7 Conclusions

In conclusion, a rapid prototyped flow cell was fabricated using a 3D printed mould, which was rapidly and iteratively developed. Four separate flow cells were bonded onto one hydrogel coated microscope slide. Flow cell dimensions were 1 mm x 0.5 mm x 5.75 mm with a volume of 2.825  $\mu$ L, similar to medium sized capillaries. Max flow rates of 2.4 mL/min were observed, which is similar to similar sized arteries *in-vivo*. All of the hydrogel covered sections of the channels were coated with either LecA or LecB, allowing for one control and three experimental flow cells. Analysis by confocal microscopy confirmed devices produced no background signal. Fluorescent liposomes coated with lectin targeting ligands were then passed over the lectin surface at different concentrations and stable for over one hour. Competitive inhibitors (IPTG and L-Fucose) were passed through at different concentrations to demonstrate the dissociation. EDTA was applied to the LecB sample and liposomes were reapplied, demonstrating the regeneration of the surface allowing for repetitive uses. These flow cells demonstrate a strong ability for rapid screening; whilst further information, such as binding affinity, requires additional more complex experimentation.

Such rapidly and cost-effective devices that also provide an accurate qualitative model are an essential tool for the evaluation of drug delivery systems *in-vitro*. Lectin targeting liposomes provide a promising method of selective drug delivery to overcome antimicrobial resistance, and a greater discussion of the synthetic chemistry and drug delivery implications of these are presented in the published work with O. Metalkina and B. Huck in the Journal of Material Chemistry B.

## Chapter 4 – Three-dimensional bioinspired intertwining channel multiplexed droplet generator.

(Patent title: Monodisperse micro droplet producing device and method of producing the same as.)

### 4.1 Abstract

One of the largest limitations facing the development of microfluidics is the restriction upon two-dimensional design and fabrication methodologies. This chapter discusses the application of 3D printing as a method to produce microfluidic devices featuring 3D structures. A planar 2D device that was adapted from Chapter 2. This device could produce water in oil droplets that were  $371 \pm 25 \mu\text{m}$  using  $Q_{\text{Oil}}$  of 1.5 mL/min and  $Q_{\text{Water}}$  of 0.2 mL/min, at a rate of  $16 \pm 1$  droplets per second. Temperatures of 31 °C and 17 °C were achieved within the integrated heating and cooling channels. The world's first truly 3D multiplexed (64) cross-flow droplet generator with bioinspired intertwined features was fabricated with the same technique and tested. A simplified single focus flow droplet generating device was also fabricated and produced droplets sized  $311 \pm 16 \mu\text{m}$ , when  $Q_{\text{Oil}}$  of 0.15 mL/min and  $Q_{\text{Water}}$  of 0.02 mL/min are used, producing  $8 \pm 1$  droplets per second. It is predicted that the 64 cross-flow droplet generator device would require  $Q_{\text{oil}}$  of 9.6 mL/min and  $Q_{\text{Water}}$  of 1.28 mL/min to produce 512 droplets per second. Addition of the 3D features allows for unprecedented multiplexing and channel density never seen in previous cross-flow droplet generators and is essential to the future of multiplexing microfluidics to further increase the through-put.

### 4.2 Introduction

Microfluidic design inherited the same two-dimensional (2D) design practises as electronic silicon wafer design. Both implement photolithographic methods to apply a structure onto or into a substrate. Alternatively, embossing, soft lithographic moulding, injection moulding, computer numerical control (CNC) milling, etc. can be utilised. All these methods can produce micro-structured devices with high resolutions and through-put, making microfluidic tools invaluable within research. Droplet generation is a common process used to create regimented nano/pico-litre volumes which can be implemented for molecule synthesis, chemical reactions, imaging, cell encapsulation, drug discovery and delivery, diagnostics, food sciences, cell biology, and many other applications.<sup>143</sup> However, microfluidics has seen limited implementation on an industrial scale despite the opportunities of continuous production methods.<sup>144</sup> Industrial processes typically implement parallel systems or systems in serial to multiplex production.<sup>145</sup> Serialised microfluidic systems have been demonstrated but these are limited in application.<sup>146,147</sup>

2D parallel systems have also been demonstrated, where multiple droplet generating junctions are present on one device.<sup>148–151</sup> Alternatively, membranes have been implemented for droplet generation (membrane emulsification) to increase through-put but mainly focuses on nanoparticle synthesis and have previously suffered from greater variation in produced droplets until recently.<sup>68,152–154</sup> Cross flow, co-flow and focus flow devices have a significantly reduced dispersity but are limited in a 2D space. 2D microfluidic droplet generators cannot cross oil and water channels in the same way circuit boards cannot cross wires. To overcome this major limitation, developments have been made to feature structures that also vary in three dimensions (3D), labelled as 3D microfluidic devices. 3D devices are defined as having different channel

heights or structures on different discrete layers within the same device. Such structures are either fabricated with selective etching with different masks, requiring mask alignments, or stacked 2D structured layers with connecting vertical channels.<sup>155–158</sup> Previously successful published work implemented soft lithography of PDMS to produce stacked 2D structured layers to produce droplets, transverse upwards and then mixed with a cross-linking agent to generate sub-100  $\mu\text{m}$  cell-laden microgels with low dispersity.<sup>159</sup> Commercialised parallel droplet generators are available using stacked 2D structures (Micronit DGFF.P8.75). These stacked droplet generators, whilst performing incredibly well, beget the question “What is a truly 3D microfluidic structure?” In theory, the same function could be performed by two separate chips with connective tubing between them. Directly stacking these structures is not conducive to the fundamental operation of the device.

3D printing technologies have been improving to the point where microfluidic devices can be fabricated as one whole piece. Fused deposition modelling (FDM) printers have been implemented to rapidly generate microfluidic devices<sup>160–163</sup>, but these often suffer from rough surfaces, particularly in the vertical direction.<sup>164</sup> These devices are easy to produce, require little post production treatment and can be rapidly produced, but the resolution is limited by the size of the nozzle used and improper overlap of the filament can result in a porous device prone to leaking. The smallest commercial nozzle available is 100  $\mu\text{m}$ , which is considered a large characteristic dimension in terms of microfluidic resolution. Alternative printers are available and have been utilised to generate 3D micro-droplet generators. One noteworthy group is the work by G. Nordin et.al. The group focuses on using a digital light processing (DLP) printer. While demonstrating well defined channel diameters, 18  $\mu\text{m}$  x 20  $\mu\text{m}$ <sup>165</sup>, the group were capable of producing a co-flow droplet generator.<sup>166</sup> Additionally, stereolithographic (SLA) printers have also been implemented for other microfluidic systems as well as droplet generators of varying configurations, droplet size and channel resolution.<sup>85,167–169</sup> A wide range of materials are available with different hydrophobicity, the devices have higher yield pressure limits and higher resolution than FDM and DLP printers, when comparing entry to mid-range commercial devices. The optical transparency of SLA prints is much higher than FDM prints due to the higher resolution and reduced surface roughness, which is essential for observations within the device. One drawback of SLA and DLP printers is the prepolymer mixtures biocompatibility, as these resin mixtures contain cytotoxic radicals. Therefore, fabricated devices must undergo more postproduction treatment to reduce contamination with untreated resin.

This chapter seeks to overcome the discussed design and fabrication limitations associated with 2D microfabrication technologies with 3D printing. Droplet generation, as previously discussed in Chapter 2, will be used as an example function as it is often in limited in terms of parallelisation.

### 4.3 Theory

Bahrami et.al. used the Navier-Stokes equation, reduced to Poisson’s equation, to define the pressure drop,  $\Delta p$  ( $\text{kg m}^{-1} \text{s}^{-2}$ ), across a rectangular channel as:

$$\Delta p = \frac{\mu \varepsilon L Q}{4c^4 \times (1/3 - 64\varepsilon t / \pi^5)} \quad (\text{Eq. 4.1})$$

Where,  $\mu$  is the fluid viscosity ( $\text{kg m}^{-1} \text{s}^{-1}$ ),  $\varepsilon$  is the channel width:height ratio,  $L$  is microchannel length (m),  $Q$  is flow rate ( $\text{m}^3 \text{s}^{-1}$ ),  $c$  is the half height of the channel (m) and  $t$  equals  $\tanh(\pi/2\varepsilon)$ .

For this work, one should consider the channels to be perfectly square (where  $\epsilon = 1$ ). The narrower (lowering  $c$ ) or longer capillary (increasing  $L$ ), the greater the pressure drop across a capillary. It was also stated that the cross sectional square root of the area is a better characteristic length than hydrodynamic diameter.<sup>170</sup> Additionally, logarithmic  $\Delta p$  has a negative linear relationship to the logarithmic Reynolds number. The Reynolds increases proportionally with increasing channel length, therefore longer capillaries experience a greater pressure drop. Division of channels into equally sized daughter channels results in a proportional division of the flow and pressure drop.<sup>171,172</sup> The sum of the pressures across the daughter channels is equal to the outlet pressure of the first channel. Therefore, the regular division and scaling of characteristic length allows for the production of a multi-outlet device with predictable flow behaviours regardless of if the multiplexing microfluidic device present 2D or 3D structures.

A droplet generating device requires at least one continuous channel for every discontinuous channel. This ratio increases 2:1 for focus flow devices. When considering the parallelisation of a droplet device, the degree of splitting must be considered. Quaternary splitting results in a scale that increases exponentially with the splitting of each channel. The first inlet channel, the 0<sup>th</sup> generation and all following generations ( $n$ ) follow a geometric pattern:

$$\text{Number of channels in a generation} = S \cdot S^{n-1} \quad (\text{Eq. 4.2})$$

where  $S$  is a splitting factor and  $n$  being the generation of splitting, with the first singular channel being generation 0. Therefore, a system that would split each channel into four ( $S=4$ ), would result a 1:4:16:64:256... splitting pattern. The angle between each generation of channels ( $\beta$ ) is given by:

$$\beta = \frac{360}{S} \quad (\text{Eq. 4.3})$$

For the quaternary pattern, this equates to 90°. An entwined structure must have an axially rotated secondary channel structure that is offset by the primary structure ( $\Delta$ ) given by:

$$\Delta = \frac{\beta}{2} \quad (\text{Eq. 4.4})$$

The characteristic length of a given generation channel ( $L_n$ ) is given by:

$$L_n = \frac{L_0}{2^{n-1}} \quad (\text{Eq. 4.5})$$

where  $L_0$  is the characteristic length of the first channel. Therefore, if the input channel is 8 mm in diameter, then the resultant generations would be 4 mm, 2 mm, 1 mm, 500  $\mu\text{m}$ , etc. It is with this understanding of pressure drop across a system, geometric sequences, and additive assembly that a truly 3D droplet generator can be considered. The following presents some conceptual and prototyped structures to overcome the current limitations in 2D microfluidic design and fabrication.

## 4.4 Experimental

### 4.4.1 Materials

Devices were produced using either “Black V4” or “Clear v4” SLA Resin (FormLabs, USA). UHU plus endfest 90 min (UHU GmbH & Co. KG, Germany) was purchased from a commercial supplier. All silicone tubing (ID x OD, 1/16 x 1/8 inch) was purchased from Sigma-Aldrich (produced by Saint-Gobain, USA). Water in oil droplet generation experiments used deionised water with a commercial food dye to aid visualisation. Oil in water droplet generation experiments used silicone oil, 350 cSt (25 °C) mixed with commercial engine oil dye to aid visualisation and deionised water. The droplet generating chamber was fabricated using 2.9 mm thick acrylic sheets and silicone caulk purchased from a commercial supplier.

### 4.4.2 Equipment

3D printed elements were drawn using the computer aided design (CAD) software Autodesk Fusion 360, Autodesk, USA. These were exported as .STL files and sliced into GCode using PreForm, FormLabs, USA. The GCode was then printed using a FormLabs 3 stereolithographic printer, FormLabs, USA. All devices were printed using a layer thickness of 0.025 mm and touchpoint size of 0.6 mm. Devices were washed using isopropanol in a Form Wash, FormLabs, USA. Two separate Aladdin syringe pumps, AL-2000, World precision instruments, USA were used for the injection of oil and water into the Micronit and fabricated devices. Water heating and cooling control systems used separate peristaltic pumps, Masterflex® Ismatec® REGLO 78018-10, Avantor®, USA. Microscope images were captured using a Stemi 508, Zeiss, Germany coupled with a digital single-lens reflex (DSLR) camera, EOS 80D, Canon, Japan, for single image collection and a mobile phone camera, 10E, Samsung, South Korea, for 960 frames per second video capture.

### 4.4.3 Device design

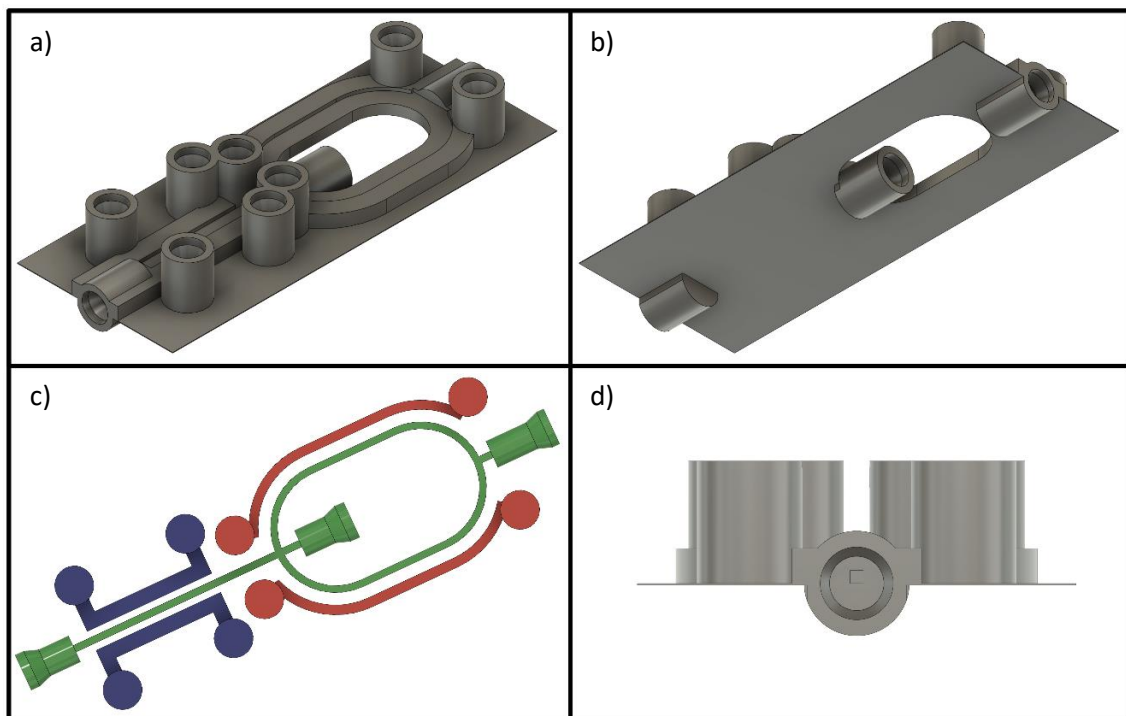


Figure 3.1: CAD of the transparent planar microfluidic droplet generation chip based on the design of the droplet generator described in Chapter 2. Green represents the water and oil channel; red represents heating channels and blue represents cooling channels. a) View of

the device from above; b) View of the device from below (the observation side) and c) The internal structure of the droplet generation channel. Heating channel and cooling channel; d) The profile of the side outlet. Detailed schematics given by Support Figures 3.1-3.3.

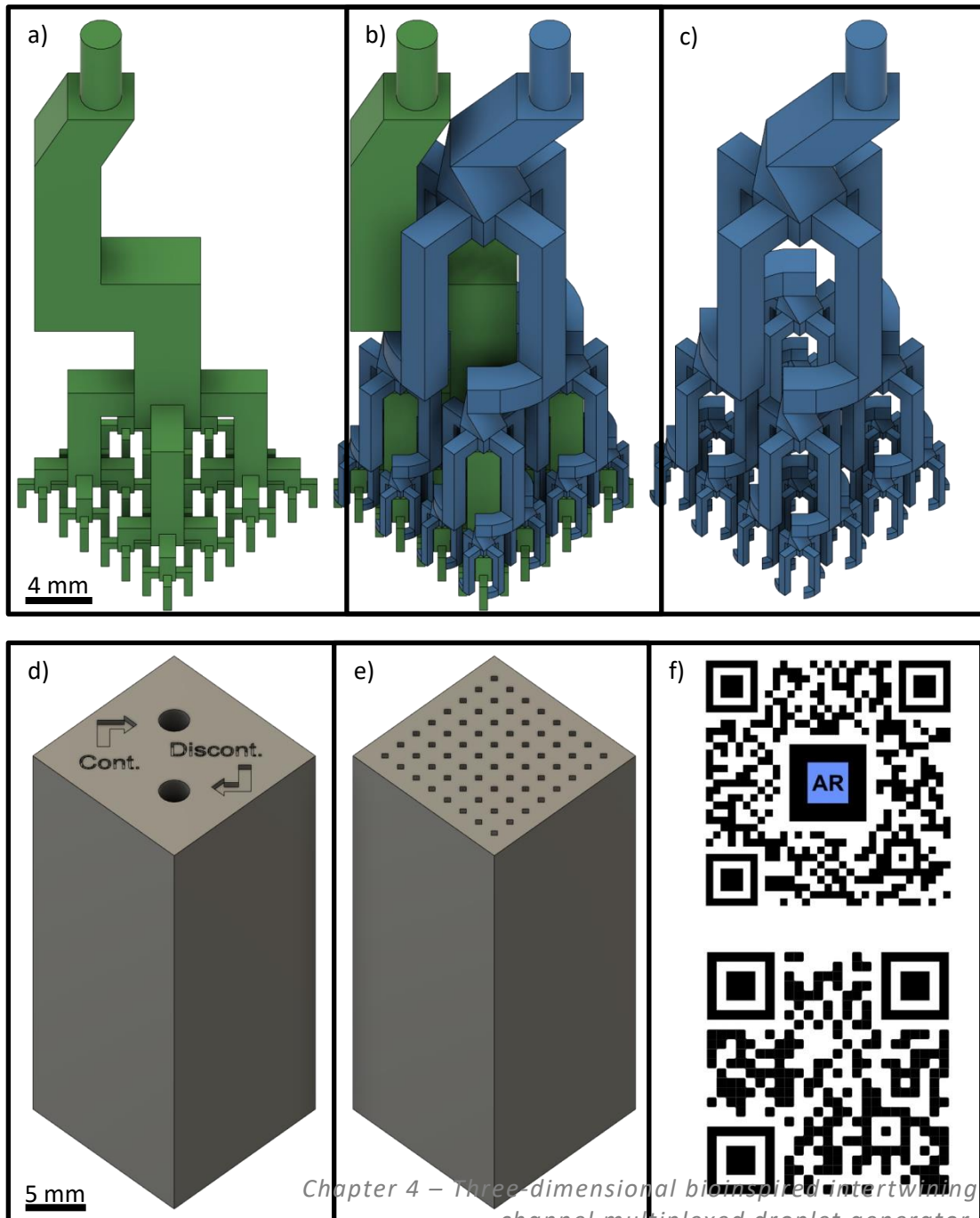


Figure 3.2: a) Continuous phase channel structure. b) Complete intertwining structure of the continuous and discontinuous phase channels. c) Discontinuous phase channel structure. d) Inlet side of the 64-intersection droplet generator. e) 64 outlet side of the 64-intersection droplet generator. f) AR code of the internal structure (<https://ar-code.com/iix8FwSOf>) and QR code for an animation showing the internal structure within device (<https://youtu.be/5tvq507b93E>). Detailed dimensions given by Support Figures 3.4-3.13.

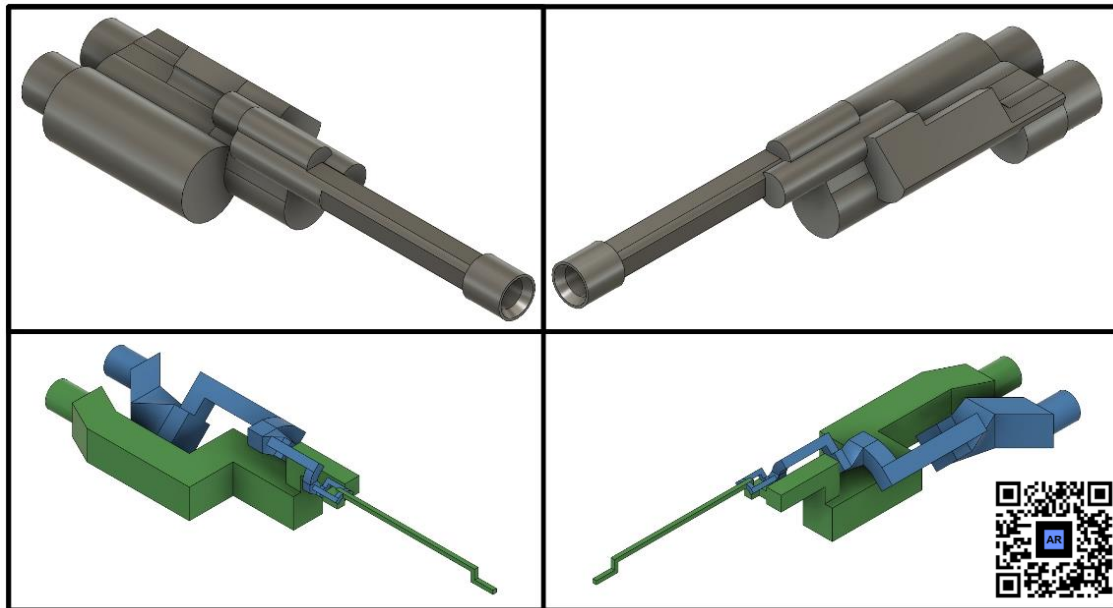


Figure 3.3: CAD of simplified 3D microfluidic chip. Only one focus flow generator is present in the device. The outlet channel is much longer to promote droplet generation within the device and allow for the observation of the droplet generation. a) and b) The body of the device and the model that would be sliced and 3D printed. c) and d) Water (green) and oil (blue) channels within the device. AR code for the internal channel structure (<https://ar-code.com/3jbm8xUYh>). Detailed dimensions given by Support Figures 3.14-3.19.

#### 4.4.4 Device Fabrication

The three different devices (Figure 3.1-3.3) were designed in Autodesk Fusion 360 and printed using the Form 3 SLA printer. Print settings used were predetermined by the slicing software based on which material was used. The 64 and 3D singular droplet generators were printed at a 45° to allow draining and avoid blocking. Planar devices were printed at either 45° or 0° as the larger channels did not block. Planar devices were printed “upside down” so that the flat was smoother and had no support touch points on the surface. Touch points were edited to ensure the surface was clear for better observations. Devices were then washed using isopropanol in a Form Wash for 20 minutes. Devices were then inspected and rinsed with isopropanol and dried with compressed air until no residue resin was observed. Tubing was then glued directly into the device using epoxy. Isopropanol was then rinsed through the devices again and dried.

## 4.5 Results

### Chapter 4.5.1 – Planar 3D printed device

#### 4.5.1 Planar 3D printed device

Figure 3.4 shows a planar device that was produced using SLA printing. Square channels were designed to be 750  $\mu\text{m}$  by 750  $\mu\text{m}$  in dimension. Actual channels were  $700 \pm 14 \mu\text{m}$  in heights and  $700 \pm 4 \mu\text{m}$  in width. Over curing occurs resulting in channels variation, particularly for the top of the channel. The devices were washed and used without any further treatment. This meant that the “smooth” surface was still too rough to clearly observe droplet generation through it. To mitigate this, a droplet of oil and cover slip was placed over the intersection and 1.5 cm after the intersection, allowing for clearer but not perfect observation through the device. The material was only 1 mm thick, well within the working range of the microscope.

Water in oil droplets produced within the device, Figure 3.5, and measured  $371 \pm 25 \mu\text{m}$  ( $n = 100$ ) in size at an oil flow rate ( $Q_{\text{oil}}$ ) of 1.5 mL/min and water flow rate ( $Q_{\text{water}}$ ) of 0.2 mL/min ( $\phi = 0.13$ ), Figure 3.6. Droplets were produced at a rate of  $16 \pm 1$  droplets per second. Devices also featured similar heating and cooling channels as the gelatin droplet devices described in Chapter 2. 70 °C heating water was pumped through the heating channels at 0.45 mL/min and 31 °C was observed. -10 °C cooling salt water was pumped through the heating channels at 0.45 mL/min and 17 °C was observed, Figure 3.7.

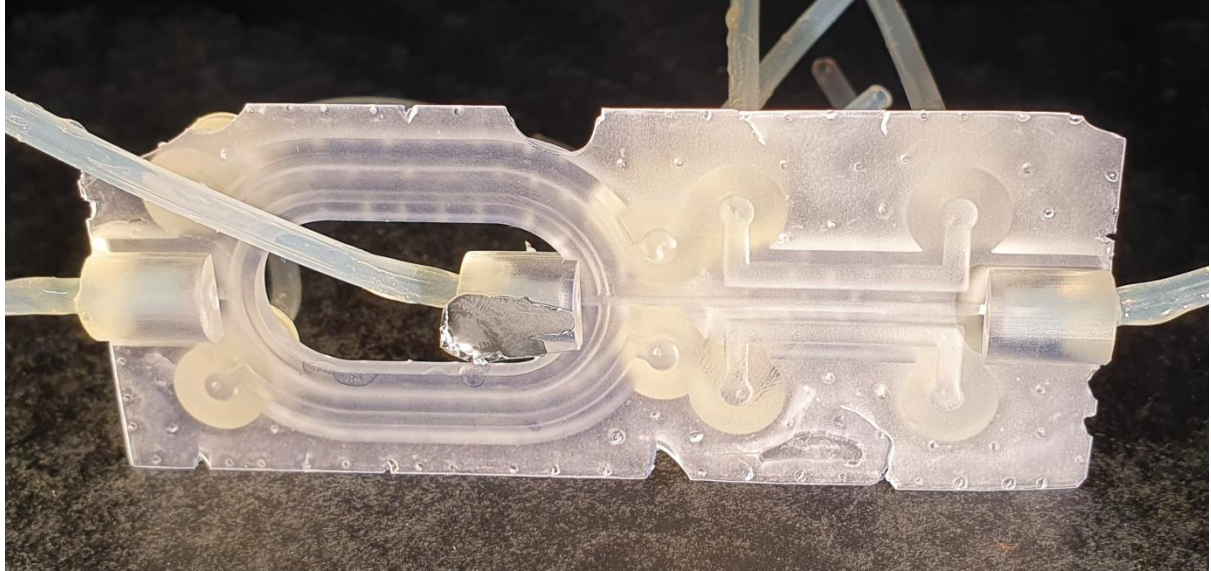


*Figure 3.4: Transparent planar microfluidic droplet generation chip. Device imprint was 61.8 mm x 25 mm x 10 mm. Device was printed at a 45° degree angle and heating and cooling channel inlet/outlets facing towards the build plate, hence the touch points observed. Droplet generation was observed through the smoother surface.*

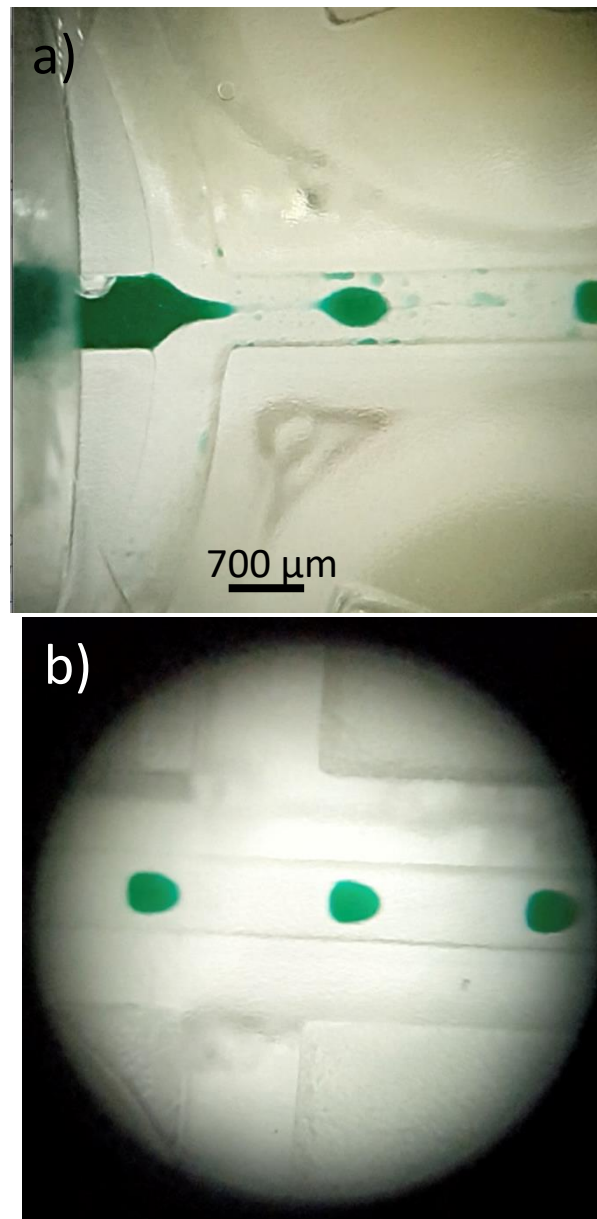


Figure 3.5: Transparent planar microfluidic droplet generation chip intersection. Channel dimensions were designed to be  $750 \times 750 \mu\text{m}$  square in cross-sectional diameter. Over curing occurs resulting in channels of  $700 \pm 10 \times 700 \pm 10 \mu\text{m}$ . a) Planar droplet generation intersection. Video of intersection under operation: <https://youtu.be/gutuP9HvnQw> b) Droplets in the channel 1.5 cm from droplet generation. Video of droplets flowing down the channel: <https://youtu.be/BecXAQHlhqA>

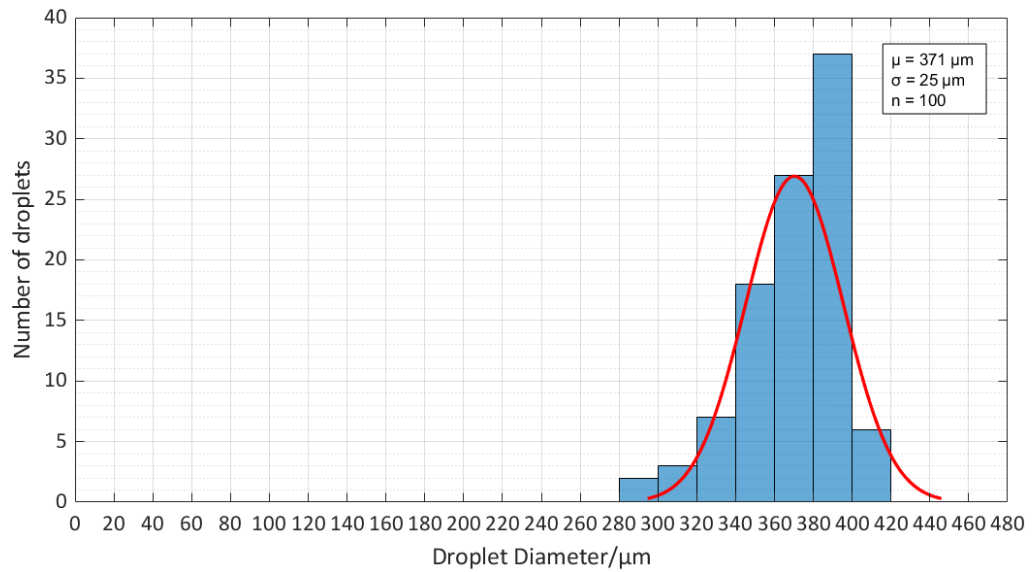


Figure 3.6: Size distribution of droplets produced in the 3D printed planar device at  $Q_{oil} = 1.5 \text{ mL/min}$  and  $Q_{water} = 0.2 \text{ mL/min}$ . Mean diameter equals  $91 \pm 25 \mu\text{m}$ ,  $n = 145$ .

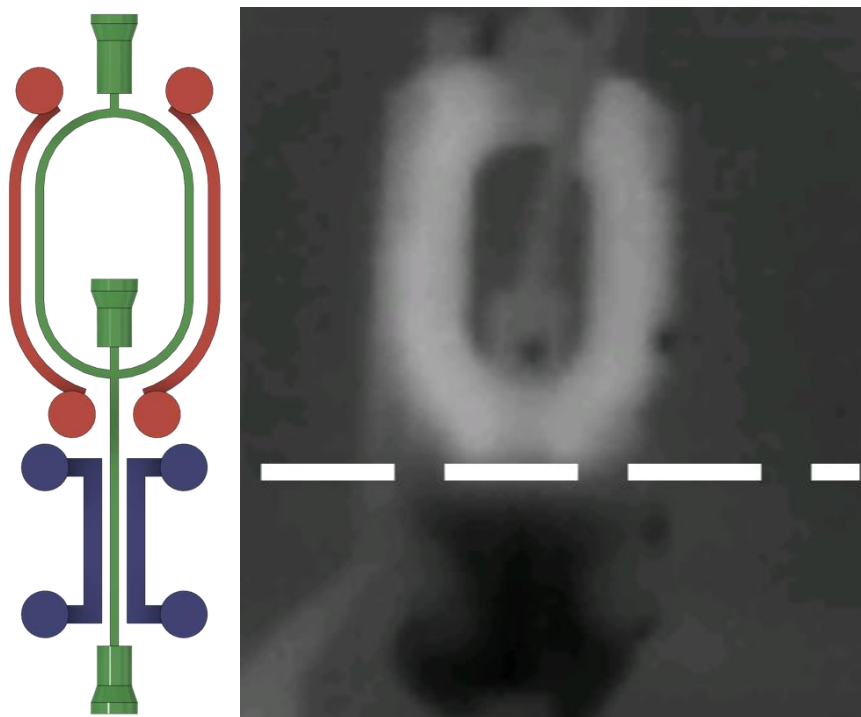
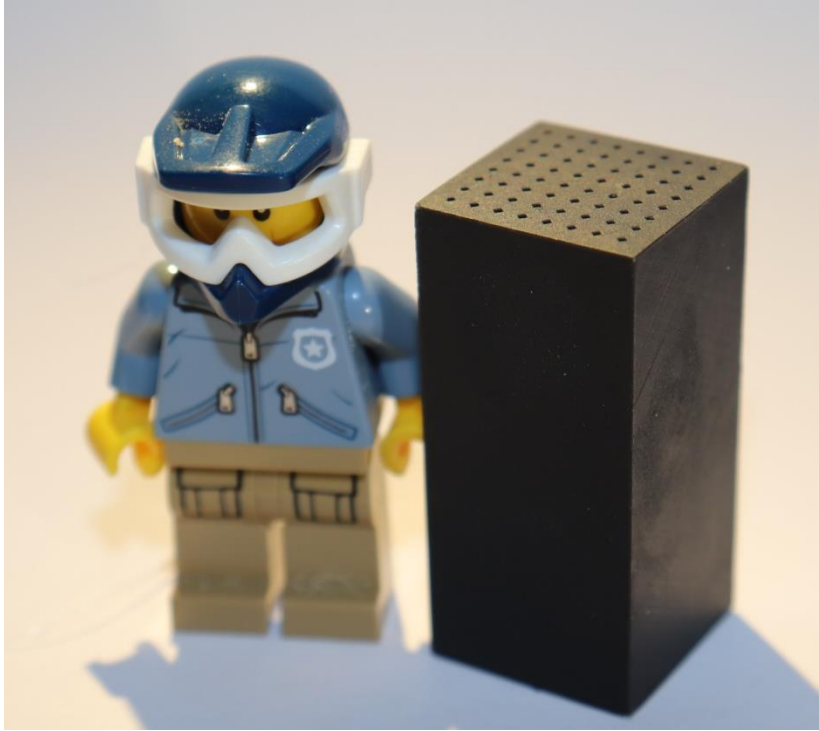


Figure 3.7: FLIR image of 3D printed planar device during hot and cold water pumping. Heated region (above dashed line) equals  $31 \text{ }^\circ\text{C}$  and cooled region (below dashed line) equals  $17 \text{ }^\circ\text{C}$ .

#### 4.5.2 3D printed 64 outlet device with intertwining channels

The 64 cross-flow droplet generator was produced as described and measured  $16 \text{ mm} \times 16 \text{ mm} \times 35 \text{ mm}$  with square outlets of  $500 \mu\text{m} \times 500 \mu\text{m}$ , Figure 3.8. Compressed air was flowed through the device to confirm that all the channels were open, Figure 3.9. At  $1 \text{ kPa}$ , air flow was observed from all outlets. As the air flow decreased, so did the number of air bubbles and the turbulence observed within the channel. At  $0.01 \text{ kPa}$ , only one channel shows a constant air flow. This

demonstrates that there must be variation within the channels so that at low pressures, the channel with least resistance is most favoured. Therefore, higher pressures must be used for droplet generation so that all channels would be under the same pressure and flow at the same rate. This experiment also demonstrated the importance of priming the device prior to use. Air had to be flowed through the device prior to the chamber being filled with water. Otherwise, water could enter the device and causing air bubbles to be trapped within, altering the channel pressures.



*Figure 3.8: 3D intertwining channel device produced using Black V4 resin. Imprint measured 16 mm x 16 mm x 35 mm. Lego mini figures are 16 mm wide at the feet and 40 mm tall.*

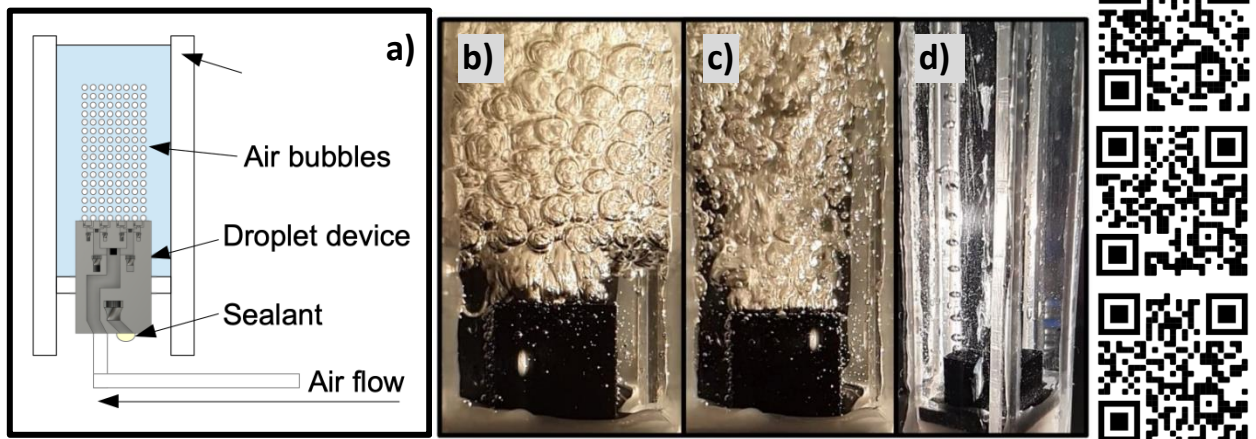


Figure 3.9: Air in water experiment. a) Schematic of the experiment b) Air bubble regime when air is flowed at 1 kPa: <https://youtu.be/iAmIEawa1us>, c) Air bubble regime when air is flowed at 0.1 kPa: <https://youtu.be/Qn493fruWol>, d) Air bubble regime when air is flowed at 0.01 kPa: [https://youtu.be/QkRU\\_YR\\_Jzq](https://youtu.be/QkRU_YR_Jzq). As the pressure decreases, the air flow decreases as does the turbulence within the chamber. At 0.01 kPa, the pressure is so low that the most favourable channel is the only one to observe flow.

Initial oil in water droplet experiments was performed and no regular droplet generation was observed as the oil was pinned to the surface of the device, Figure 3.10. Generated droplets did not have enough buoyancy to detach but would instead be pinned on the surface and grow from the additional droplets from the intersection until the droplet was large enough to come into contact with a neighbouring outlet and coalesce. This formed a disruptive layer and covered several channels with oil. These channels then became dominated by the oil flow and the water flow would circumvent to a water favoured channel. Droplets generation was too varied and inconsistent to accurately report. Both transparent and black resin was used to fabricate the device but no difference in surface pinning was observed.

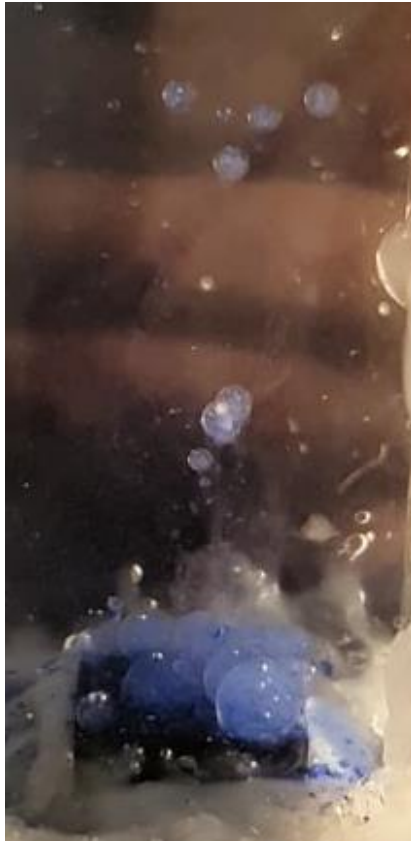


Figure 3.10: Oil in water droplet generation using 64 outlet device. Initial oil in water experiment was halted after oil was pinning to the surface and coalescing to form an oil layer that disrupted droplet generation. Video showing the formation of this oil layer and significantly varied droplets generated: <https://youtu.be/koouU9QPuqQ>

#### 4.5.3 Singular outlet device with 3D channels

A singular version of the branching system was produced with a modified body. Here, water in oil droplets were observed, Figure 3.11 and 3.12, to be  $311 \pm 16 \mu\text{m}$  in size when  $Q_{\text{oil}}$  equals 0.15 mL/min and  $Q_{\text{water}}$  equals 0.02 mL/min ( $\phi = 0.13$ ), at a rate of  $8 \pm 1$  droplets per second, Figure 3.13. Smaller and more frequent droplets ( $81 \pm 1$  droplets per second) were generated at  $Q_{\text{oil}}$  equals 0.20 mL/min and  $Q_{\text{water}}$  equals 0.02 mL/min ( $\phi = 0.1$ ), but this was by inconsistent droplet generation and suffered from tip streaming and co-flow. Therefore, a functioning 64 outlet droplet generator should be able to produce 512 droplets per second with  $Q_{\text{oil}}$  of 9.6 mL/min and  $Q_{\text{water}}$  of 1.28 mL/min.

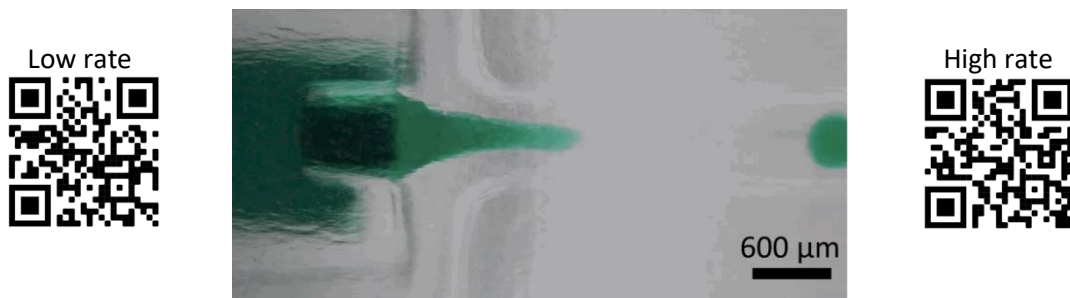


Figure 3.11: Simplified 3D droplet generator intersection. Video of operation at intersection and 4 mm downstream after current view. Flow rates:  $Q_{Oil} = 0.15 \text{ mL/min}$  and  $Q_{Water} = 0.02 \text{ mL/min}$  ( $\phi = 0.13$ ) - <https://youtu.be/pELEMavhRqY>. Higher oil flow rate results in smaller droplets at a higher production rate but more inconsistent generation: <https://youtu.be/5hXxZZp5iX0>.

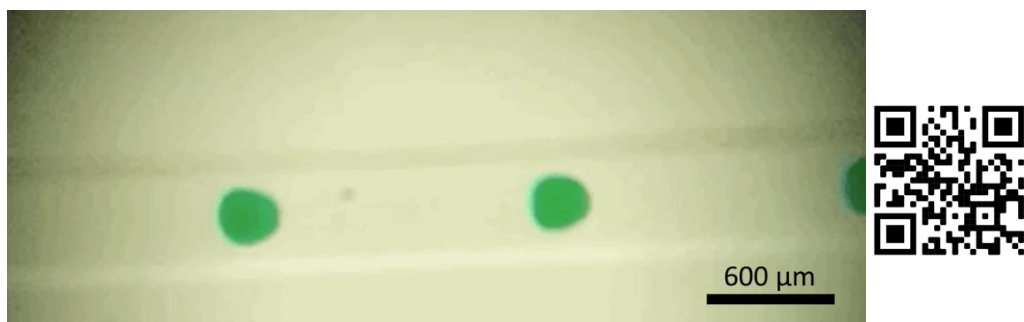


Figure 3.12: Simplified 3D droplet generator – 4 mm downstream. Video of operation at intersection and 4 mm downstream after current view: <https://youtu.be/pELEMavhRqY>

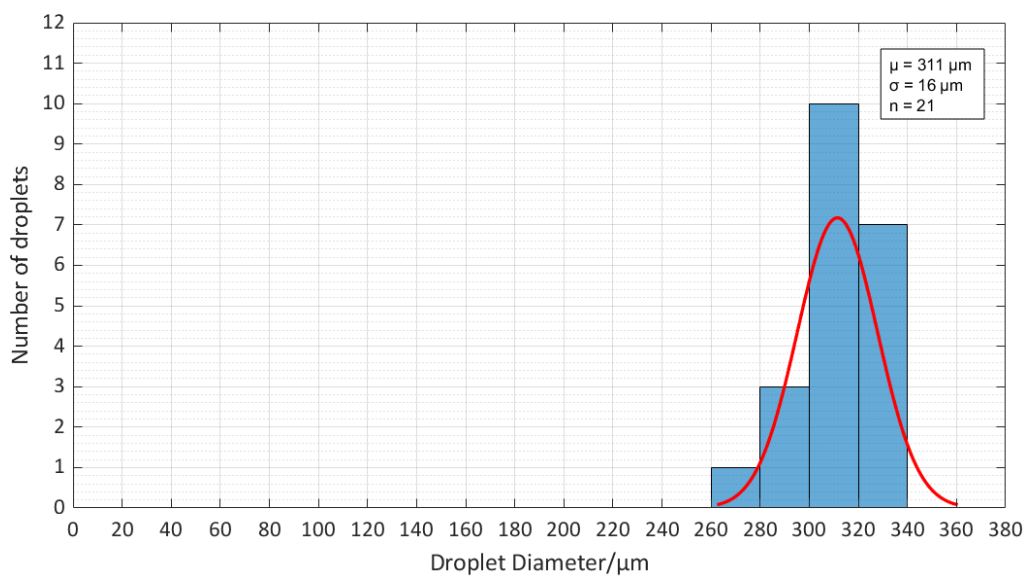


Figure 3.13: Size distribution of droplets produced in the 3D printed singular channel device. Flow rates used:  $Q_{Oil} = 0.15 \text{ mL/min}$  and  $Q_{Water} = 0.02 \text{ mL/min}$ . Mean diameter equals  $311 \pm 16 \mu\text{m}$ ,  $n = 21$ .

### 4.6 Discussion

The planar device demonstrated that observations could be made through the transparent material, despite the surface roughness, and that the FormLabs 3 SLA printer could produce a

complete microfluidic device with channels smaller than previously reported for the printer. Additionally, temperature control was observed, but with a lower change in temperature than the PDMS-glass. This is expected as the PDMS-glass device used the glass as a thermal conductor, which is more effective than the polymer device. Additional experimentation could optimise the temperature change as the device has a far higher rupture limit, as it is complete piece and not two bonded parts, which in turn could provide an alternative method for fabricating the devices described in Chapter 2.

Upon optimising conditions for SLA printed devices and experiencing the potential, the 64 cross flow droplet generator was designed and fabricated. Whilst it was possible to produce a device with intertwining channels, immediately utilising such a device resulted in no consistent droplet generation, hence the transition to the simplified device. All this occurred within one week, a prototype turnaround speed that would be impossible via traditional methods.

Not only that; but the actual structure of the 3D channels is impossible with current clean room technologies as well. The only method to replicate such structures would be to stack many etched or micro-milled layers. Twisting channels are also very difficult to produce using milling or lithographic methods but not for the layer-by-layer assembly of additive fabrication. Multilevel woven or branching channels have been demonstrated before, but not in a way where it is both integral for the function of the device nor would the performance be significantly enhanced. Many are stacked 2D structures with the 3D features being simple straight vertical channels to traverse material in between levels. The devices within this chapter feature complicated multileveled features where branching occurs on 8 distinct levels and recombination of the flows occurs on a different level.

Three different droplet generating devices were 3D printed using an SLA printer. Whilst the bulk dimensions of the devices were accurate to the designs, all devices' channels were smaller than designed. Holes are difficult to print with SLA printers due to the reflection and refraction of the laser and the drainage of resin out of the device as it prints. Additionally, commercial SLA printers use slicers that over cure hanging structures. This results in free resin within the channel to be crosslinked. Channel roughness is smoother and squarer than those produced using filament printers, e.g., the droplet devices in Chapter 2. These devices produced droplets that were significantly larger than those described in Chapter 2; however, these are also using larger channels so that is expected. It is fair to assume that a more optimised slicer and printer could produce smaller more refined structures that could become more comparable to traditional microfluidic systems. It is interesting how both the planar and 3D device observed droplet generation with a flow rate ratio near 0.1, as did the devices from Chapter 2, which is supported by the scaling theory. Therefore, the same structure scaled down could also implement same flow rate ratio to produce initial droplets for assessment and further optimisations from there on.

Preliminary experimentation with the 64-droplet generator did not provide a consistent droplet generation, due to three major factors: a lack of shearing forces; resin affinity to the oil discontinuous phase and a lack of equal flow pressure within the device due to under pumping. Lack of shear forces is assumed to occur at the droplet generating intersection. This lack of a shear forces would result in either a co-flow or oil dominant flow into the outlet channel; resulting in the oil to remain attached to the resin surface. This would be typically resolved by optimising the

flow rate ratio, but this was exceedingly difficult or impossible to observe in the transparent device, as the working distance for observation was too great within the chamber setup. Oil to polymer affinity becomes a more apparent problem at the outlet-to-chamber interface. There is no active shearing force to instigate droplet generation here other than the buoyancy of the droplet. As observed by the oil spreading on the surface, the buoyancy of the droplet was not greater than spreading forces upon the polymer surface. This would typically be overcome by surface treatments, typically surfactants, to generate a hydrophilic surface thus repelling the oil phase. This would aid both the droplet generation at the intersection and at the outlet-to-chamber interface. Finally, not being able to clearly observe into the device to understand the internal flows resulted in flow rates being used which were not suitable for the device (10+ mL/min). Poor optimisation resulted in water or oil channel bias, resulting in inconsistent flows or the fouling of channels rendering the device defective until cleaned.

One additional effect observed was the effect of gravity on the 64-droplet generator. If the device was mounted horizontally into a chamber, then the channels at the top would be oil dominant. A combination of gravity and the system being under too little pressure means that the pressure does not equilibrate; hence, neither does the droplet generation. Therefore, all the reported experimentation with the 64-droplet generator is vertical, whilst the planar device and 3D single focus flow generators are operated horizontally. It is expected that a reduction in the characteristic length of the capillaries would result in a reduction in the Bond number; therefore, the capillary forces become more dominant. Therefore, future iterations of the 64-droplet generator should feature outlet channels similar in length to the singular 3D design.

Industrial applications of microfluidics are limited in use, due to the start-up costs and lack of multiplexing present. The conceptual microfluidic structure could provide a framework to develop new novel structures to multiplex a common process such as droplet generation. In accordance to scaling laws of microfluidics and the splitting ratio, equations 1-5, it is theorised that a continuous droplet generator with non-microfluidic inlets could be functional, as long as number of branching generations, branches volume ratio and the correct flow rate ratios were implemented. Such devices could then be operated in parallel to one another, allowing for industrial scale microfluidics that has been previously unachievable due to current fabrication techniques.

One clear advantage of the intertwining structure is the channel density compared to planar devices. Parallel droplet generation devices are heavily reliant on the surface area of the plane on which the intersections are present. This means that greater parallelisation requires an additional increase in the surface area of the device, leading to a dramatic increase in the devices' footprint. Meanwhile, the 3D droplet generators reduce the area required by allowing intertwining to occur. Addition of splitting generations with smaller channel diameters would increase the devices' footprint, but far less than if the device was a stacked 2D structure.

*Chapter 4 – Three-dimensional bioinspired intertwining channel multiplexed droplet generator.*

## 4.7 Conclusions

In conclusion, 3D microfluidics is a promising field which will benefit from advances in additive manufacturing. Truly 3D structures can now be fabricated as one whole piece, as opposed to either stacked or intersecting 2D structures. Here a simple 2D planar device is produced using a commercial SLA printer mimicking the droplet generation device fabricated in Chapter 2 to

confirm that the materials would be compatible. Channel dimensions were  $700 \pm 10 \times 700 \pm 10 \mu\text{m}$ . Planar devices produced water in oil droplets sized  $371 \pm 25 \mu\text{m}$  ( $n = 100$ ) at a  $Q_{\text{oil}}$  of 1.5 mL/min and  $Q_{\text{Water}}$  of 0.2 mL/min, flow ratio equals 0.13.  $16 \pm 1$  droplets were produced per second. Temperatures of 31 °C and 17 °C were achieved within the integrated heating and cooling channels. A 3D cross-flow droplet generator featuring branching and intertwining channels resulting in 64 intersections was fabricated. The device imprint was 16 mm x 16 mm x 35 mm and featured square channels that were  $600 \pm 10 \times 600 \pm 10 \mu\text{m}$ . Compressed air was flowed through the device to confirm that all of the outlets were open. Initial oil into water droplets testing was inconclusive due to the hydrophobic surface causing surface pinning and coalescence. A simplified version of the device was fabricated with one focus flow intersection. Water droplets which were  $311 \pm 16 \mu\text{m}$  ( $n = 21$ ) in size, were produced from  $Q_{\text{oil}}$  of 0.15 mL/min and  $Q_{\text{Water}}$  of 0.02 mL/min, flow ratio equals 0.13, produced  $8 \pm 1$  droplets per second. It is predicted that a functioning 64 outlet droplet generator should be able to produce 512 droplets per second with  $Q_{\text{oil}}$  of 9.6 mL/min and  $Q_{\text{Water}}$  of 1.28 mL/min. These devices demonstrate the promise that complicated multiplexed devices featuring intertwining channels that are integral to the function of the device. Structures that are extremely difficult, costly, and labour intensive with current 2D based technologies could be easily and rapidly fabricated using additive manufacturing techniques.

## Chapter 5 – Development of an ultra-high voltage electrophoresis system using a Van de Graaff generator capable of $10^7$ theoretical plates.

### 5.1 Abstract

Electrophoresis is a powerful tool for analytical chemistry and molecular biology. Performance is proportional to the applied voltage. Current high voltage electrophoresis uses limited voltages due to the dielectric breakdown of the fused silica capillary. Developments were made in the experimental work of Lee et. al, in which a Van de Graaff (VdG) generator was implemented for separations of simple molecules. This chapter presents the experimental investigation of VdG based separations and found that a 1-meter-long capillary with an inner bore of 50  $\mu\text{m}$  could produce theoretical plate numbers as high as  $1.73 \pm 0.16 \times 10^6$ . The average voltage was estimated, via a plate number ratio approximation ( $V_N$ ) or peak migration time ( $V_{tm}$ ) ratio approximation and found to be  $296.5 \pm 0.17$  kV or  $82 \pm 8$  kV, respectively. This discrepancy is assumed to be due to non-ideal conditions resulting in non-linear or aperiodic electrophoresis to occur. The emitted electric field along the capillary was characterised to be non-linear, as was the migration time. An alternative estimation, based upon the non-linear migration of samples under sub-30 kV conditions ( $V_{est}$ ), was found to be 192 kV. A new injection procedure was determined to increase the performance of VdG generator separations, increasing the theoretical plate numbers up to  $7.45 \times 10^7$ , exceeding the current performance of other ultra-high voltage electrophoresis experiments. The applied voltage is estimated to range between 192.0 -  $296.5 \pm 0.17$  kV based on non-linear migration and plate number observations. The potential for record breaking plate numbers in an inherently safer and cheaper experiment warrants further investigations into alternative electric field generators for ultra-high resolution electrophoretic separations.

### 5.2 Introduction

Capillary electrophoresis is an incredibly well documented field of research with years of extensive work providing a solid foundation for future developments. Since the initial observations of peptide movement under an electric field by Tiselius from 1937<sup>173-176</sup>, research has constantly been focused on improving the resolution so that previously indistinguishable samples may be separated. Additionally, other developments such as separation matrix gels, injection methods and coupling to additional analytical techniques have been made.<sup>177-184</sup>

Electrophoresis can be defined as an analytical technique used to study charged particles or ions and their migration due to an applied electric field between a cathode and anode.<sup>185</sup> At first, this was performed and developed in larger tubes in the shape of U-bends, but the concept was developed and expanded upon over the coming years.<sup>186,187</sup> However, the conventional high performance capillary electrophoresis conditions were first defined by Lukacs and Jorgenson et al.<sup>188-190</sup> Many of the included conditions are still used in modern commercial units, for example using a maximum voltage of 30 kV. But once again developments were made by increasing the voltage to 120 kV<sup>191</sup>, and these were improved upon again by producing voltages exceeding 300 kV and applying this to a fused silica capillary with an inner bore of 75 - 50  $\mu\text{m}$ .<sup>192</sup> Separations with

theoretical plate numbers up to  $10^7$  were achieved, thus setting the bar for future experimental separations.

### 5.3 Theory

Previous work by Hjertén et. al.<sup>186</sup> and Jorgenson et. al.<sup>190,193</sup> derived Eq. 5.1-5 by combining the Einstein-Nernst relationship, which relates diffusion coefficients and ionic mobility, with Giddings findings on theoretical plate number and column efficiency.<sup>194</sup>

$$v_{ep} = \mu_{ep}E \quad \& \quad v_{eo} = \mu_{eo}E \quad (\text{Eq. 5.1})$$

$$\therefore \mu_{obs} = \mu_{ep} + \mu_{eo} \quad \therefore v_{obs} = \mu_{obs}E \quad (\text{Eq. 5.2})$$

$$t_m = \frac{L}{v_{ep}} = \frac{L^2}{\mu_{obs}V} \quad (\text{Eq. 5.3})$$

$$\sigma_L^2 = 2Dt_m = \frac{2DL^2}{V\mu_{obs}} \quad (\text{Eq. 5.4})$$

$$N = \frac{L^2}{\sigma_L^2} = \frac{V\mu}{2D} = 5.54 \times \left(\frac{t_m}{w_{0.5}}\right)^2 \equiv 16 \times \left(\frac{t_m}{w_{base}}\right)^2 \quad (\text{Eq. 5.5})$$

In Eq. 5.1, the electrophoretic and electroosmotic velocity in  $\text{m}^2\text{s}^{-1}$ ,  $v_{ep}$  &  $v_{eo}$  respectively, is defined by the analyte electrophoretic and electroosmotic mobility,  $\mu_{ep}$  &  $\mu_{eo}$ , in  $\text{m}^2\text{V}^{-1}\text{s}^{-1}$ , and the applied electric field,  $E$ , in  $\text{V m}^{-1}$ . The observed mobility ( $\mu_{obs}$ ) hence the observed velocity ( $v_{obs}$ ) is a determined by the sum of the two different mobility, as shown in Eq. 5.2. The time of migration,  $t_m$ , is a function of the capillary of length,  $L$ , in meters; applied voltage,  $V$ , in V, and  $v_{obs}$ , as per Eq. 5.3.  $\sigma_L^2$  gives the spatial variance, in  $\text{m}^2$ , in terms of the molecular diffusion coefficient of the analyte ( $D$ ) in  $\text{m}^2\text{s}^{-1}$  multiplied by  $t_m$ . Alternatively,  $D$ ,  $L$ ,  $V$  and  $\mu_{obs}$  can be used to determine  $\sigma_L^2$  (Eq. 5.4). When combined with the Giddings theoretical plate number equation;  $L$ ,  $V$ ,  $\mu$  and  $D$  can be used to express the theoretical plate number, Eq. 5.5. Therefore, if  $\mu$  and  $D$  are kept constant, it is then the voltage applied to a given system that determines the theoretical plate number,  $N$ . Thus, an increase in  $V$  leads to an increase in  $N$ . It is also possible to assess an electropherogram to determine  $N$ , using the migration time of a peak,  $t_m$ , with the peak width at half height,  $w_{0.5}$ , or the base peak width,  $w_{base}$  as per Eq. 5.5. Because of this key calculation, there was a shift in direction that strived to discover how to apply a larger voltage to a system to provide a higher resolution separation.

It is possible to use time instead of distance as a measure of the observed diffusion. This is because the observed diffusion relies upon mobility and diffusion coefficient, both of which are also time dependent. In accordance to the theory, the longer the separation capillary, the greater time for the peak to resolve and the greater the diffusion observed.

Eq. 5.5 is a simplified approach to calculating the plate number that relies upon several assumptions, such as diffusion being the only observed peak broadening effect as it is significantly larger than the other effects hence; there is no joule heating; there is no conductivity difference between the analyte and the buffer solution; the resolved peaks are symmetrical; there is no adsorption onto the capillary surface; convection is minimalised due to the narrow bore diameter

of the capillary; and finally that the pH of the sample injected is no different than the separation buffer.

$$N = \frac{L}{\frac{\Delta\chi_0^2}{16} + \frac{2DL}{uE} + \frac{1}{12} \left(\frac{BkL}{\lambda}\right)^2 \left(\frac{RE}{2T_0}\right)^4 + ALE} \quad (\text{Eq. 5.6})$$

Hjertén et. al. provided Eq. 5.6 which additionally accounts for the band broadening caused by; the original injection width,  $\Delta\chi_0^2$  in m; joule heating,  $\left(\frac{BkL}{\lambda}\right)^2 \left(\frac{RE}{2T_0}\right)^4$  where;  $B$  is a constant equal to 2400 K;  $k$  is the electrical conductivity in  $\Omega^{-1} \text{ m}^{-1}$ ;  $\lambda$  is the thermal conductivity of the buffer in  $\text{J s}^{-1} \text{ m}^{-1}$ ;  $R$  is the radius of the capillary in m;  $T_0$  is the temperature of the coolant in K (in this case room temperature dry air) and the adsorption constant,  $A$ , of a given solute in  $\text{M}^{-1} \text{ s}^{-1}$ .<sup>195</sup> Hjertén also proposed that a given system has an optimum field strength,  $E_{opt}$ , where  $E$  leads to the greatest reduction in the observed effects of the diffusion without the effects of joule heating and adsorption being significantly increased. After the  $E_{opt}$ , these two factors, the joule heating in particular, results in a decrease in the performance of the system. The following equations, Eq. 5.7 to 5.10, are essential for understanding these observed electronic effects:

$$R = \rho LA \quad (\text{Eq. 5.7})$$

$$V = IR \quad (\text{Eq. 5.8})$$

$$E = \frac{V}{L} \quad (\text{Eq. 5.9})$$

$$P = I^2 R = \frac{V^2}{R} = VI \quad (\text{Eq. 5.10})$$

where, current ( $I$ ) in Amp; resistance ( $R$ ) in  $\Omega$ ; conductivity ( $\rho$ ) in  $\text{S m}^{-1}$  and power ( $P$ ) in Watt. Joule heating in electrophoresis is the by-product of excess power in a system. Any increase in heat leads to a change in the buffer viscosity, zeta potential, diffusion, catastrophic bubble formation and several other observable effects.<sup>196,197</sup> Typically, electrophoresis systems implement a narrow and long capillary bores to increase the resistance,  $R$  as per Eq. 5.7, allowing for high voltages whilst simultaneously reduced currents are implemented, Eq. 5.8, and in turn greater electric fields, Eq. 5.9. The electric field is often considered as liner in electrophoresis with voltages below 30 kV<sup>198</sup>, as simply defined in Eq. 5.9. Increasing the current increases the voltage, thus the electric field strength and plate number, but also leads to an increase in the  $P$  generated, Eq. 5.10. Typically, ultra-high voltage electrophoresis experiments seek to increase the  $N$  by increasing the  $V$  via increasing  $I$ . But an increase in  $I$  leads to a squared increase in the power generated, and the joule heating upon a system. To mitigate this effect, additional experimental conditions are implemented, such as air cooling or submersion in oil, to aid in removing the excess heat.

A VdG generator is of particular interest because it is distinctly different from the typically implemented power supplies, as it is a current generator capable of producing ultra-high voltages. The current is generated as the belt spins and a charge builds up on the dome. Therefore, the current is limited by the speed of the belt and never exceeds 10  $\mu\text{A}$ . Coupled with the relatively high resistance of the buffer filled capillary acting as a wire, it is possible to easily produce a voltage

of 300 kV on a bench top with a very safe current. The low current also aids in dealing with the problem of disruptive Joule heating.

$$V_{tm} = \frac{t_m(30\text{ kV})}{t_m(\text{VdG})} \times 30\text{ kV} \quad (\text{Eq. 5.11})$$

$$V_N = \frac{N_{\text{VdG}}}{N_{30\text{kV}}} \times 30\text{ kV} \quad (\text{Eq. 5.12})$$

Under ideal theoretical conditions, the VdG generator can produce a voltage of 300 kV therefore should have a plate number ten times greater than a typical 30 kV power supply. Due to the low current discharge nature of the VdG generator, it is easier to calculate the applied voltage from collected data. Under ideal linear conditions, dividing either the  $t_m$  of a specific peak or  $N$  of the 30 kV by the respective VdG generator produced value, followed by a multiplication of 30 kV, allows for the actual applied voltage ( $V_{tm}$  or  $V_N$ ) from the VdG generator to be determined (Eq. 5.11 & 5.12). It is essential to know the applied VdG generator voltage as this indicates the efficiency of the system and aids in identifying an error in the system or evaluating optimisations. Ideally, both estimations should produce the same applied voltage and deviations would indicate non-ideal electrophoresis is occurring.

With this theory in mind, an alternate method to implement a VdG generator to apply a voltage of 300 kV for capillary electrophoresis experiments is investigated and discussed. The system was optimised and the resolution compared to a 30 kV power supply. Previous work has been performed into the field, by Lee et al.<sup>199</sup>, which showed very promising results ( $N$  up to  $3.48 \times 10^6$  plates) and will be developed upon further.

## 5.4 Experimental

### 5.4.1 Chemicals and materials

All listed chemicals were purchased from Sigma-Aldrich. A stock of 10 mM borate buffer was prepared by the dissolution of 0.9534 g of sodium tetraborate decahydrate in 250 mL of Milli-q water. The pH of which was equal to 9.24. 2 mM solutions were prepared by dilution for further experiments. This will be simply referred to as the borate buffer. A cleaning solution of 0.5 M sodium hydroxide was also prepared. 100  $\mu\text{M}$  fluorescein isothiocyanate (FITC) was prepared by dissolving 0.0038 g of FITC in 100 mL of borate buffer. This would later be used for amino acid staining. A mixture of 100  $\mu\text{M}$  FITC and 200  $\mu\text{M}$  of fluorescein (F) solution was prepared by dissolving 0.0038 and 0.0066 g, respectively, in 100 mL of borate buffer. The FITC and F solution acts as a simple separation sample, as the molecules will show the same charges at the pH but differ in molecular mass. 2 mM solutions of Valine (Val), Alanine (Ala) and Glycine (Gly) peptide solutions were prepared. All solutions were sonicated for at least 5 minutes followed by filtering using Millipore Express® PLUS Membrane filter (PES) - 0.22  $\mu\text{m}$  filters, Merck, Germany. The solutions were then degassed by rapid stirring under a vacuum. 1.5 mL stained amino acid solutions were prepared with using the stock solutions in a ratio of 1:5:3:2 of FITC:Gly:Val:Ala and left overnight at 4 °C to allow for peptide staining. 3D printed components were printed using polylactic acid (PLA) filament, 1.75 mm diameter, Raise3D, USA. 5.4.2

### 5.4.2 Electronics

The conventional high voltage power supply was a CZE 2000, Spellman, USA. The power supply used the provided outlet cable made of UL listed high voltage wire to dip into the sample during separations, with the buffer reservoir connected to ground. The VdG generator was an N-100v, Winsco, USA. No modifications were made to the dome or chassis. A platinum electrode was connected to a steel tumbler containing the first buffer reservoir. The VdG generator then passes the charge to the tumbler by the electrode which was placed 1 mm from the dome's surface. The VdG generator setup was grounded through the CZE 2000. Injections were performed using the 30 kV power supply. Initial injection times and voltages were 10 seconds at 30 kV but then reduced to 1 second and 5 kV to reduce plug width, hence improve plate number. Amp meters were implemented by measuring the voltage across a 100 kΩ resistor in two locations: firstly, at the sample side of the capillary and secondly from the VdG generator outlet. These were also fitted with a 1 μF capacitor to reduce noise by limiting the measurement bandwidth to 10 Hz.

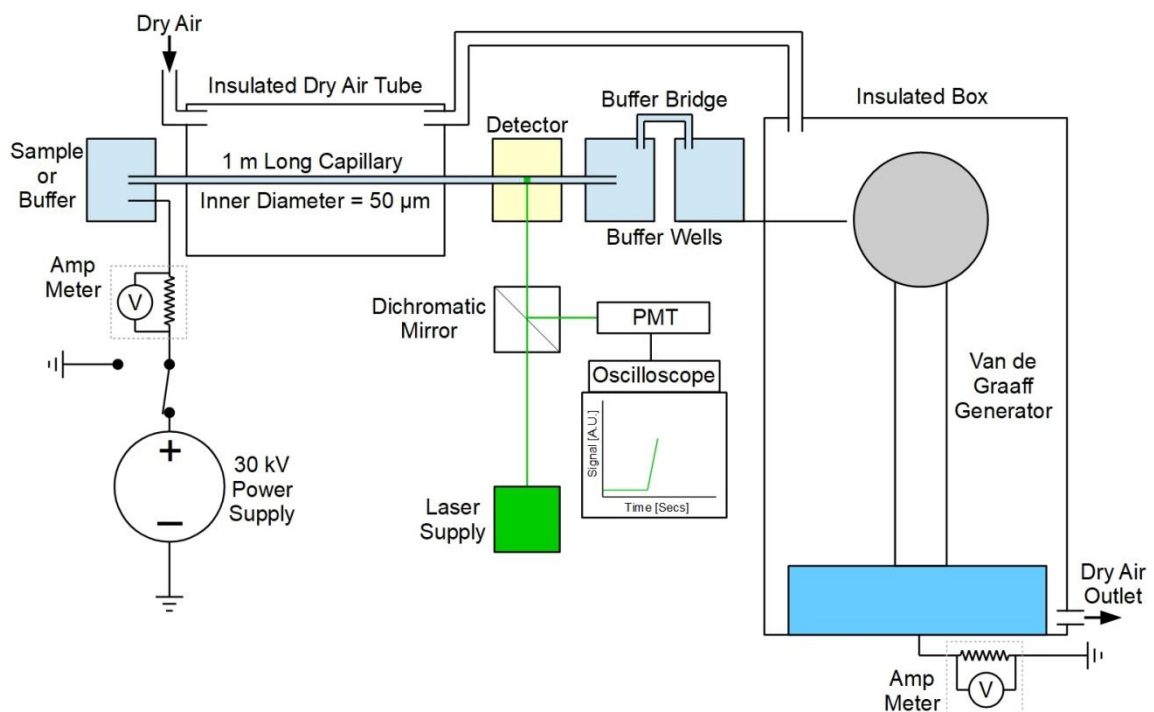


Figure 4.1: Schematic of the experimental setup. Power supply is used for all injections and 30 kV separations. The switch next to the power supply is currently resting in the injection step. It would be switched prior to a VdG separation. A photon multiplier tube (PMT) is situated between the mirror and oscilloscope. The voltage was measured across a resistor, active Chapter 5: Development of an ultra-high voltage electrophoresis system using a Van de Graaff generator capable of  $10^7$  theoretical plates.

### 5.4.3 Capillary

1 meter of fused silica capillary with an outer diameter of 360 μm and an inner bore of 50 μm or 25 μm (Postnova, Germany) was prepared by removing 0.5 cm of coating at 17 cm from one end. The coating was removed by burning with a cigarette lighter and cleaning with ethanol. This end of the capillary was then carefully loaded into the detection stage to avoid cracking. The capillary was then cleaned with 1.5 mL of 0.5 M sodium hydroxide, Milli-q water, methanol and then Milli-q water, to ensure a consistent surface within the channel. The capillary was then filled with 100 μM FITC and aligned. The capillary was then cleaned again and filled with buffer. Once completed, the capillary was then placed into the sample holster, holding the capillary flat, and ready for use.

After each run, the capillary was flushed with buffer to avoid buffer fatigue. Upon the occurrence of promising results, the experiment was repeated with smaller bore capillaries.

#### 5.4.4 Detection

The detection method was identical to the method described in the work performed by Lee et al., where the objective in the detector was an EC Epiplan Neofluar 100x Objective, Zeiss, Germany. The following components were purchased from ThorLabs, USA. The detection stage was created using modified optic staging. The staging differed from aforementioned setup so that the capillary would be held horizontally instead of vertically. The excitation laser of wavelength 488 nm with a power of 19.30 mW was generated from a S3FC488 - Fabry-Perot bench top laser source. The excitation light then passes through a F220FC-A 488 to 512 nm collimator, along a 4-meter FT2000EMT fibre optic cable to the exposed capillary. The emitted light was then processed by PMT coupled with a Tektronix DPO 3014 oscilloscope.

#### 5.4.5 3D Printer, materials and settings

3D printed elements were drawn using the computer aided design software Autodesk Fusion 360, Autodesk, USA. These were exported as .STL files and sliced into GCode using ideaMaker, Raise3D, USA. The GCode was then printed using a fused filament 3D printer, a Raise3D E2, Raise3D, USA. All components were fabricated using a 0.4 mm nozzle. The print speed was 500 mm/s, layer height was equal to 0.2 mm, print temperature of 200 °C and a bed temperature equal to 60 °C.

### 5.5 Results

#### 5.5.1 Implementation of 3D printed parts and dry air system

Improvements were made to the experimental setup, according to Figure 4.1, from the prior experimentation of Lee et. al.<sup>199</sup> Prior experimentation observed the movement of the capillary under an electric field as well as surrounding metal objects gathering a charge, which would require discharging in between runs. Figure 4.2 shows the improved setup, which removed most of the metal from the surrounding environment (shown in Support Figure 4.1); thus, the setup was safe to be near during operation and only the VdG generator required discharging in between sample injections.

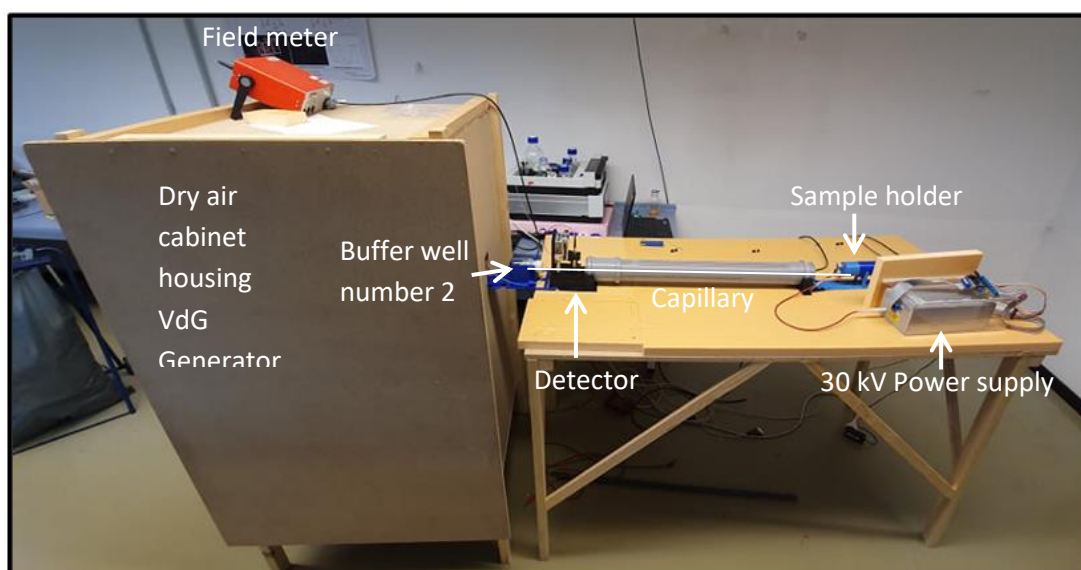


Figure 4.2: Overview of the final Van de Graaff generator electrophoresis setup. On the left is the insulated cabinet housing the VdG generator. The “detector”, two-amp meters and field meter are all connected to the same oscilloscope, allowing for the simultaneous recording of each during operation. Blue and black components within the setup are 3D printed. Additional images are presented in Support Figure 4.2 and 4.4.

Implementation of the dry air system would remove humidity in the air; control the temperature; remove dust; and remove surface water from the internal components. Removing water allowed for consistent experimental conditions for the VdG generator regardless of the humidity of the room, as the discharge is affected by the humidity. The setup is mostly fabricated from wood with polystyrene foam to act as an insulating material. The grey pipe is the insulated dry air tube insulated with foam. Foam is also placed between the power supply and resistor/amp meter to avoid discharge and noise. The meter long capillary is inserted through the dry air tube and held in place at both ends to eliminate any bending before and during the experiment.

3D printed components were designed and fabricated as described, using polylactic acid filament with Support Figure 4.2-4.4 showing these components in greater detail. This polymer is an insulating material, so posed no hazard in the setup. Additionally, all 3D components were designed and fabricated from a singular individual, proving the accessibility of the technology. Typically, fabrication of original laboratory requires the effort of several individuals, whereas one scientist equipped with the correct skills, software and a 3D printer can rapidly produce a required component at their convenience. More sophisticated elements, such as the sample holder shown in Support Figure 4.2 and 4.3a, improved the stability of the capillary and the setup and allowed for faster and more controlled capillary to electrode distance, hence more consistent injections.

### 5.5.2 Capillary lifetime verification

Figure 4.3 shows how repeated separations were possible on the same capillary with buffer washes in-between runs. The FITC peak was observed at  $273 \pm 8$  seconds and F peak was observed at  $285 \pm 8$  seconds. Over 40 repetitions were performed upon this capillary before any effects of degradation were observed (Not all runs shown). This equates to at least 200 minutes of experimental time, a marked improvement in comparisons to Lee et. al. and Jorgenson et. al. capillary lifetimes.<sup>199,200</sup>

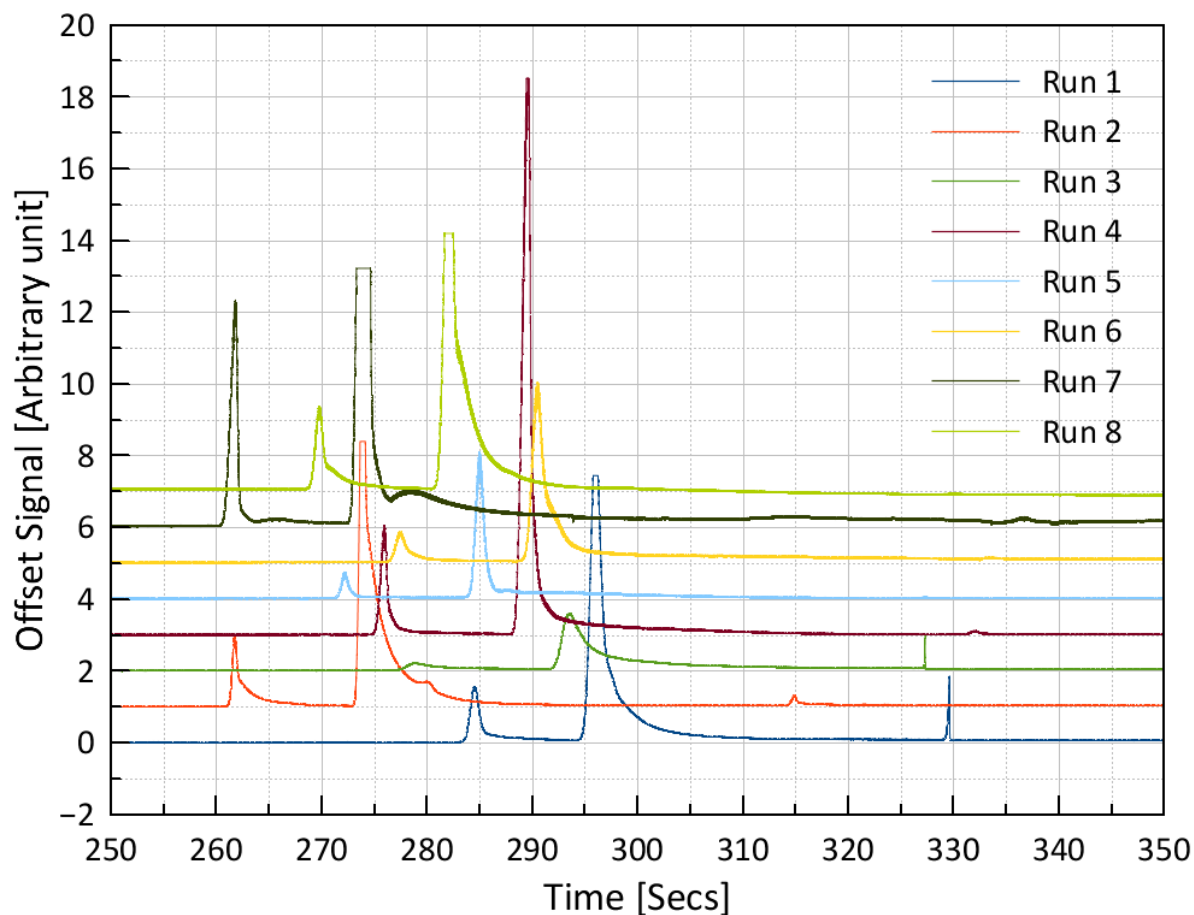


Figure 4.3: 8 consecutive runs of F and FITC separations in a capillary with inner bore of  $50 \mu\text{m}$ . Changes from Lee et. al. setup to current setup allows for one capillary to last for 40+ runs. Here 8 consecutive runs of F and FITC separations are presented. FITC was observed at  $273 \pm 8$  seconds and F was observed at  $285 \pm 8$  seconds.

### 5.5.3 Separations

As shown in Figure 4.4, the VdG generator results in a much faster separation with significantly more narrow peaks. Regardless of the two voltages used, the FITC and F peaks are easily identifiable by the difference in intensity, with FITC being in lower concentration therefore having the lower signal when compared to the F peak and concentration. Using Eq. 5.5, the VdG generator had a total  $N$  equal to  $1.73 \pm 0.16 \times 10^6$ . That is 9.94 times larger than the 30 kV total  $N$  of  $1.74 \pm 0.17 \times 10^5$ . By using the voltage via plate number Eq. 5.11, the maximum voltage was found to be  $296.5 \pm 0.17$  kV. However, this evaluation of performance differs to the time variant of Eq. 5.10, which has a result of  $82 \pm 8$  kV. This discrepancy is not expected and observed from the described ideal systems in the literature; hence, additional effects such as a non-linear electric field or joule heating must be observed.

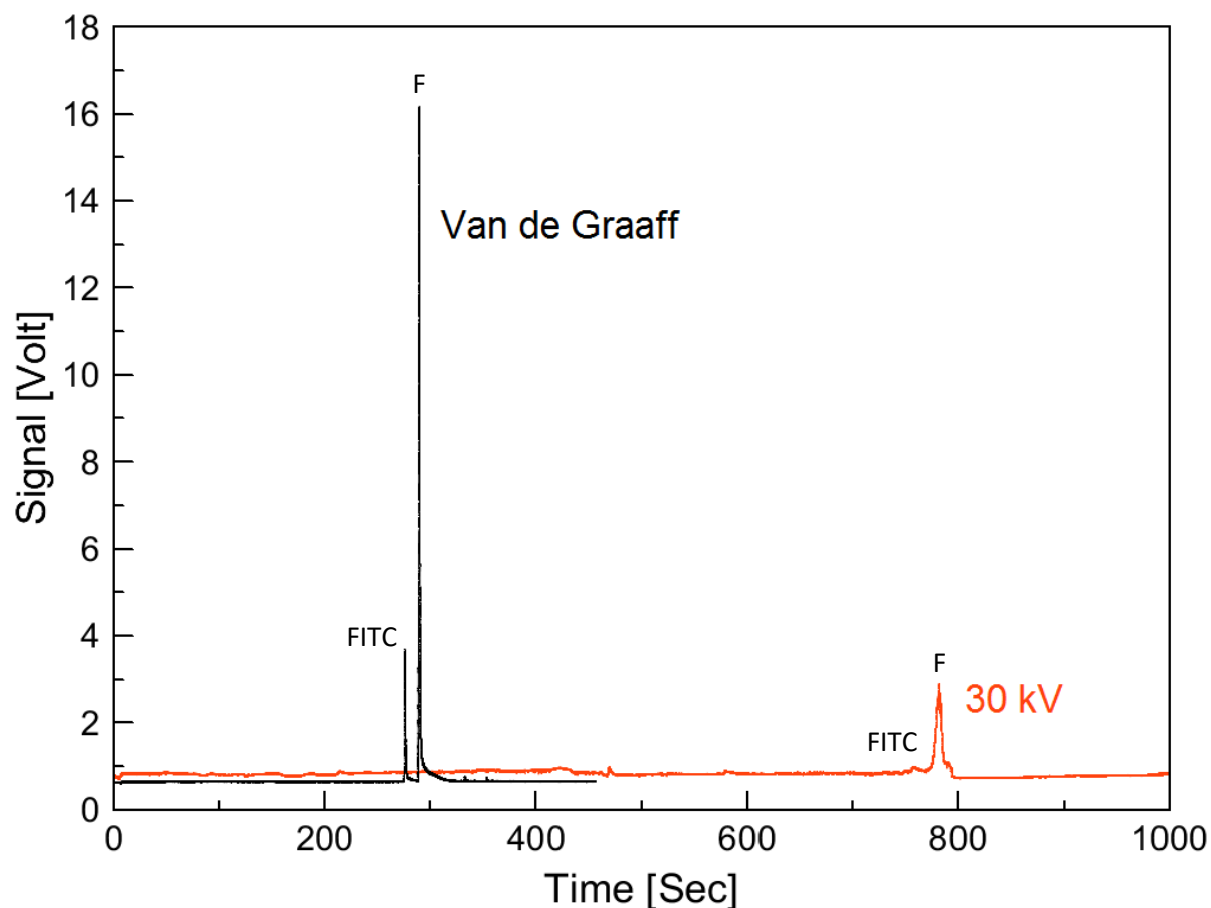


Figure 4.4: FITC and F separation using VdG generator and 30 kV plotted as fluorescence intensity measured as Signal [V] versus Time [Seconds]. Experiment used a capillary with an inner bore of  $50\ \mu\text{m}$ . The FITC peak is the smaller of the two peaks for both voltages due to the lowered concentration, 1:6 ratio with respect to the F concentration. The VdG FITC peak is at 275 seconds, which is 2.76x times faster than with the commercial supply time of 758 seconds, hence a calculated  $V_{\text{tm}}$  of  $82 \pm 8\ \text{kV}$ . The plate number of the FITC peak was  $1.73 \pm 0.17 \times 10^6$  and  $1.75 \pm 0.17 \times 10^5$ , for the VdG generator and 30 kV separations, respectively.  $V_N$  was calculated to be  $296.5 \pm 0.17\ \text{kV}$ .

Simple amino acids were separated, Figure 4.5, where the plate numbers for the VdG generator separation of the Val, Ala and Gly peaks were  $3.79 \times 10^6$ ,  $4.14 \times 10^6$  and  $1.18 \times 10^6$ , respectively. The plate numbers for the 30 kV separations of the Val, Ala and Gly peaks were  $1.84 \times 10^5$ ,  $2.44 \times 10^5$  and  $1.73 \times 10^5$ , respectively. Whilst the VdG generator outperformed the 30 kV, these values for plate numbers and migration times show the same disagreement between the  $V_{\text{tm}}$  and  $V_N$ .

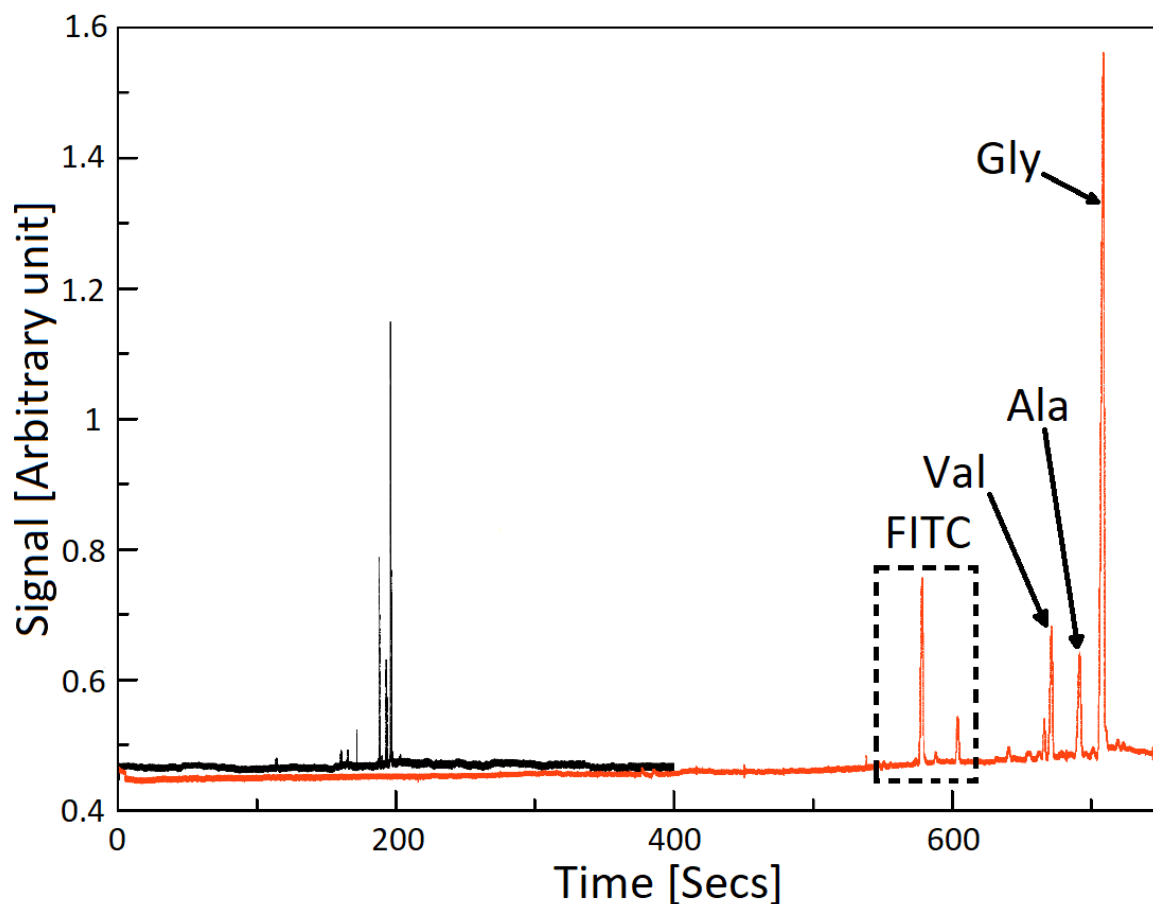


Figure 4.5: Amino acid separation of FITC stained Val, Ala and Gly using a VdG generator vs. 30 kV plotted as fluorescence intensity measured as signal [Arbitrary unit] versus Time [seconds]. Experiment used a capillary with an inner bore of  $25\ \mu\text{m}$ . The concentration ratios of Val:Ala:Gly was 3:2:5. The plate numbers for the VdG generator separation of the Val, Ala and Gly peaks were  $3.79 \times 10^6$ ,  $4.14 \times 10^6$  and  $1.18 \times 10^6$ , respectively. The plate numbers for the 30 kV separations of the Val, Ala and Gly peaks were  $1.84 \times 10^5$ ,  $2.44 \times 10^5$  and  $1.73 \times 10^5$ , respectively.

#### 5.5.4 Characterisation of the electric field and migration times

With higher capillary lifespans, characterisations and optimisations could occur. The electronic field strength emitted from the capillary during experimentation was measured, as seen in Support Figure 4.5, and observed to follow a non-linear inverse relation to the distance from the source. This relationship is also demonstrated in Support Figure 4.6, where a reduction in the capillary length results in a non-linear decrease in the migration time. These both indicate that plug velocity within the capillary is non-linear when using the VdG generator. As such, Eq. 5.11 becomes a less reliable estimate of the experienced voltage of the system as this assumes a linear relationship between the electric field strength and distance. Additionally, shortening the capillary leads to an increase in the current observed, as shown in Support Figure 4.7.

It is impossible to directly measure the voltage of the VdG generator in the current setup. However, armed with the knowledge that migration time is not linear with field strength (and by extension applied voltage), it is possible to extrapolate an estimate from the well-defined 30 kV power supply. As shown by Figure 4.6, voltages between 1 to 30 kV show a similar negative relationship between the voltage and migration time. Extrapolation of this graph to include a calculated migration time of 300 kV, 126 seconds, is shown in Figure 4.6. Plotting the experimental

migration time of an experimental Van de Graaff migration time, 177 seconds, estimates the voltage,  $V_{est}$ , to be 192.0 kV.

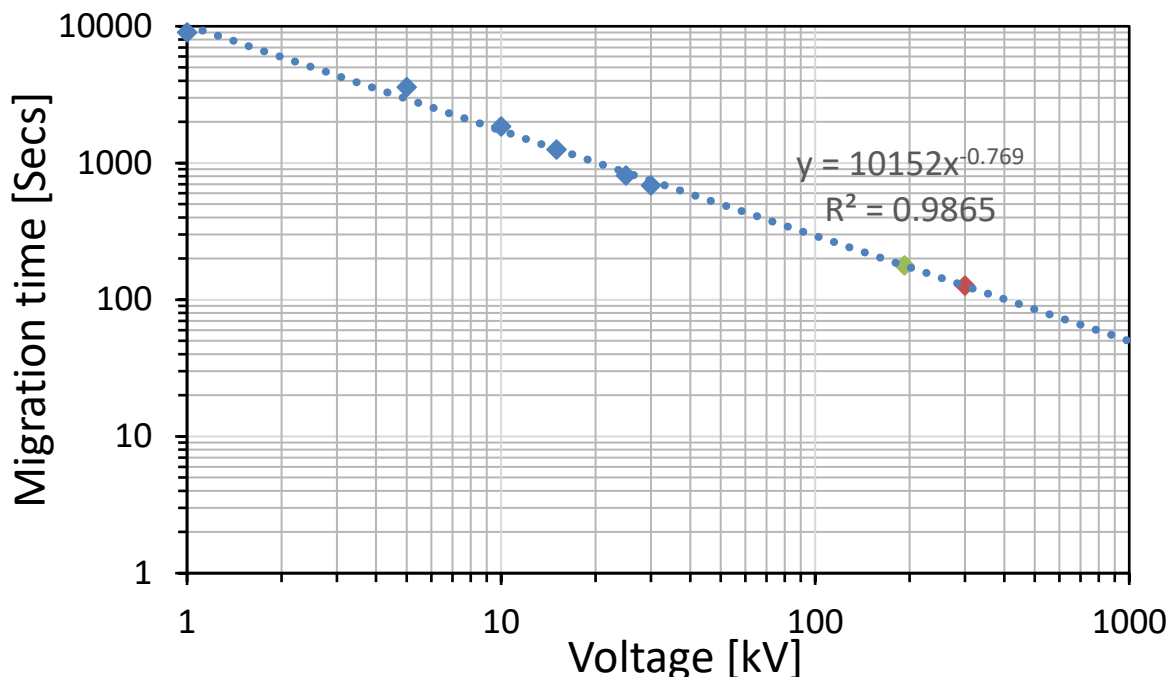


Figure 4.6: Migration time as a function voltage change from the 30 kV power supply. Power supply voltages used were 1, 5, 10, 15, 25 and 30 kV, shown by the blue data points. Experimental VdG generator fluorescein migration time was plotted on the graph, green, and determined the applied voltage to be 192.0 kV. The calculated migration time of an ideal 300 kV system using the extrapolation, red, was calculated to be 126 seconds.

### 5.5.5 Injection optimisation and separation improvement

Hjertén discussed in his work how the width of a peak on a electropherogram relates to the real world width of the separated plug, Eq. 5.5 and 5.6, where if  $N$  and  $t_m$  are known, the width of the plug at detection can be calculated.<sup>195</sup> The smallest the plug can be is at the point of injection, prior to any other peak broadening effects. Therefore, all efforts should be made to inject enough of a sample to be observed, but so much that the initial peak width decreases the performance of the system. Optimisations were made to the injection based on Support Figure 4.8 and 4.9, where reducing the injection time and voltage resulted in an injection smaller plug, which meant a smaller plug was observed at the detector resulting in a higher performance. Figure 4.7 shows the limiting effect that the injection plug's length can have on the plate number. If a 30 kV for 1 second injection pulse is applied, the peak width can never be smaller than 1.46 mm, and hence the separation could never have a performance higher than of  $2.6 \times 10^6$ . It was determined that future experiments would use a 5 kV injection for 1 second, as 1 kV was too unstable in practise. After injection optimisations was made, FITC-stained Ala was separated from FITC with an efficiency of  $7.45 \times 10^7$  theoretical plates, proving that a significant contribution of the performance of the VdG generator-based electrophoresis was being limited by the injection quality.

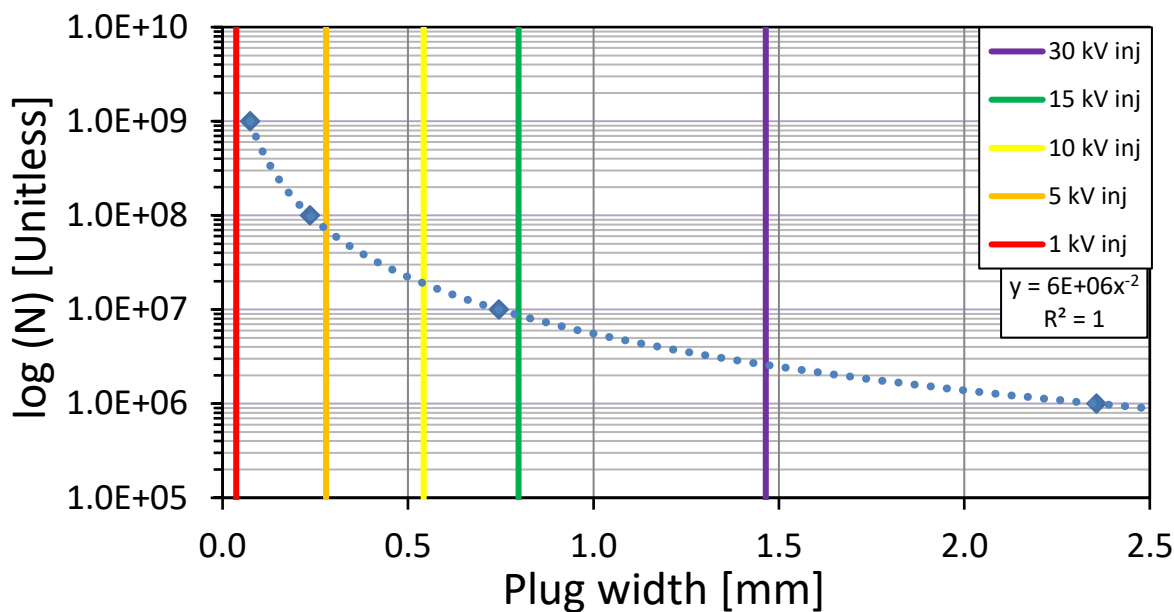


Figure 4.7: The limitations of the injection plug on the resultant plate number for a simulated ideal 300 kV separation. Final plug width cannot be smaller than the injection voltage width. Blue data points and trend line is for simulated peak base width at the point of detection for a separation voltage of 300 kV (based on Figure 4.6). The 5 coloured lines indicate the 1 second injections with 5 different voltages, purple is 30 kV, green is 20 kV, yellow is 15 kV, orange is 5 kV and red is 1 kV.

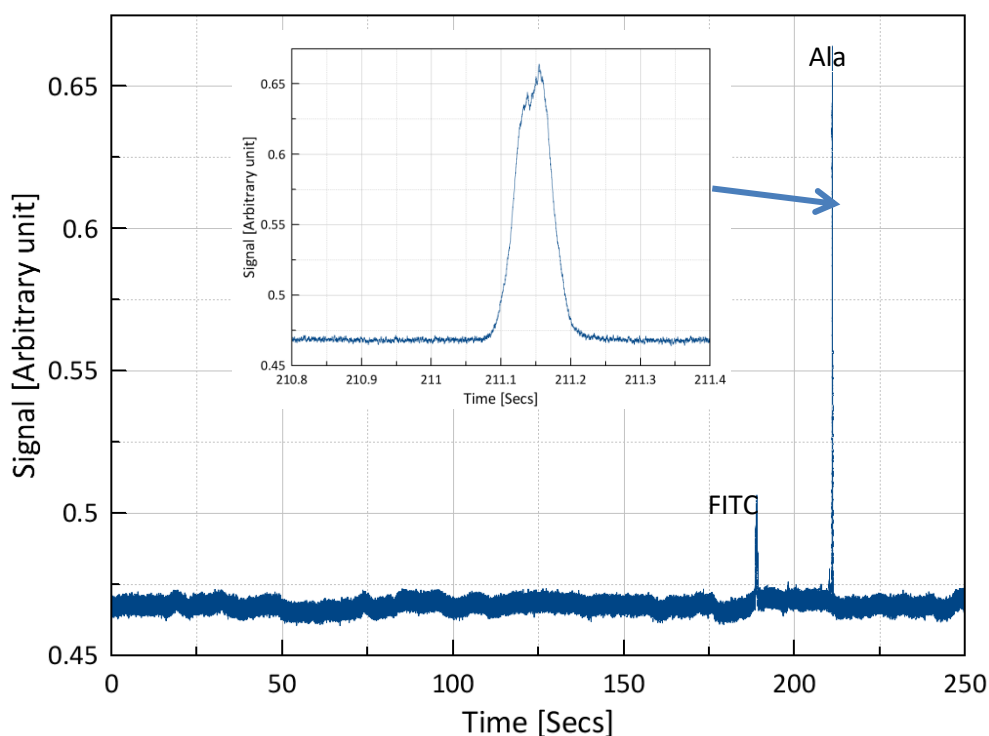


Figure 4.8: Observation of Ala peak with an  $N$  of  $7.45 \times 10^7$ . Experiment used a capillary with an inner bore of  $25 \mu\text{m}$ . Separation of 1mM FITC-stained Ala from  $100 \mu\text{M}$  FITC. Injection conditions were 5 kV for 1 second. Nested) Zoom in of the Ala peak. Migration time is 211.15 seconds.

### 5.5.6 Capillary degradation

Elevated voltages lead to a greater deterioration in the capillary than the standard 30 kV, as shown by the breakdown of the signal in Figure 4.9. The 50  $\mu\text{m}$  bore capillary showed a reduced breakdown rate during experimentation, with a capillary typically lasting over 40 runs with routine washing. Meanwhile reducing the size of the bore to 25  $\mu\text{m}$  increases the resistance allowing for greater electric field strengths within the capillary, hence the faster resolution speed in Figure 4.5 and Figure 4.8. It is assumed that the increase in the difference of electric field strengths between the centre of the capillary and the surrounding air results in a greater rate of dielectric breakdown. Capillaries placed under mechanical stress, such as the one within the Figure 4.10, immediately break under the VdG generator electric field.

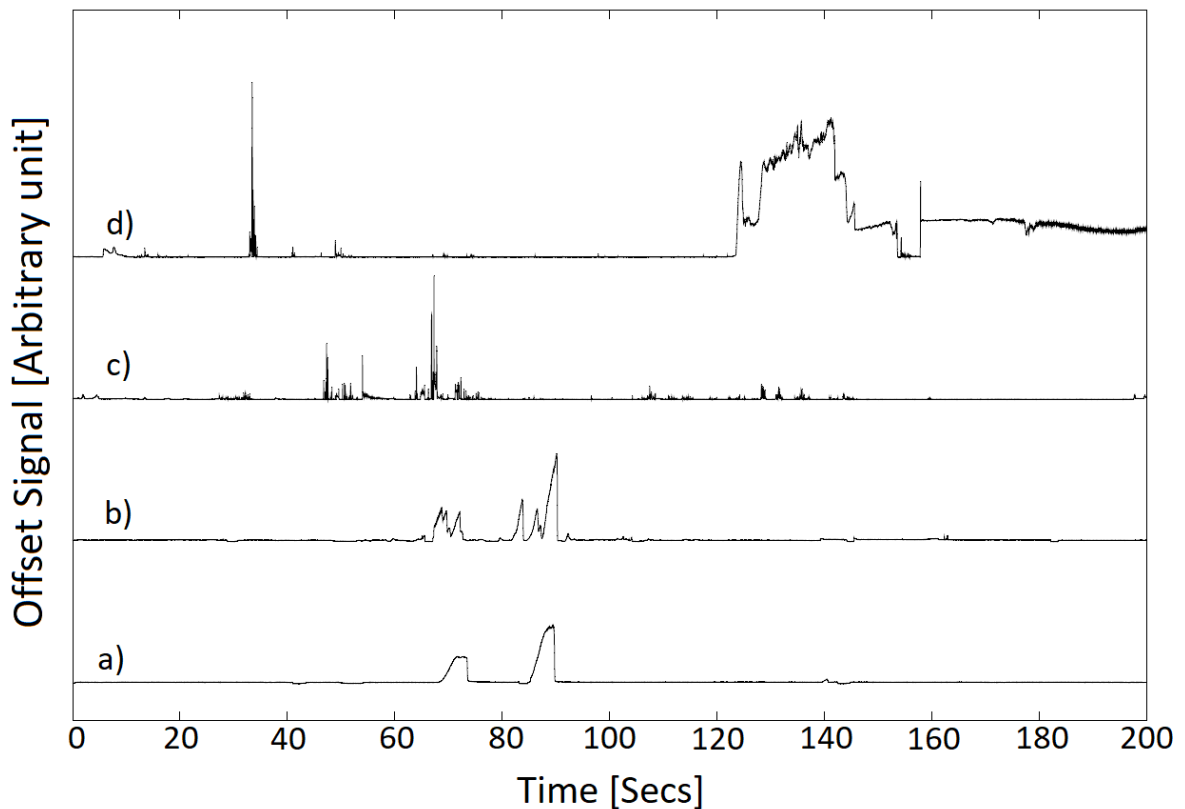


Figure 4.9: The progressive breakdown of a 5  $\mu\text{m}$  capillary shown from the run 1 (a) to run 4 (d). As the runs progress, the peaks breakdown and the background noise increase, additional peaks are apparent and the migration times vary much more. During the final run, the capillary broke into two parts with more crumbling during additional handling. Similar breakdown was observed with the 50  $\mu\text{m}$  capillary but only after 40+ runs with the current setup.

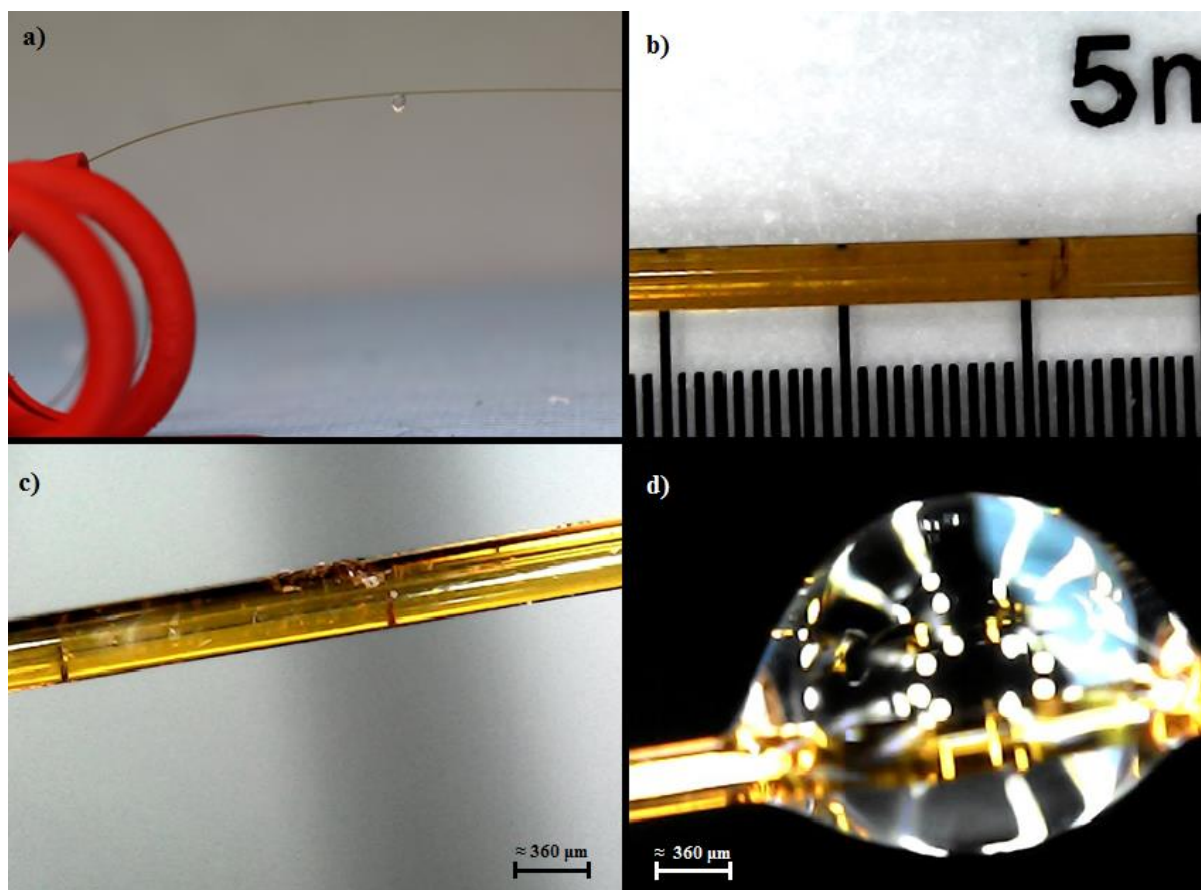


Figure 4.10: Capillary breaking - 50  $\mu\text{m}$  inner bore diameter capillary with cracking caused by the increased voltages. a) A droplet forming whilst the capillary was in a prototyped coil holster. b) and c) Zoomed in images of the capillary at the site where the droplet formed. The large crack across the capillary is visible with additional cracking and surface roughness. d) Zoom in at crack as a droplet forms. All cracks form on the ground side close to the injection point therefore it is fair to assume that the damage is caused by the tunnelling of current across the glass and polyimide wall. This results in the propagation of pre-existing nano- and micro-cracks in the capillary from fabrication and general handling.

## 5.6 Discussion

VdG generator driven separations outperformed all the 30 kV separations in the same conditions, Figure 4.4 and 4.5. The VdG generator applies a stronger electric field than the 30 kV and results in record high efficiencies at much more rapid times than that described in the literature. Interestingly, the order in which the samples pass the detector indicates that species with higher charge densities move slower under the applied electric field of the VdG generator. This indicates that the bulk movement is due to the electroosmotic flow whilst the separations are due to higher charge densities have greater electrophoretic mobility's against the electroosmotic flow, hence a slower observed movement, as per Eq. 5.2. This order of movement differs greatly from typical electrophoretic based experiments and could prove to be a useful tool for separating analytes with low charges which would normally experience slow migration times.

So far, only relatively simple samples have been separated. Whilst allowing for introductory observations of the platform, these amino acids are already well defined, only differing in one methyl group, and are easily separated by other methods. Further experimentation with more sophisticated and complex analytes should be performed to determine the limitations of the system. For instance, glycoproteins and the cleaved glycans can be difficult to separate by typical

electrophoresis or HPLC techniques. Glycoproteins can undergo electrophoresis as the protein can carry a charge. However, once the protein is cleaved from the glycan, the glycan molecules carry no charge. Additionally, some glycans may only show small variations by being stereoisomers. Yet, the isomers have a different shape and volume in solution allowing for the molecules to be distinguished if the separation method has an extremely high resolution. Previous separation efforts have been successful but arduous. Electroosmotic flow driven electrophoresis using a voltage of 300 kV may provide an alternate and simple methodology for these separations. Additionally, electrophoresis is commonly coupled with mass spectroscopy. As such future developments of the setup should also begin to consider how to couple a VdG generator separations resolution with the analytical power of a mass spectrometer. With this in mind, future efforts should consider implementing a coupling between the VdG separation and mass spectrometry.

Determination of the applied voltage and inner capillary electric field strength is still under question. VdG generator output currents were measured and never exceeded 10  $\mu$ A however the resistance of the setup could not be directly measured. Eq. 5.11 and Eq. 5.12 both provide ways to calculate the voltage but experimentally  $V_{tm}$  and  $V_N$  did not significantly overlap. This indicates that the system operates in non-ideal conditions and differs from other experimentation found in literature. Firstly, the VdG generator is a current generator that builds up charge and discharges onto the wire and tumbler of the setup, whilst typical electrophoresis implements direct current (DC) power supplies which supply a constant linear field to the capillary. Current measurements of the setup indicate that there is no significant current drop across the capillary and that the current is constant. It is proposed that either a transformation occurs due to the buffer wells acting as capacitors which provide a constant discharge along the capillary; or that the method to measure the current can only detect a filtered current of 10 Hz and not the actual current discharged through the capillary. Therefore, the observed electrical field within the capillary must differ from the actual field, which could be either non-linear or aperiodic in nature. Due to the voltage being applied as a discharge across air, the migration times may be representative of the total migration time taken as there will be many short pulses of high voltage but then the electric field drops due to discharges in-between the pulses. So, the observed migration time could be an average of these pulses and discharges or transformed direct current.

$V_{tm}$  has been previously implemented in the literature to estimate the applied electric field; however, this relies upon the system fitting ideal conditions and for the electric field to be linear. Therefore, as the field strength increases, then the migration time should increase linearly. But, as demonstrated by Figure 4.6, the current experiment appears to express a non-linear relationship between the field strength and migration time. In the literature, this relation is assumed to be due to joule heating reducing viscosity, resulting in higher velocities. But this is often detrimental to the separation performance, as diffusion is increased, which contradicts the low current and incredibly high performance observed. The current experiment is driven by the electroosmotic flow and adsorption is also possible because the capillary is uncoated, which are additional factors indicating non-ideal conditions. Yet, movement in direction to the detector would not be observed if the electroosmotic movement were suppressed. It is assumed that, due to these non-ideal conditions, the estimation of  $V_N$  ( $296.5 \pm 0.17$  kV) provides a better estimate for the performance of the applied field than  $V_{tm}$  ( $82 \pm 8$  kV). Only the velocity of the species is taken into consideration with  $V_{tm}$ , as per Eq. 5.5, but  $V_N$  considers the performance of the field

based on its velocity, peak focusing and broadening effects, as per Eq. 5.6, expressed by both the peak migration time and peak width. Diffusion and injection error, which are the largest contributors to the peak width and negatively affect the resolution, must be taken into consideration, as well as the increasing effects of joule heating and adsorption with greater field strengths.  $V_{est}$  was determined from the non-linear migration time relationship to applied voltage and was found to be 192.0 kV, providing an estimate that is between the  $V_{tm}$  and  $V_N$ . Whilst  $V_{est}$  provides a more representative estimation than  $V_{tm}$ , it still does not consider the peak focusing and broadening effects of a higher electric field, but it does reduce the estimated range of the effective voltage to  $192.0 - 296.5 \pm 0.17$  kV.

When compared to previous high voltage electrophoretic separation experiments, the current experiment is simple, less cumbersome, cheaper, and safer. Disruptive Joule heating is an issue that has been avoided by using the inherently low current generator coupled with the small inner diameter capillary. Disruptive joule heating and excess power would become apparent from the observed separations, with the performance dropping with increasing joule heating. Current experimentation results in record high theoretical plates, therefore joule heating must be negligible in the current experimentation. Additionally, the dry air system provides a cooling and drying effect around the capillary, allowing for better heat transfer as well as removing surface water and dust that could propagate dielectric breakdown.

Difficulties persist when working with higher voltages. Dielectric breakdown is assumed to be the greatest factor in capillary deterioration. By increasing the voltage within the capillary, the voltage gradient across the capillary wall also increases causing a greater rate of breakdown. After a given amount of breakdown, a decrease in the strength of the capillary is observed, thus a reduced resiliency to bending which often occurs due to the influence of the electric field, resulting in crack formation and propagation. The resultant cracks lead to the electric field to leak out of the capillary to the surroundings therefore lowering of the separation efficiency or even the complete failure of the capillary structural integrity. Often the effects of the breakdown would be observed as a complete breaking of the capillary at a singular point with additional cracks in other locations, as shown in Figure 4.10. The solution for this possibly lies in the capillary material used or how the capillary is fixed in place to remove crack propagation but more investigation is required. The dry air conditions and straightened capillary allowed far longer lifetimes that surpassed previous iterations, both by Lee et. al. and others in the literature implementing ultra-high electrophoresis, with capillaries surviving over 200 minutes of experimentation.

*Chapter 5.6 – Conclusion*

## 5.7 Conclusion

We compared a Van de Graaff generator as a field generator in capillary electrophoresis to a commercially available 30 kV source, using a meter long capillary with an inner bore of 50  $\mu\text{m}$ . The experimental setup included measures that improve the lifetime of the capillaries used and general electrical safety. Separation of F and FITC is significantly faster when using the VdG generator. The FITC peak appears after  $275 \pm 12$  seconds, compared to  $758 \pm 57$  seconds for the 30 kV supply. In addition to the faster separations, the efficiency of the separation is much higher; with the FITC peak resulting in  $1.73 \pm 0.16 \times 10^6$  theoretical plates from the VdG generator separation compared to  $1.74 \pm 0.17 \times 10^5$  theoretical plates from 30 kV. From the theoretical plate number, we estimate the average voltage to be  $296.5 \pm 0.17$  kV. Estimating the applied voltage using the migration time of the FITC peak found the  $V_{tm}$  to be  $82 \pm 8$  kV. However, the electric field

and analyte migration times were determined to be non-linear along the capillary. This deviates from current ideal models; therefore, the voltage was estimated to be 192 kV from extrapolating the effects of various voltages below 30 kV on migration time. Injection time and applied voltage optimisations were performed, allowing for an unparalleled theoretical plate number of  $7.45 \times 10^7$  to be observed. 5  $\mu\text{m}$  capillary bores were implemented but these suffered from very rapid dielectric breakdown compared to the 50  $\mu\text{m}$  inner bore capillary. These initial optimisations and results show that the use of a Van de Graaff generator as a current source for ultra-high voltage electrophoresis is both feasible and promising.



## Chapter 6 – Conclusions and Outlook

### HOW COULD ALTERNATIVE TECHNOLOGIES BE IMPLEMENTED TO OVERCOME CURRENT LIMITATIONS IN MICROFLUIDICS?

This question was approached in the four chapters with a common theme being the application of 3D printing to overcome manufacturing limitations. Additionally, a current supply was used to mitigate adverse effects of implementing ultra-high voltage electrophoresis. Here is a chapter-by-chapter summation of thesis.

#### 6.1 Chapter 2 – 3D printed moulds for the production of microgel liver cell encapsulation devices.

Microfluidic iterative prototyping is slow and expensive. Each new design requires a new mask, mould, or stamp, taking time and resources. 3D printing was employed as a method to produce rapid and cheap moulds for the production of devices with channels with sub-200  $\mu\text{m}$  features. These devices were used to produce sub-100  $\mu\text{m}$  cell-laden microdroplets that would be crosslinked into microgels. The cells within the microgels showed high viability rates and proved to be valuable models for biological assays and smart food delivery systems by others. During the development of this device, two additional factors had to be considered for the operation of the device. Firstly, cytotoxic effects of surfactant needed to be eliminated. Secondly, the device would block from the premature gelation of gelatin within the device. Both issues are common in microfluidic platform development, and here they were eliminated using integrated heating and cooling channels. The heating eliminated the gelation blocking the device, and the cooling eliminated the need for surfactants to stabilise the droplets within the device. In summary, device cost was reduced.

#### 6.2 Chapter 3 – Rapidly prototyped 3D printed flow cell the screening of extracellular lectins via glycomimetic liposomes.

*(Publication title: Targeting extracellular lectins of Pseudomonas aeruginosa with glycomimetic liposomes – Journal of Materials Chemistry B, 2022, DOI: 10.1039/D1TB02086B)*

Surface coatings for flow cell assays are prone to variation in density. This is problematic for the analysis of drug delivery vesicles, liposomes, to the surface proteins of bacterial biofilms. Here the same 3D printing techniques was used to develop customised microfluidic flow cells, demonstrating the versatility of such a technique. Devices presented four flow cells in one device designed to mimic the scale of a medium sized artery, providing biomimetic pressure and flow conditions. Fabrication was modified to include the bonding of the structured PDMS to hydrogel coated glass slides, eliminating hydrogel coating density variation. This was a collaborative work with further description of the glycomimetic liposome formulation and analysis available in the co-written publication.

#### 6.3 Chapter 4 – Three-dimensional bioinspired intertwining channel multiplexed droplet generator.

*(Patent title: Monodisperse micro droplet producing device and method of producing the same as.)*

3D structures are difficult, time consuming and expensive to produce and are often just stacked, folded or intersecting 2D structures, hence the 3D element is not integral to the function. Here, a bioinspired multiplexed (x64) droplet generator with intertwining channels was 3D printed. Using a geometric sequence for the area of a channel, following the scaling laws of microfluidics, the design of scaling of the device was simple and the fabrication was even easier. This was the fraction of the cost and difficulty than traditional stacked devices. Whilst initial air in water experimentation with the multiplexed device simply demonstrated that the channels were open, droplet generation proved to be more problematic. Simplified singular versions of the device, planar and 3D, were fabricated and tested to provide estimates for the operation of the multiplexed device. Such devices would seek to bridge the gap between microfluidics and industrial production processing, where multiplexing and variation between individual devices operated in parallel remains too high. Additionally, microfluidics often has low channel volumes compared to the material volume of the device. 3D printing allows for vastly higher channel density, thus increasing the effective material used.

#### **6.4 Chapter 5 – Development of an ultra-high voltage electrophoresis system using a Van de Graaff generator capable of $10^7$ theoretical plates.**

Higher resolution electrophoretic separations require higher electric field strengths. Increasing field strength requires a higher applied voltage, but ultra-high voltages (Over 30 kV) incur joule heating and dielectric breakdown. This cripples the performance of the separation or breaks the capillary. Previous experimentation using a Van de Graaff generator, an electrical current generator, had shown promising results but required refinement and still suffered severely from dielectric breakdown. Implementation of a new experimental setup which consisted of a dry air flow system, insulated cabinet, and insulating custom 3D printed parts surrounding the capillary are assumed to have reduced the number of locations for the electric field to discharge or tunnel towards. This increased capillary lifespan to over 200 minutes. Experimental conditions were improved, such as improving the injection volume, resulting in record breaking theoretical plate numbers. Such observations would not have been observed without longer capillary lifespans.

#### **6.5 Summary**

Three aspects of microfluidic limitations were overcome using non-conventional methods.

1. Lithographic prototyped moulds are expensive, time consuming and resource intensive. 3D printing provided a faster, cheaper, and less wasteful way to produce functional microfluidic moulds. Moulds were implemented to produce droplet generators and flow cell devices with comparative performance to commercial devices.
2. Current micro-fabricated chips are designed using a 2D approach, adopted from microelectronic circuit board design. 3D printing provides an alternative design and fabrication technique that is not limited to two effective planes. 3D droplet generating devices were produced to prove the improved applicability and improved device density.
3. Commercialised electrophoretic separations are limited to 30 kV, limiting separation resolution at the benefit of instrument lifespan. A VdG generator, a current source, was used to provide an electric field of limited current, resulting in higher performances alongside extended instrument lifespan.

All these methods provide alternative solutions to some of the critical limitations facing microfluidics. If microfluidics is to continue evolving at the rate observed in the past, then it means that the fabrication and experimental technologies used should evolve too. 3D printing is a rapidly growing technology that has only been commercially available in the past few decades. It holds a potential that grows with every passing day, so it is only natural that microfluidics should coevolve with it. Meanwhile, what are currently considered outdated technologies, such as the VdG generator, may just need to be implemented in new and creative ways to continue pushing the field to new and exhilarating boundaries.

## 6.6 Outlooks

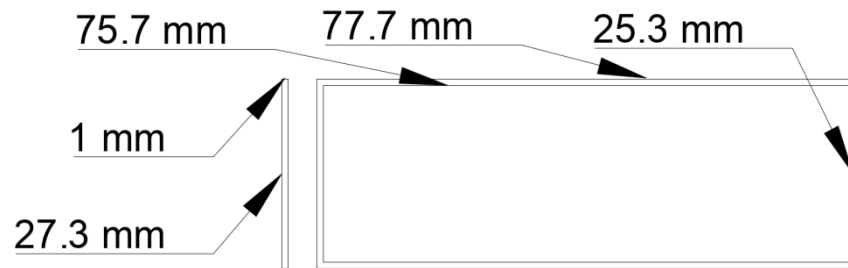
Whilst ultra-high voltage electrophoresis is an exceptionally niche demand, it is still in demand especially when dealing with samples that are incredibly similar in structure and hydrodynamic volume. It only then makes sense of exceptionally niche solution to be presented. Current supplies or generators acting as a non-linear electric field source for electrophoresis are incredibly under researched. Yet, such a simple configuration is already outperforming other ultra-high voltage electrophoresis experimentation. This warrants further investigation and could hold the key to safe and accessible ultra-high resolution separations.

3D printing is a powerful tool. All the work described within this thesis required it in some form or another. All the presented designs, fabrication and experimental setups were built by an individual scientist with a master's in chemistry and a passion for technology, who also has had no formal engineering education and was only introduced to 3D design and printing at the beginning of their doctoral studies. So not only is it powerful, but it is extremely accessible, adaptive, and as complex as the user wants it to be. The more restrictions removed from design and fabrication, the more freedom a scientist has to invent and produce truly novel microfluidic structures. As 3D printing improves and begins to reach sub-50  $\mu\text{m}$  and even sub-10  $\mu\text{m}$  resolution, it means that the microfluidic community has begun to shift opinion of 3D printing. The shift is away from "if 3D printing will be used", and towards "how 3D printing will be used" to overcome the current limitations. We live in a 3D world, so it is only natural for our technology to evolve into this 3D space too.

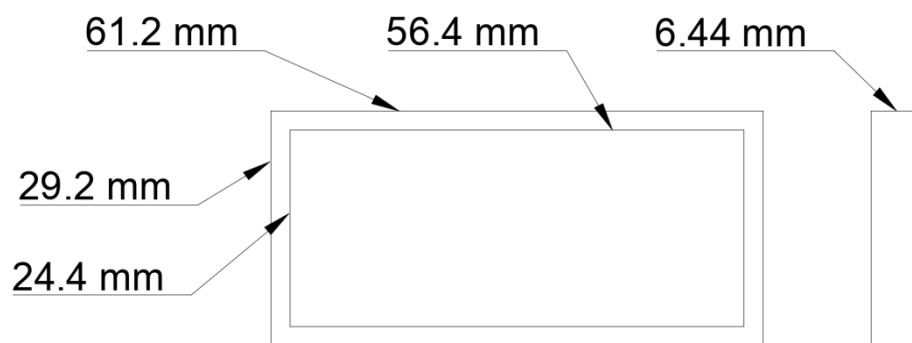


# Appendices

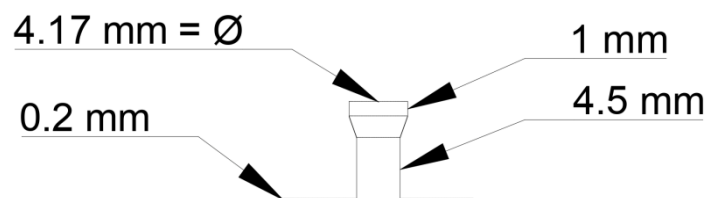
## Chapter 2 Support Information



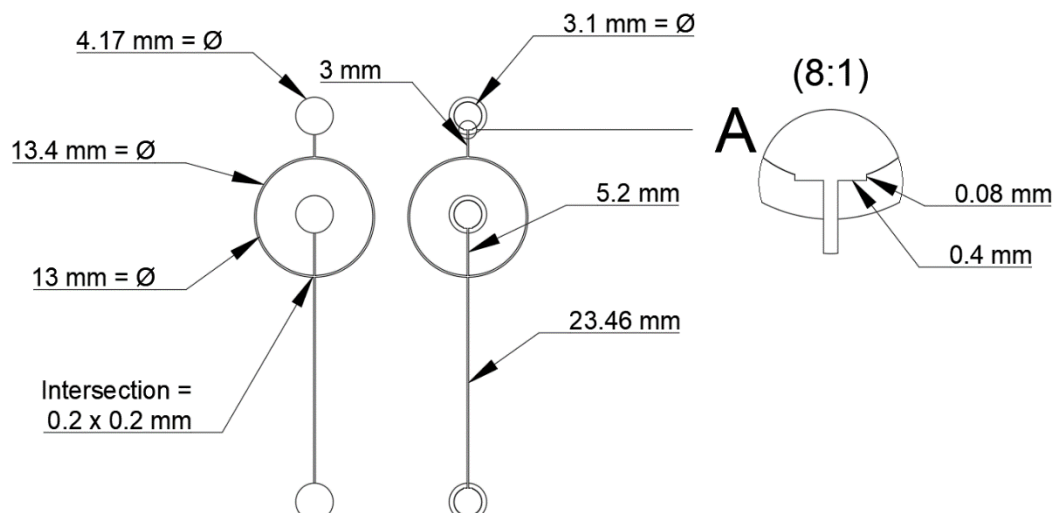
Support Figure 1.1: Support ring which would be 3D printed and upon completion was loaded with a glass microscope slide. This design was used throughout all designs using a standard microscope slide.



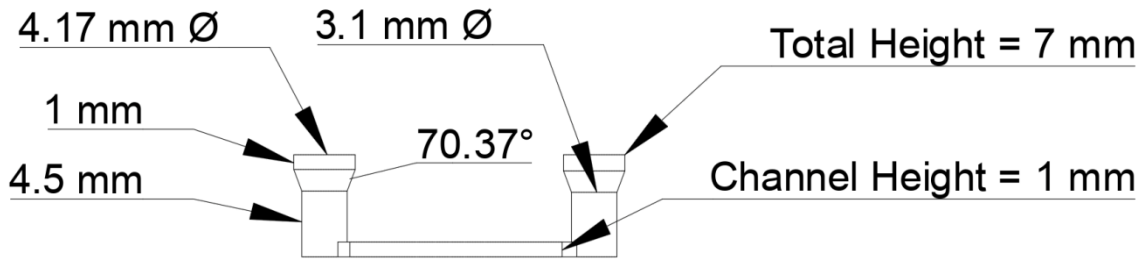
Support Figure 1.2: Schematic of the final outer PDMS mould used with magnetic filament. Earlier iterations used thinner, less stable moulds due to the faster print times.



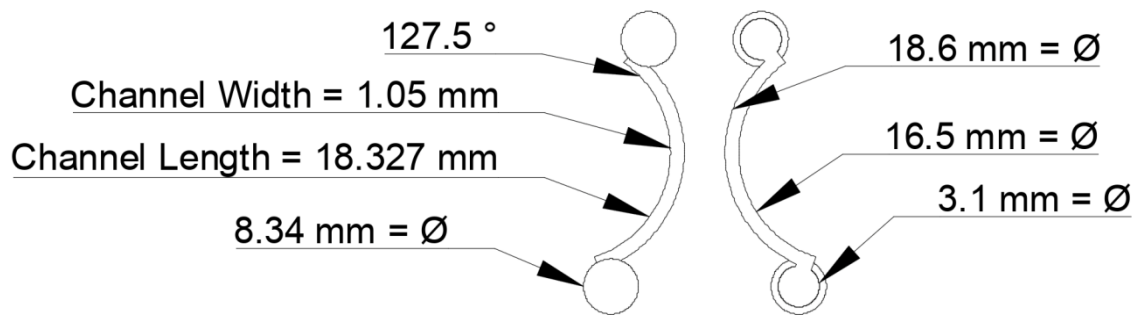
Support Figure 1.3: Profile schematic of the droplet generation channel.



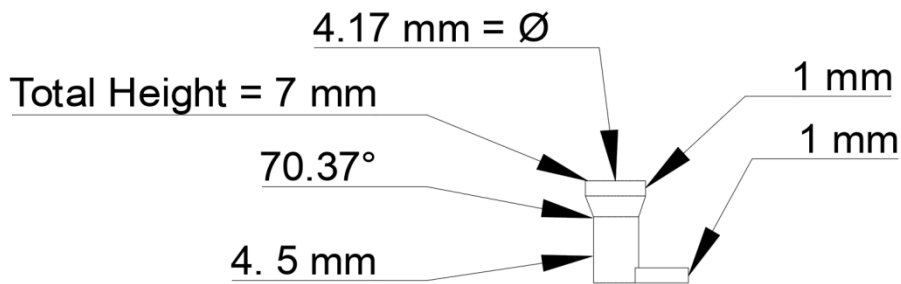
Support Figure 1.4: Droplet generation channel mould observed from the top (left) and bottom (right). A) shows how the connections of the inlets/outlets-channel connections were designed to force the slicer to overlap the filament, hence a seamless connection. Typically, the circular and straight-line intersections result in the slicer to separate the two paths, forcing a lift off and small disconnect. This could result in a negative relief with a blocked or incompletely open channel.



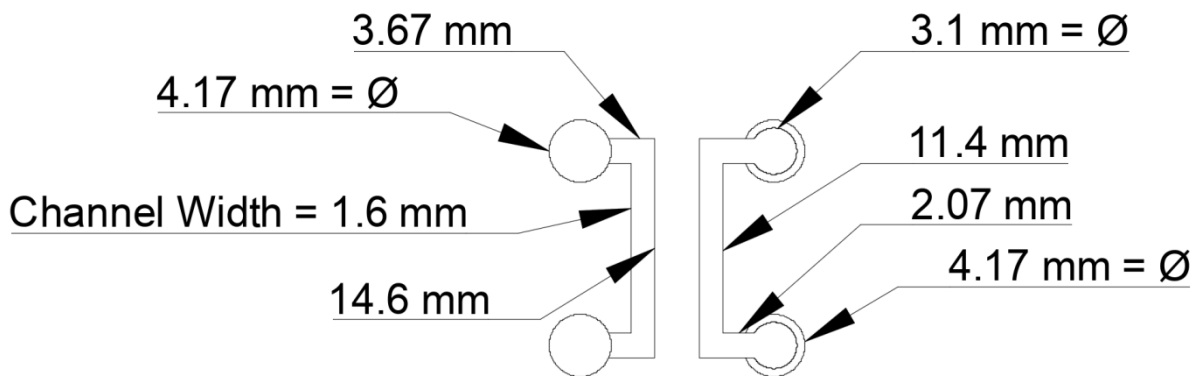
Support Figure 1.5: Profile of the heating channel moulds.



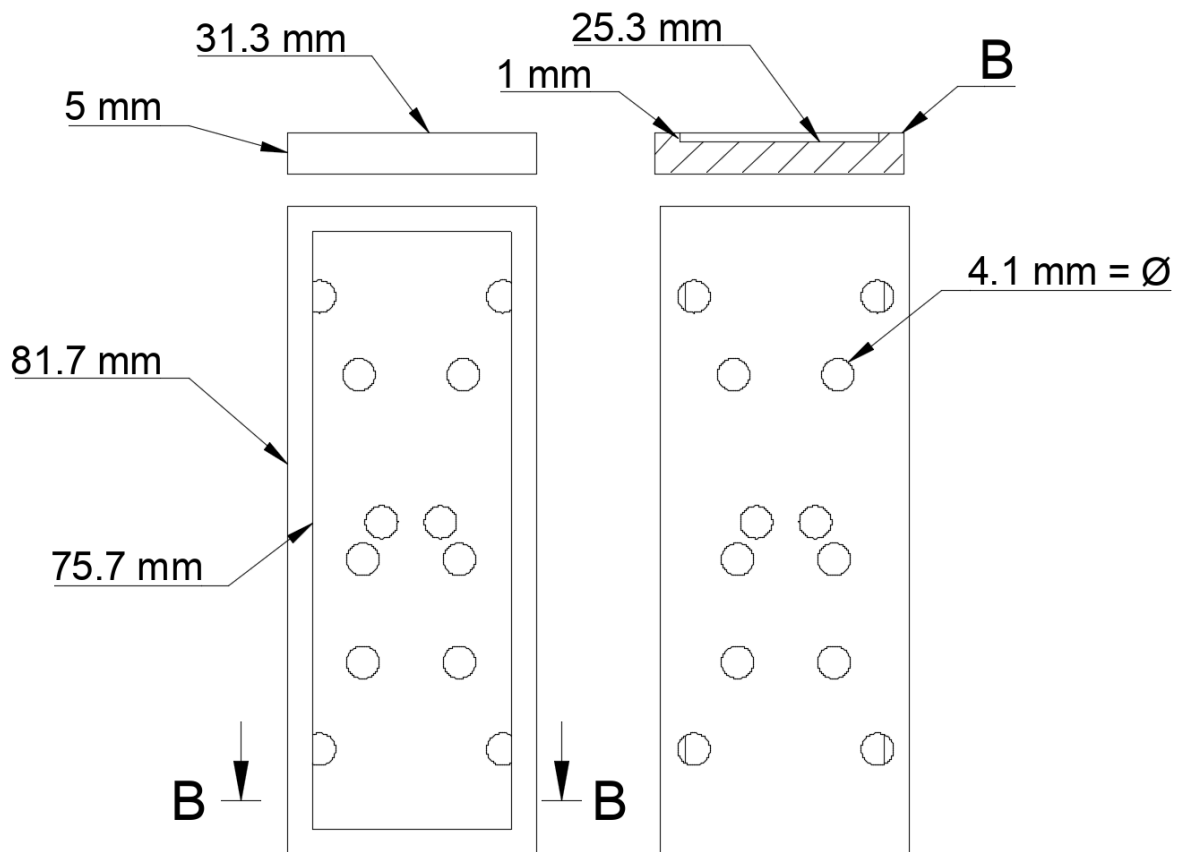
Support Figure 1.6: The right heating channels mould observed from the top (left) and bottom (right). The mould of the left side is a mirror design.



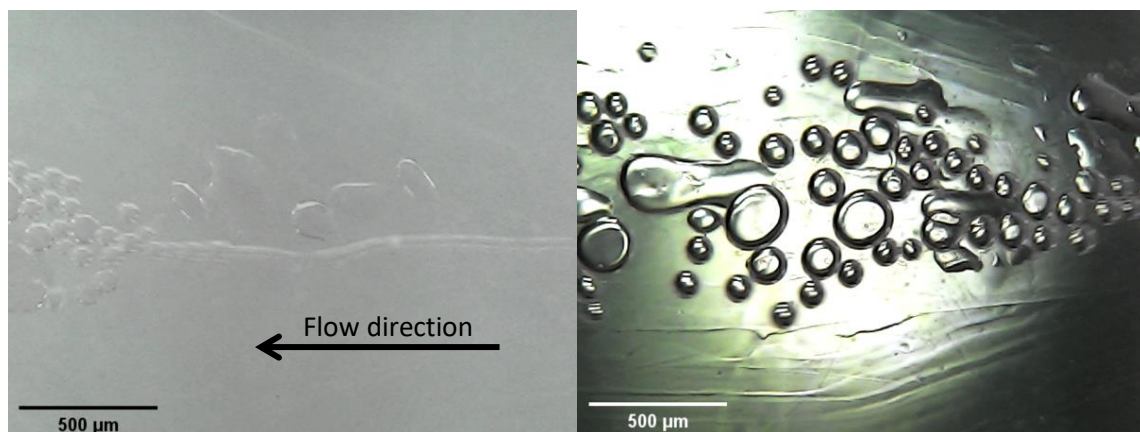
Support Figure 1.7: Profile of a cooling channel mould.



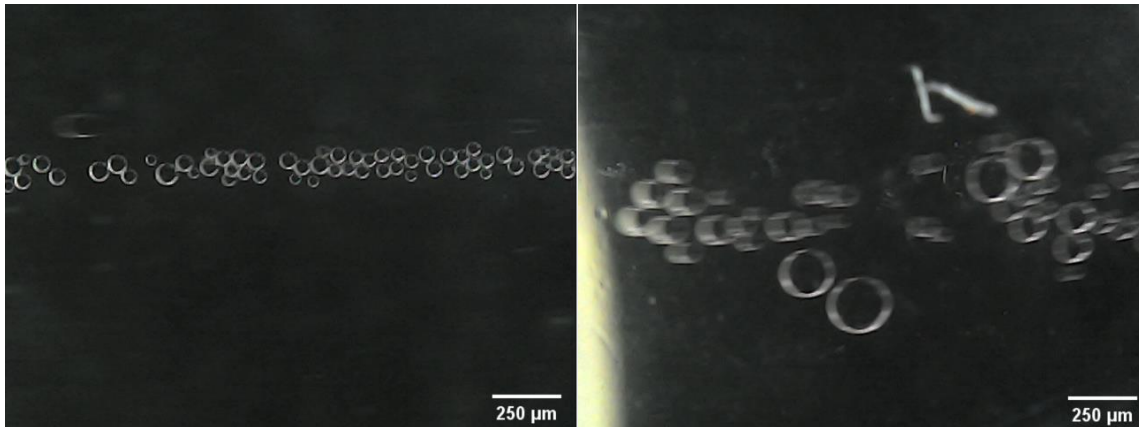
Support Figure 1.8: The cooling channels mould observed from the top (left) and bottom (right). The mould of the opposite side is a mirror design.



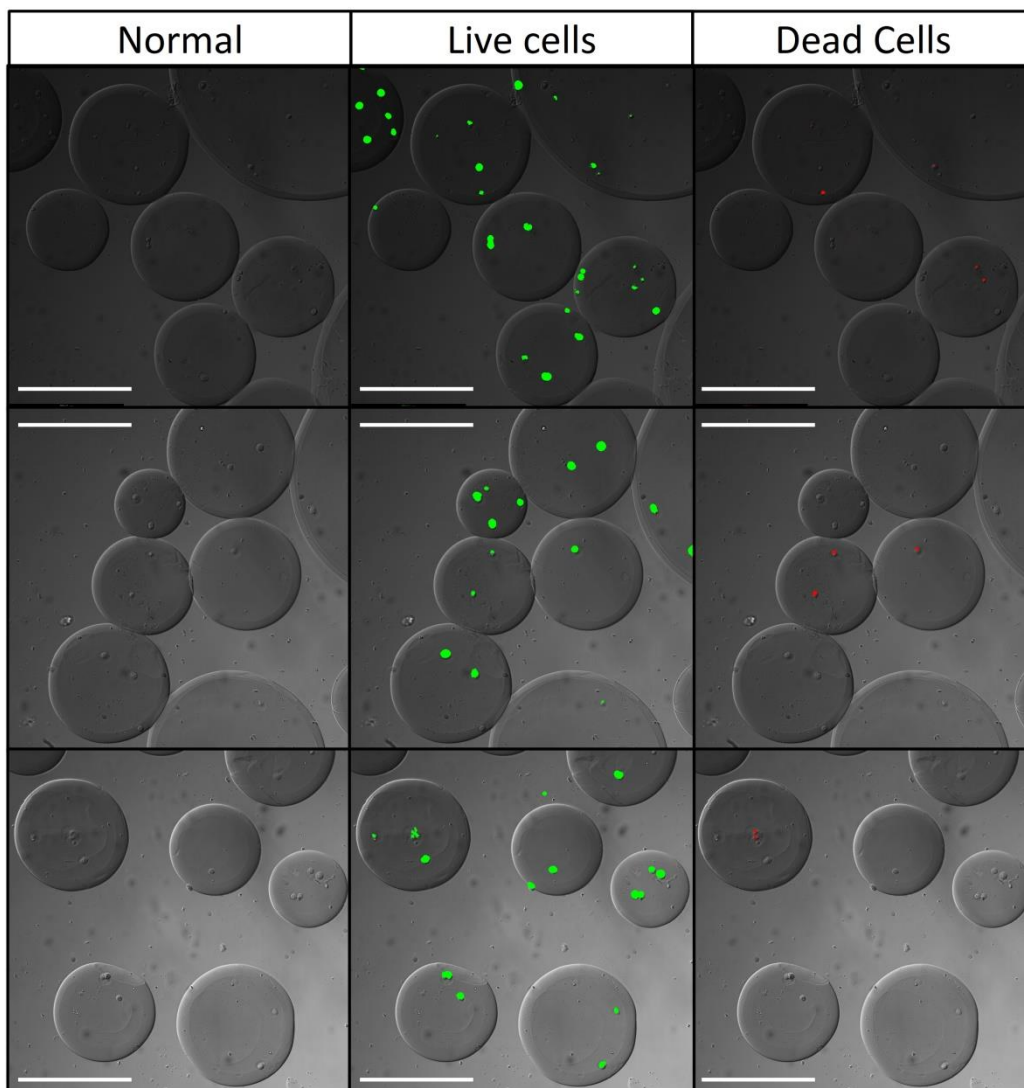
Support Figure 1.9: The 3D printed (SLA) magnetic alignment bed. Top left is the short side profile of the bed and top right is a section view of position B, showing where the microscope slide slides into position. Bottom left is the bed observed from above and bottom right is the bed observed from below. Upon printing, 4 mm x 4 mm x 4 mm cylindrical magnets were inserted into the holes and glued in place.



Support Figure 1.10: The observed effect of surfactant droplet in a microfluidic droplet generator. The device used was a variation of Figure 8(b). Left) Droplet generation without any surfactant. Dripping regime appears to be jetting with break-up occurring 3 mm into the outlet channel. Jetting stream appears a contour in the roof of the channel, an unintended by-product of the 3D printed mould using a less refined printer. Droplets were relatively uniform in size upon formation but then immediately collide and coalesce. Right) Jetting occurs at with stream breaking at 1.5 mm into the outlet. Droplets appear to be produced at a slower rate with greater size variation and still coalesce upon collision. Droplet spreading on the surface of the channel is also observed to a greater degree.

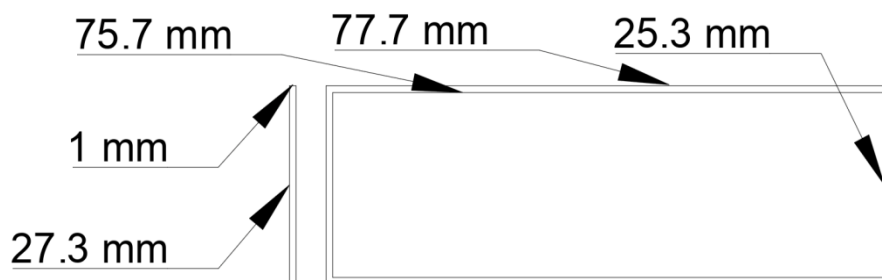


Support Figure 1.11: Droplet generation with a reduced flow rate to reduce droplet collision. Left) Droplets with a large dispersity of size. Droplets are observed at 1 cm along the outlet channel. Right) Approaching the outlet, observed by the light area on the left of the image, droplets of even greater variation are observed. This demonstrates coalescence still occurs despite the inclusion of the surfactant and the reduction of flow rates.

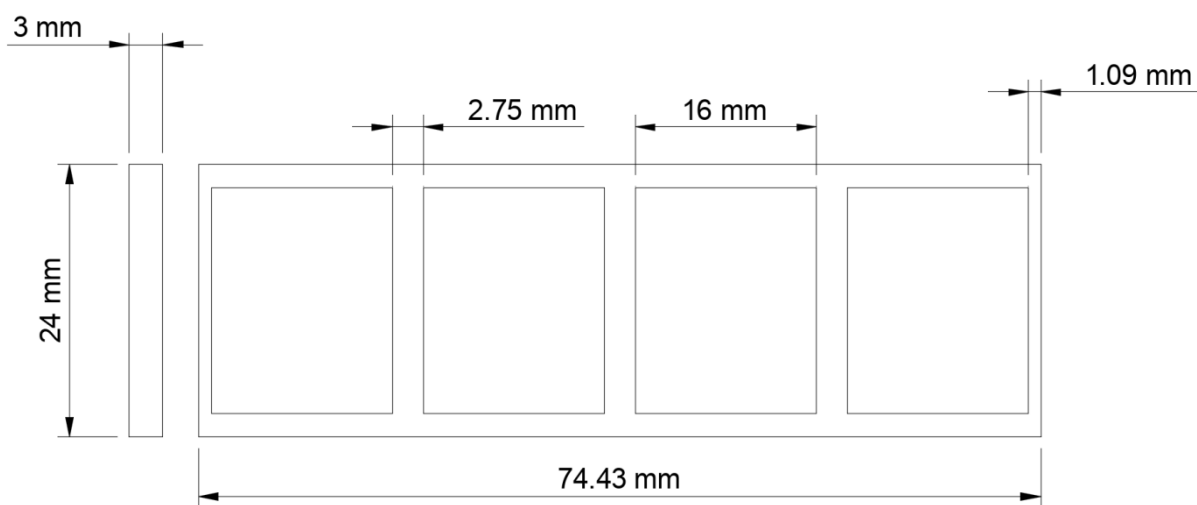


Support Figure 1.12: Additional examples of cell-laden microgels. Viability rate is based upon cell counting from DIC and fluorescence microscopy, calcein-AM (Live/Green) and propidium iodide (Dead/Red) staining™. Scale bar = 220 μm.

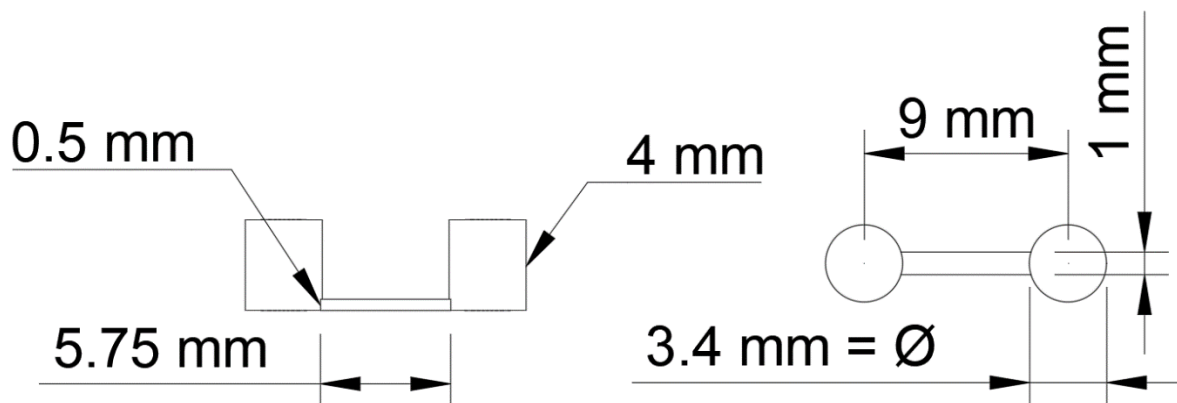
### Chapter 3 Support Information



Support Figure 2.1: Support ring which would be 3D printed and upon completion was loaded with a glass microscope slide.

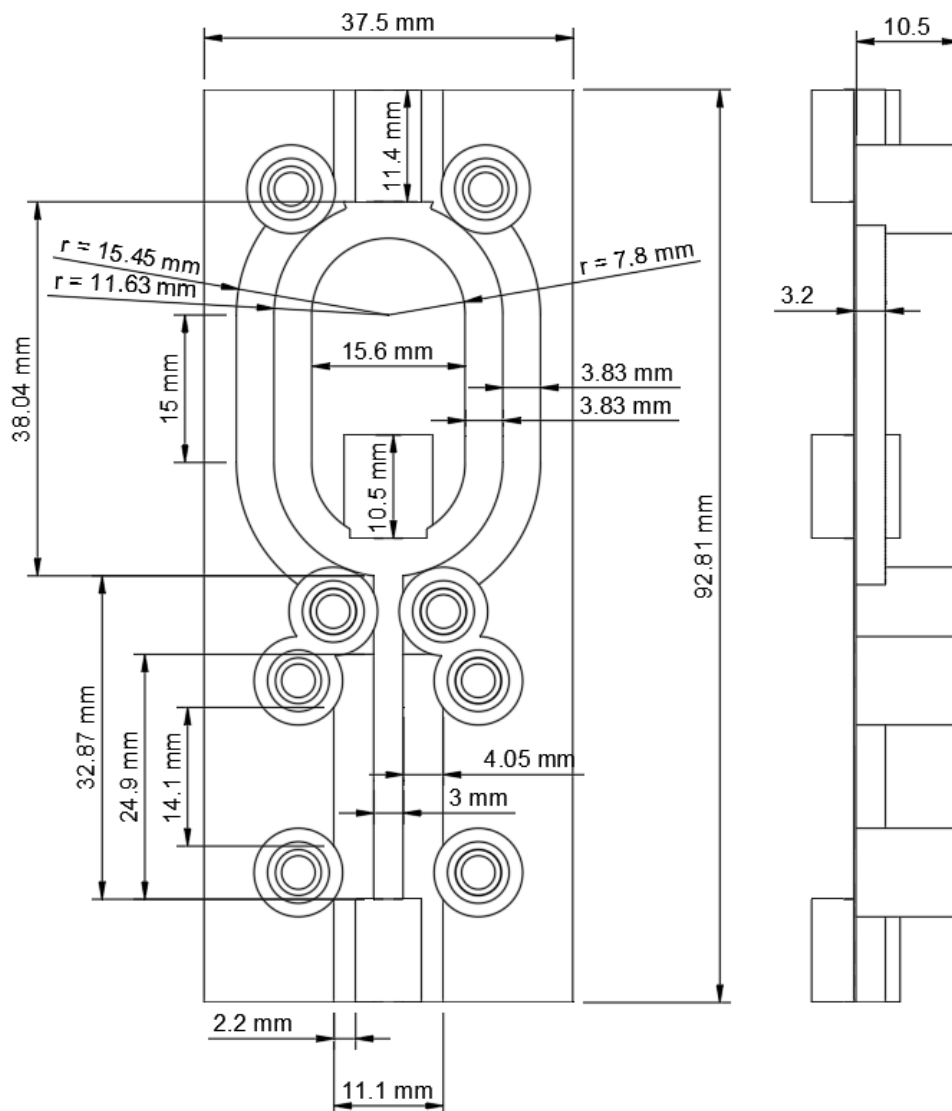


Support Figure 2.2: Schematic of outer 3D printed structure that would act as the bulk mould for the four PDMS flow cells.

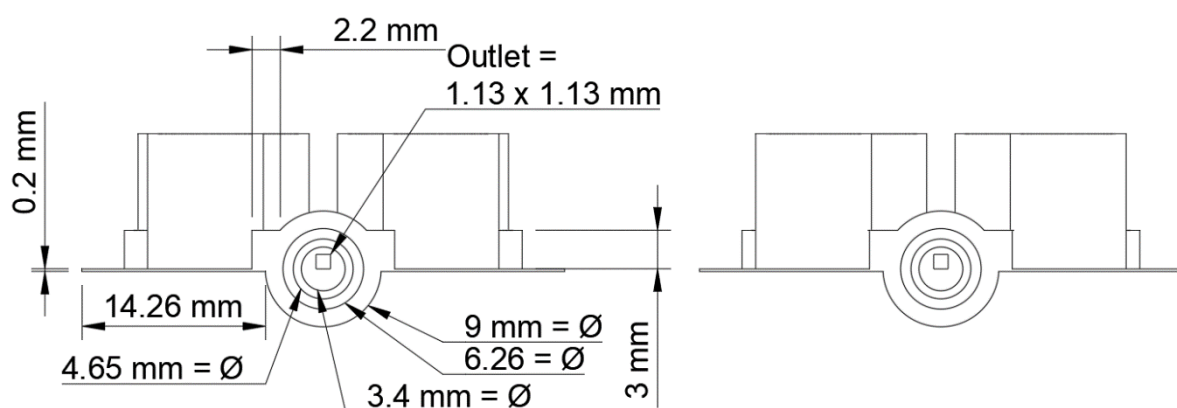


Support Figure 2.3: Schematic of the channel mould.

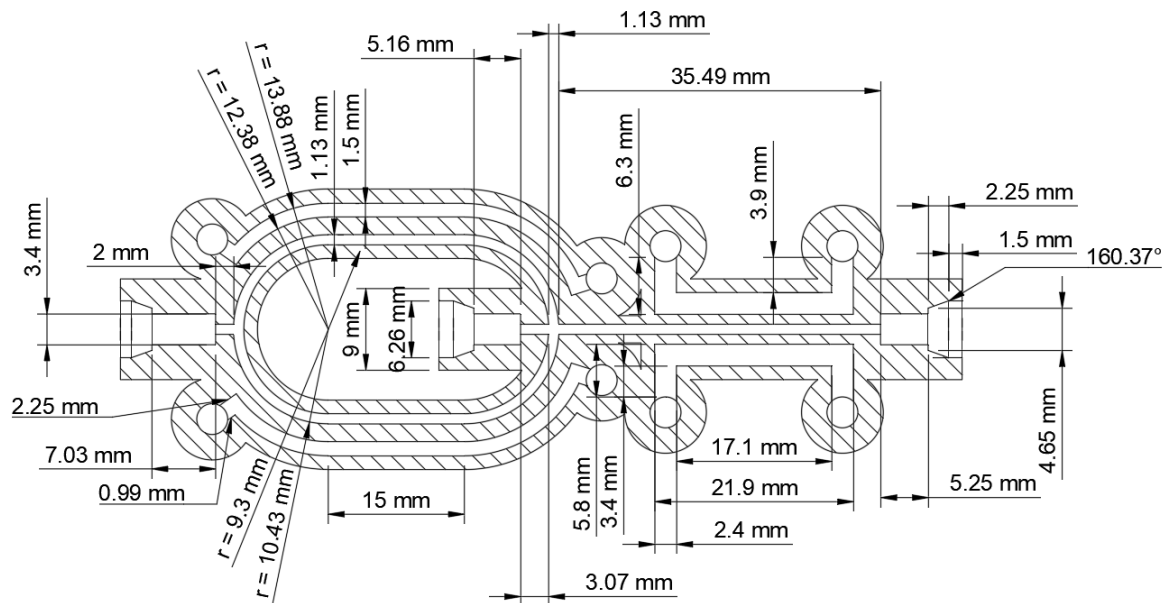
## Chapter 4 Support Information



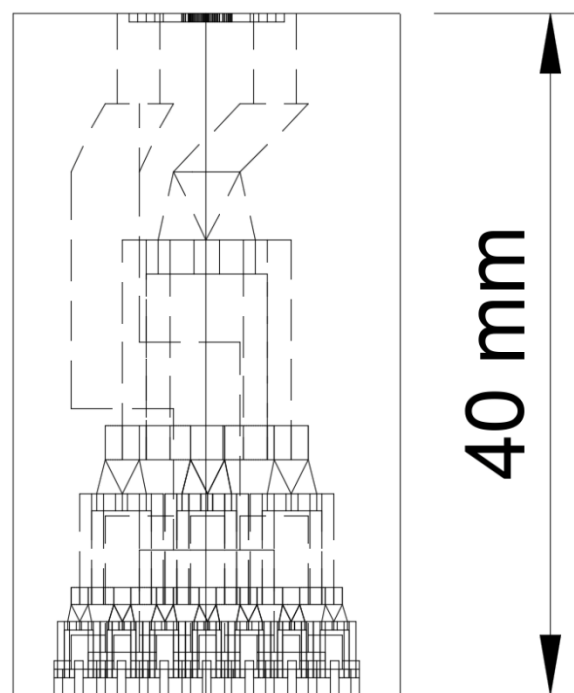
Support Figure 3.1: Schematic view of the planar device from above (left) and the side profile (right).



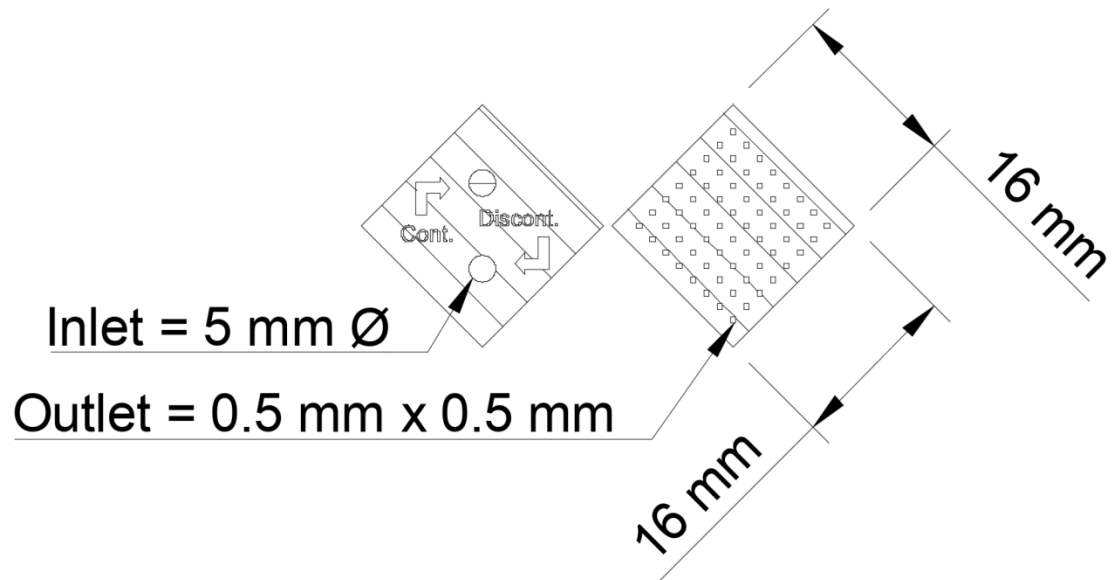
Support Figure 3.2: Outlet (left) and inlet (right) of the planar device.



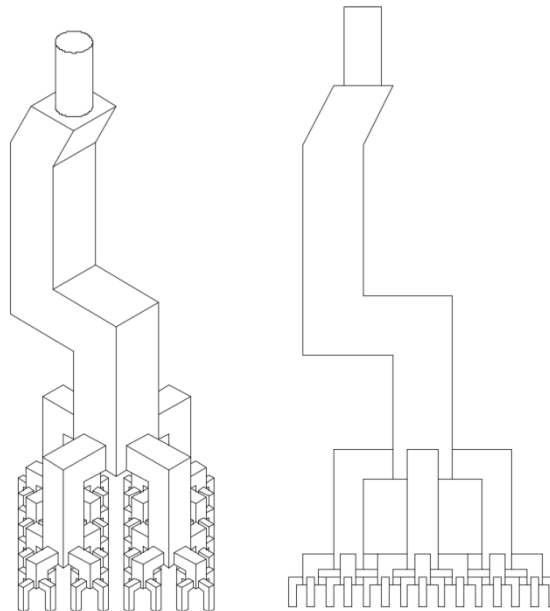
Support Figure 3.3: Schematic of the internal channel structure of the planar device.



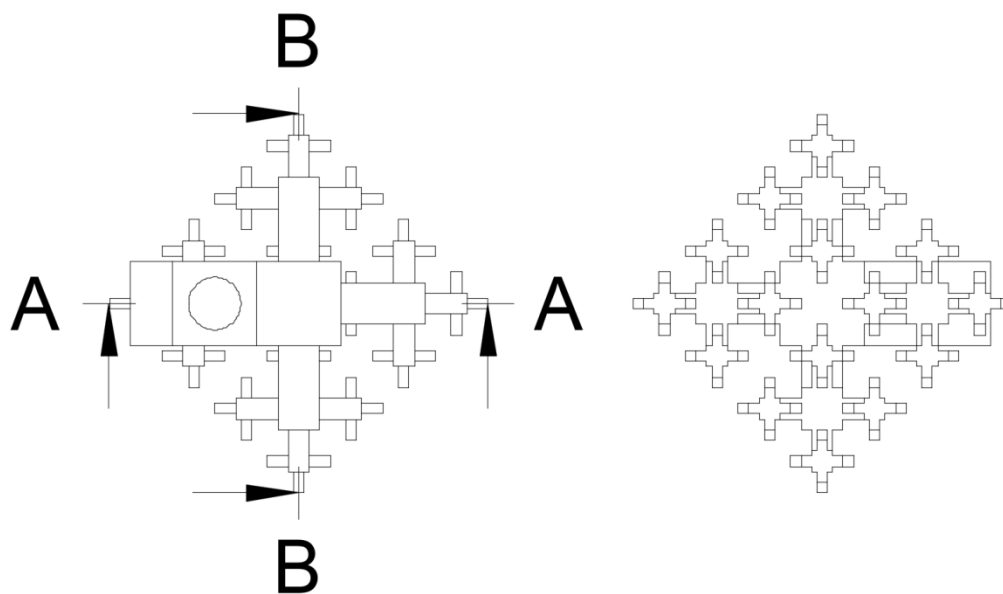
Support Figure 3.4: Schematic of the 3D intertwining channel device (64 outlets) with the internal structure. Device is rotated to  $45^\circ$  to allow for better visualisation of the internal structures to be "planar".



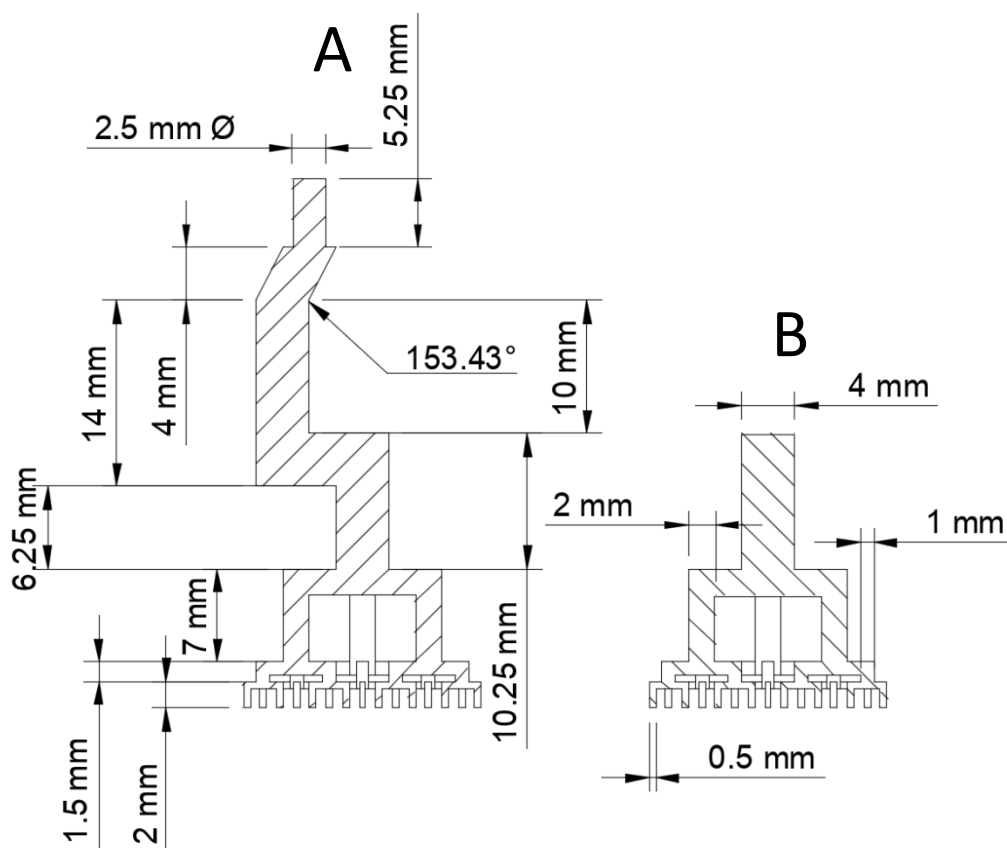
Support Figure 3.5: Inlet (left) and outlet (right) of the 64 outlet 3D device.



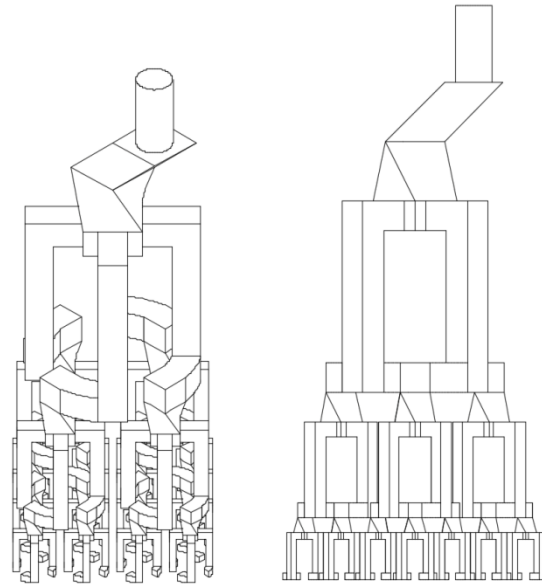
Support Figure 3.6: "3D" (left) and profile (right) view of the continuous phase channel.



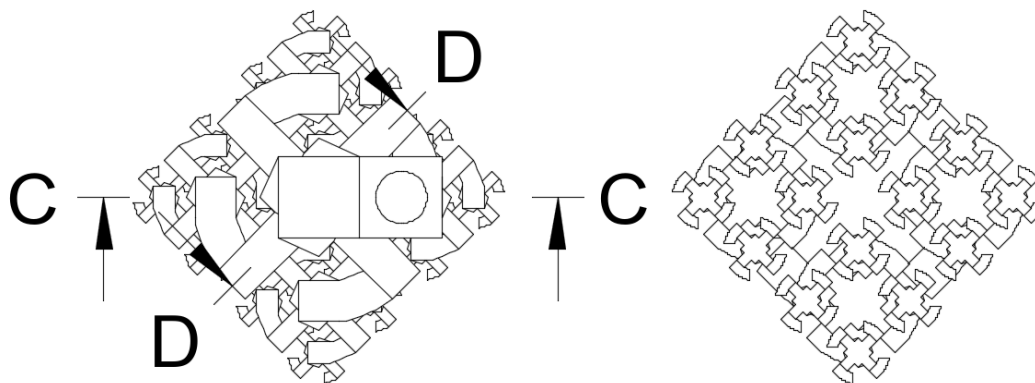
Support Figure 3.7: Inlet (left) and outlet (right) of the continuous phase channels. A and B indicate the “Section” line, and the resultant structures are shown in Support Figure 8.



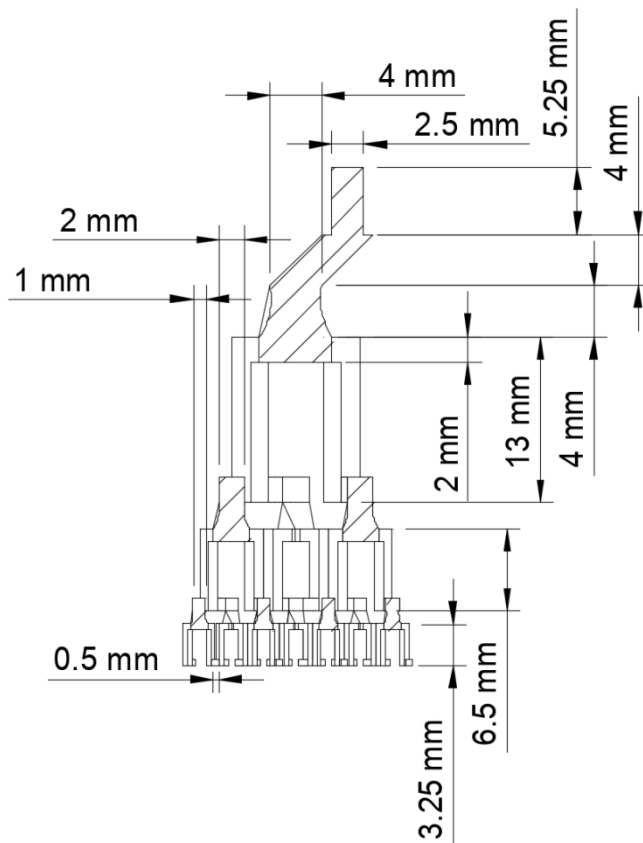
Support Figure 3.8: Schematic of the continuous phase channels. A and B are sections taken from Support Figure 7.



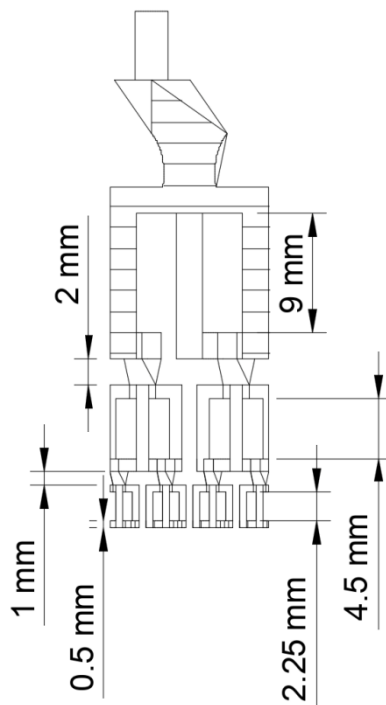
Support Figure 3.9: “3D” (left) and profile (right) view of the discontinuous phase channel.



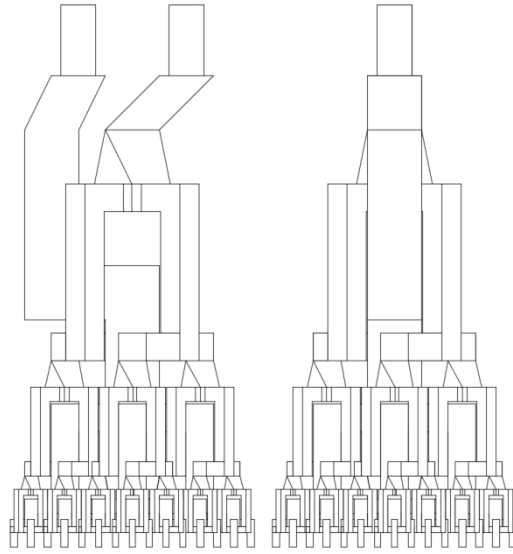
Support Figure 3.10: Inlet (left) and outlet (right) of the continuous phase channels. A and B indicate the “Section” line, and the resultant structures are shown in Support Figure 11 and 12.



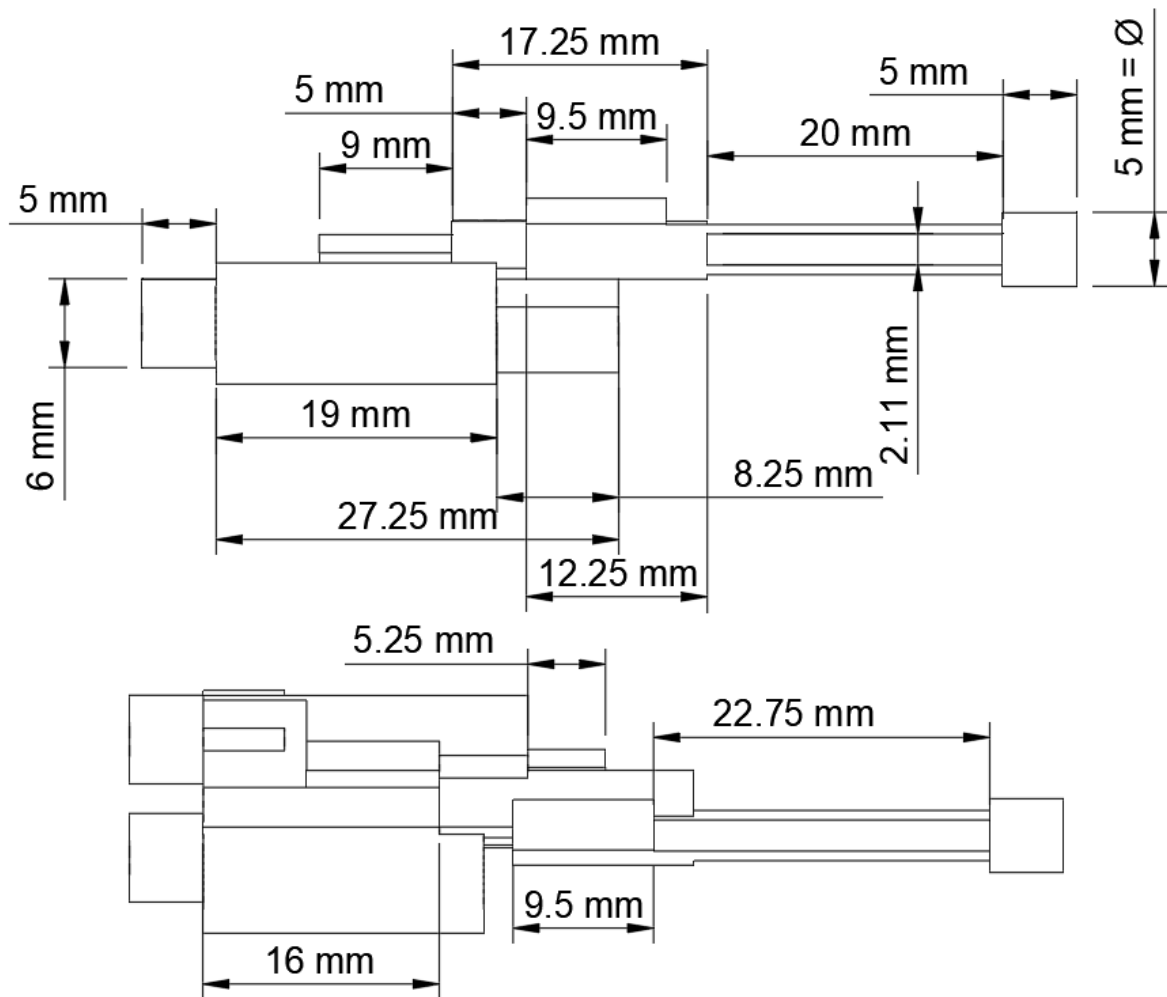
Support Figure 3.11: Schematic of the continuous phase channels, from section C of Support Figure 10.

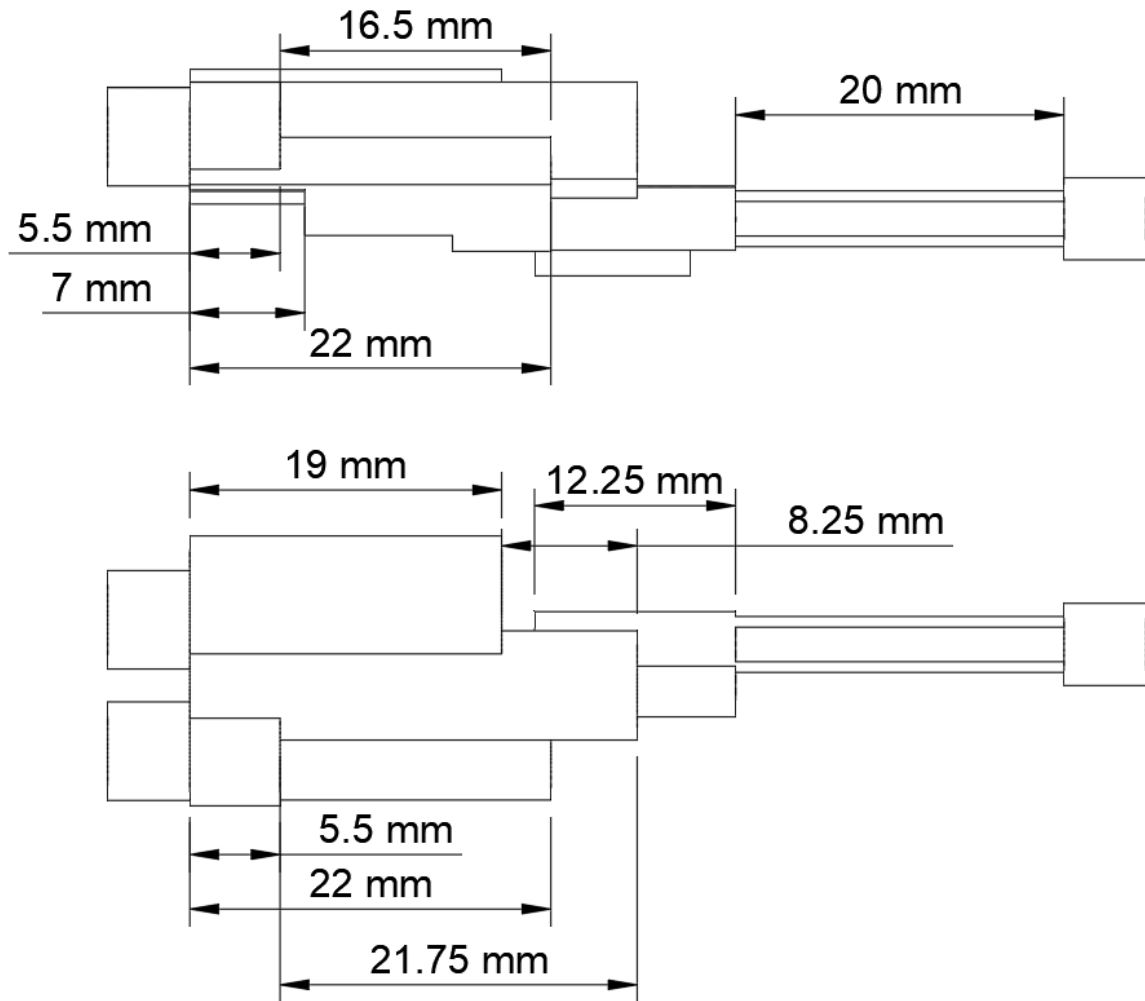


Support Figure 3.12: Schematic of the continuous phase channels, from section D of Support Figure 10.

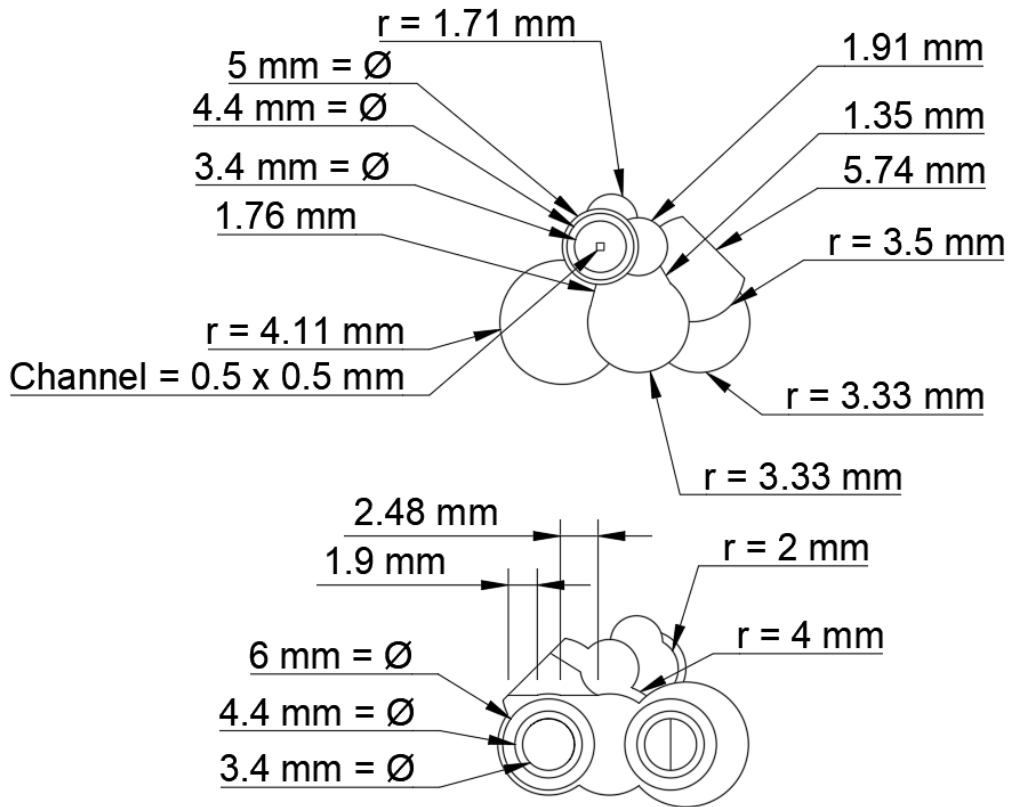


Support Figure 3.13: Left) Profile view of the intertwining channels depicted in Figure 2(b). Right) Profile view of internal channels rotated 90° with regards to Left.

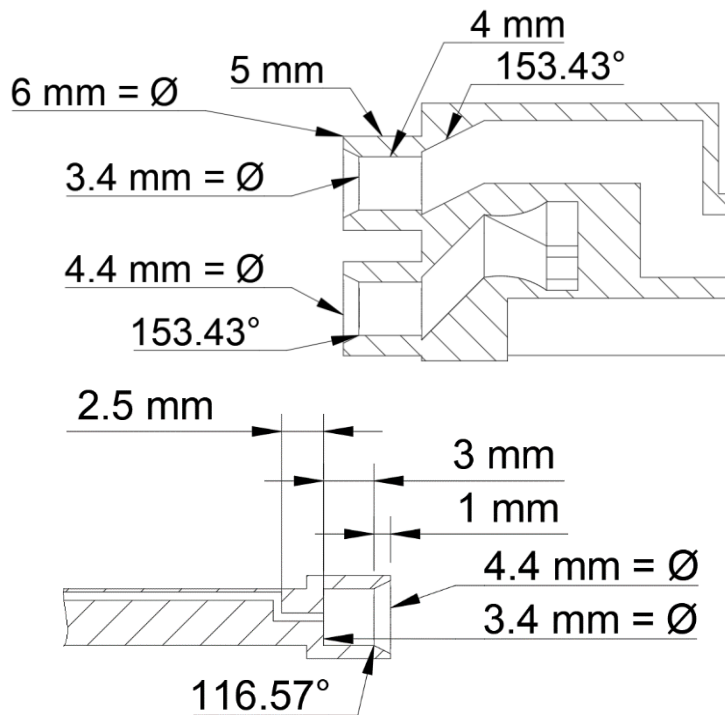




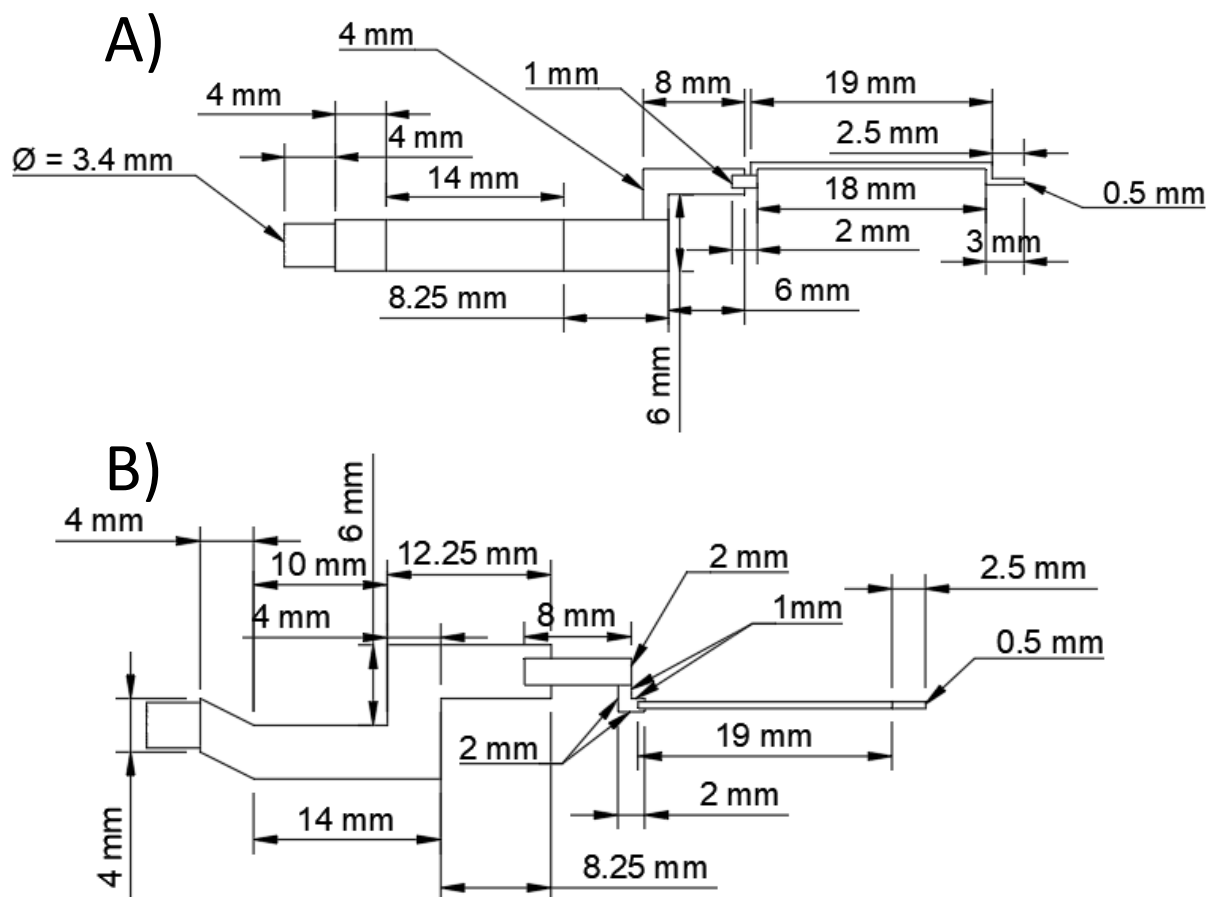
Support Figure 3.14: Four side profiles and dimensions of the body of the singular 3D device, Figure 3.



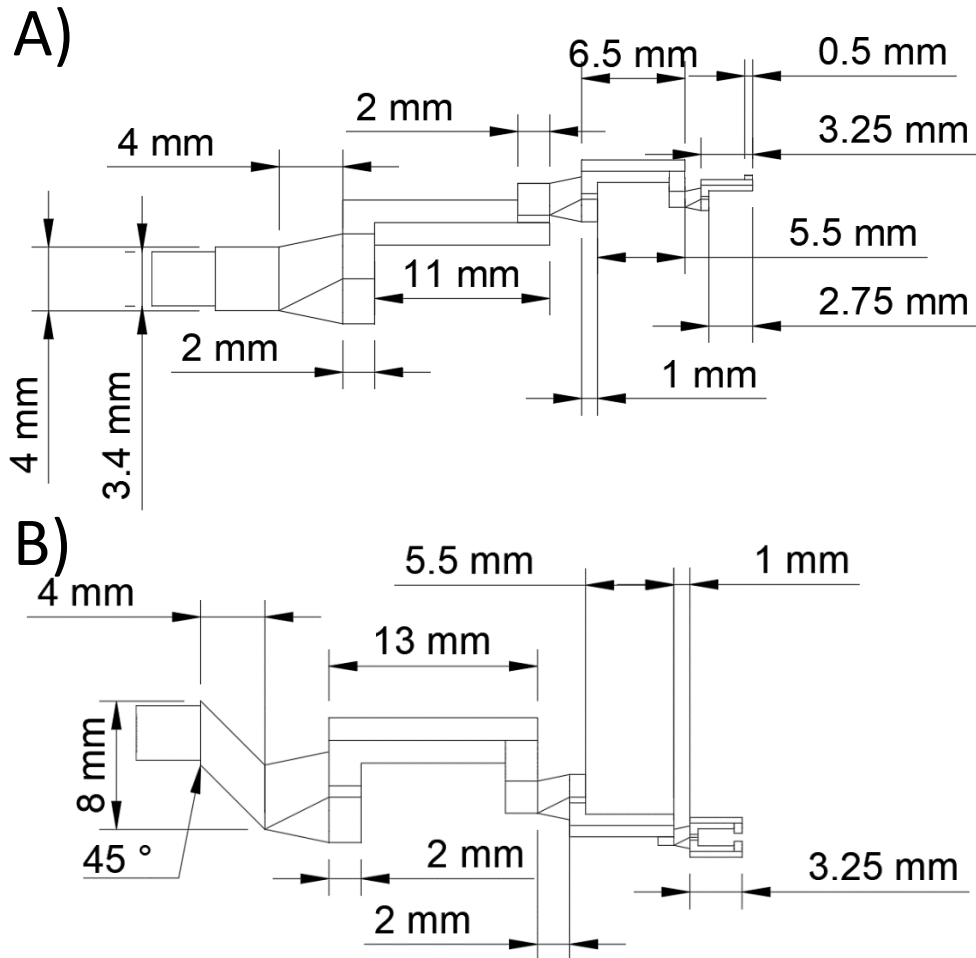
Support Figure 3.15: Outlet (top) and inlet (bottom) profile of the singular 3D device.



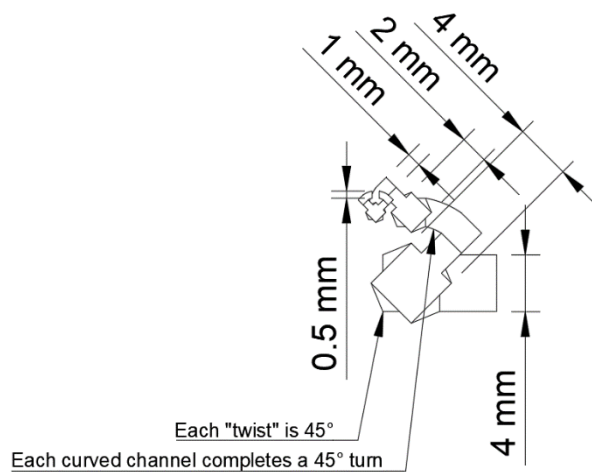
Support Figure 3.16: Section view of the outlet (top) and inlet (bottom).



Support Figure 3.17: A) Schematic of the continuous phase channel within the singular 3D device. (Side profile number 1 – Support Figure 14) B) Schematic of the same continuous phase channel rotated 90°. (Side profile number 2 – Support Figure 14)



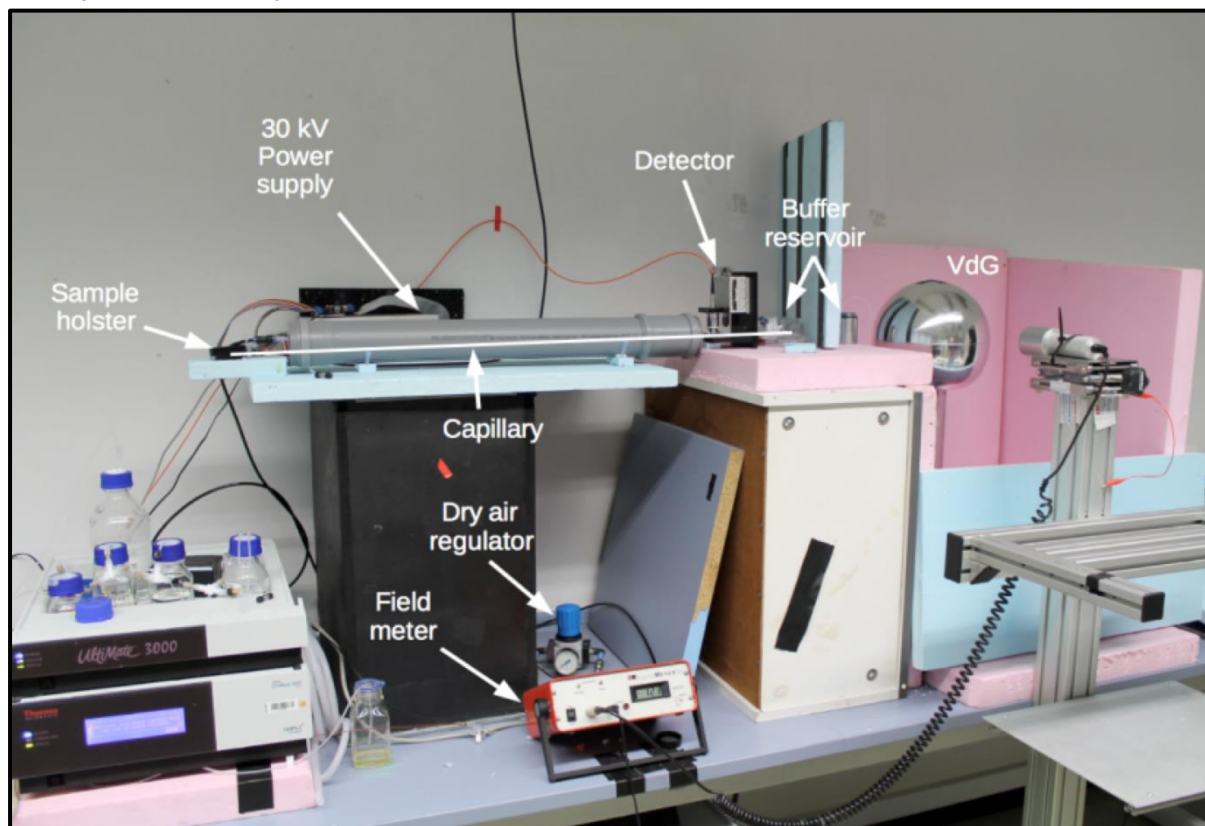
Support Figure 3.18: A) Schematic of the discontinuous phase channel within the singular 3D device. (Side profile number 1 – Support Figure 14) B) Schematic of the same discontinuous phase channel rotated 90°. (Side profile number 2 – Support Figure 14)



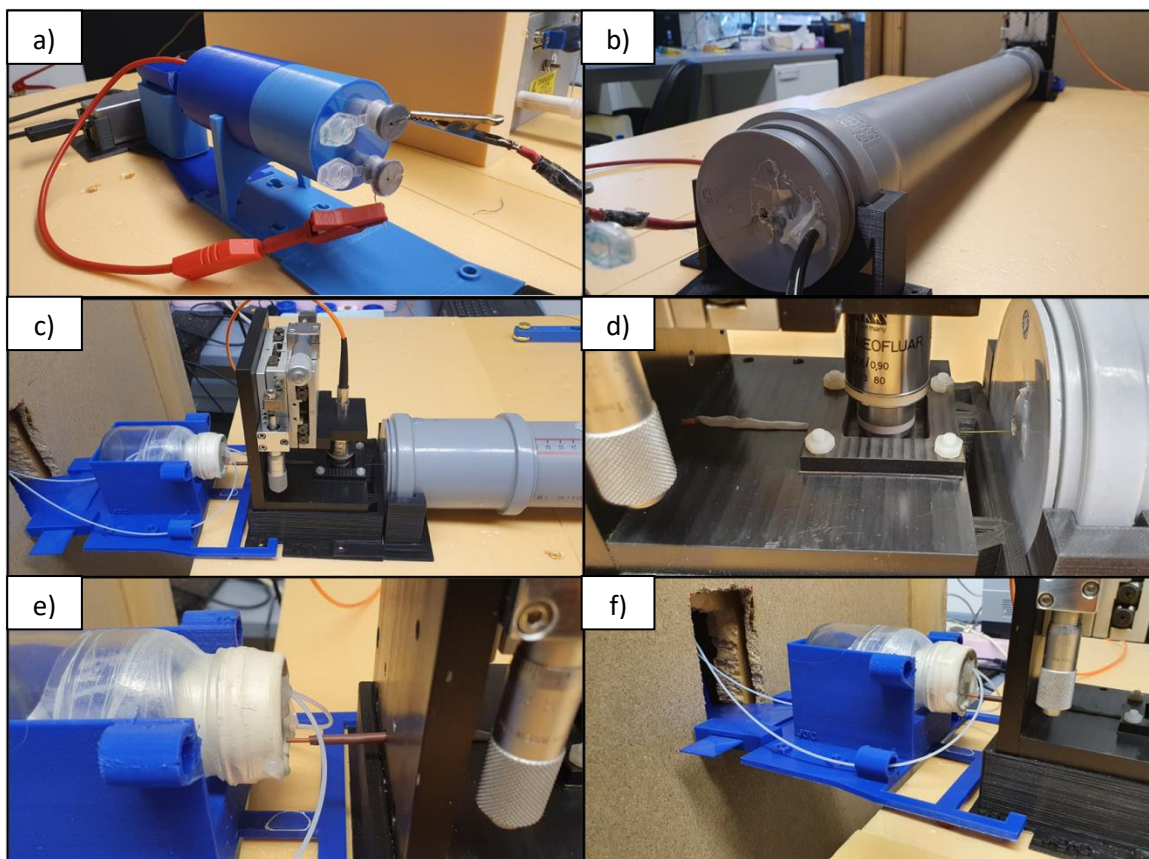
Support Figure 3.19: Schematic of the discontinuous phase channel within the singular 3D device from the perspective of the outlet. This perspective allows for the observation of the curvature of channel.

## Chapter 5 Support material

### 5.1 Experimental setup



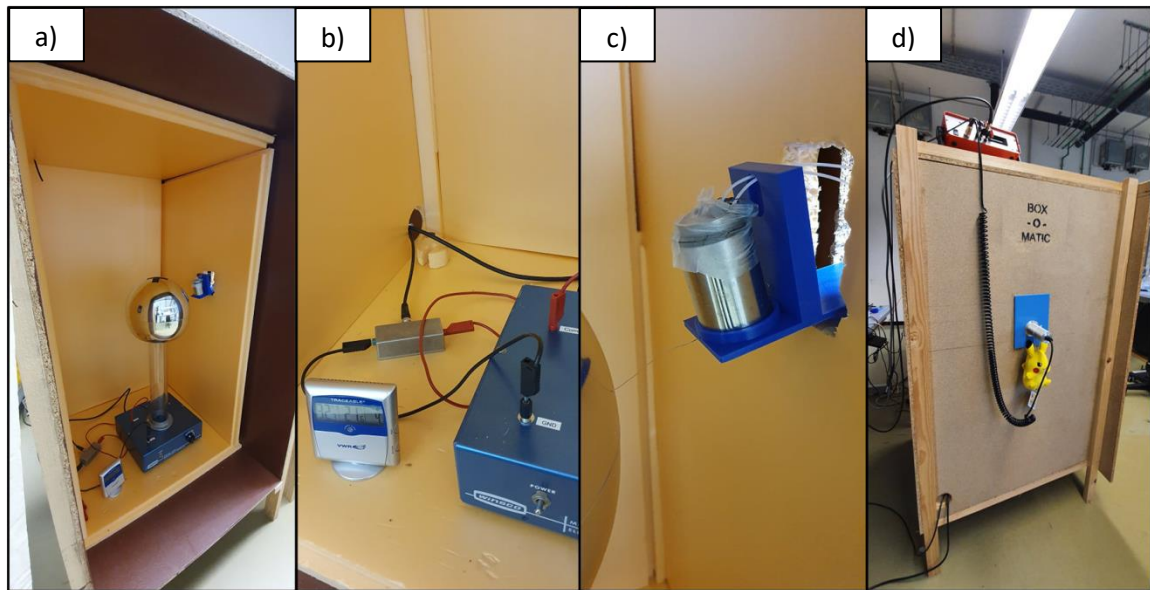
*Support Figure 4.1: Early iteration of the VdG generator separation setup. Here the first implementation of the dry air proved to extend the lifespan of the capillary as seen in Figure 2. This setup contained many metal elements which would gather charge and lead to safety issues. The boxes that the experiment rested upon were metal frames covered in either foam or wood. These frames would still gather charge. As would the frame which the field meter was mounted upon. These gathering in charges would lead to dangerous discharges to the user or to equipment, such as the pump, resulting in the system to crash and risk damage. The setup shown in Figure: 2 is the product of development with the aim or reducing the metal present and improving user and equipment safety.*



Support Figure 4.2: Zoom in of the key components on the insulated table. a) Sample holder and resistor/amp meter holder. The current holder would measure the current passing through the capillary from the VdG generator to ground. Both the sample and running buffer could be loaded simultaneously. The holder was retractable and rotated 180° to allow for accurate and rapid manual switching between the samples and running buffer. 3D printed Eppendorf caps sealed the sample and buffer in place, reducing observed evaporation and variation of electrode positioning. The current depicted configuration is for the separation phase. b) Insulated dry air tube. Inside was foam to aid in insulating the capillary and restrict the bending within. The black tube is the dry air inlet. Tape was placed over the capillary hole, which the capillary would pierce during preparation, keeping the tube airtight. c) The detection stage and second buffer well. Once the capillary was loaded into the detector, alignment was achieved by manually focussing the lens onto the capillary via the stage micro-screws. d) Zoom of the detection stage. Here the capillary leaves the insulated dry air tube and is held in the “detector”. The optics, VdG generator and the 30 kV power supply are the only remaining components of the previous experimental setup by Lee. et. al.<sup>199</sup> Adhesive putty is used to ensure the capillary remains flat in the detector. e) The capillary is held in an insulating rigid polymer and into the second buffer well. Glass was used here to ensure insulation; however, ozone would be detected in this region at high field strengths, indicating an ionising voltage was leaking in the vicinity. f) Salt bridges connect the first and second buffer wells together.

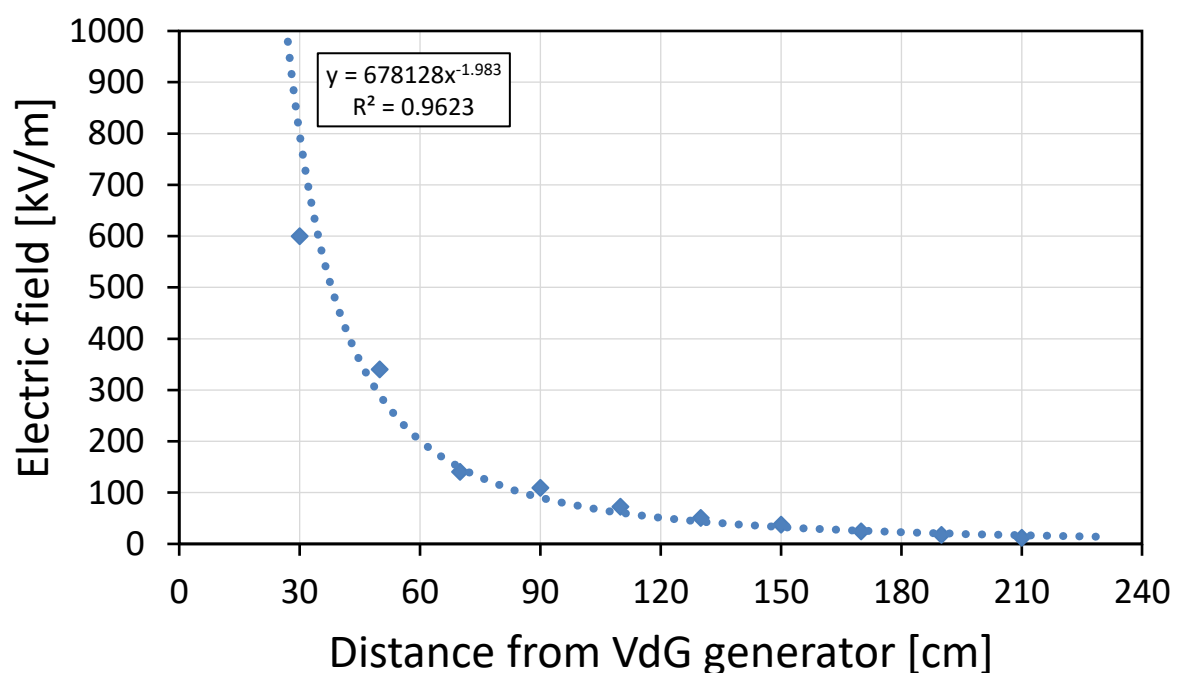


extended and retracted upon the locking pin at 90° of the loading assembly. Upon extension, the tumbler is locked into position, ensuring the sample is completely secure during the run.

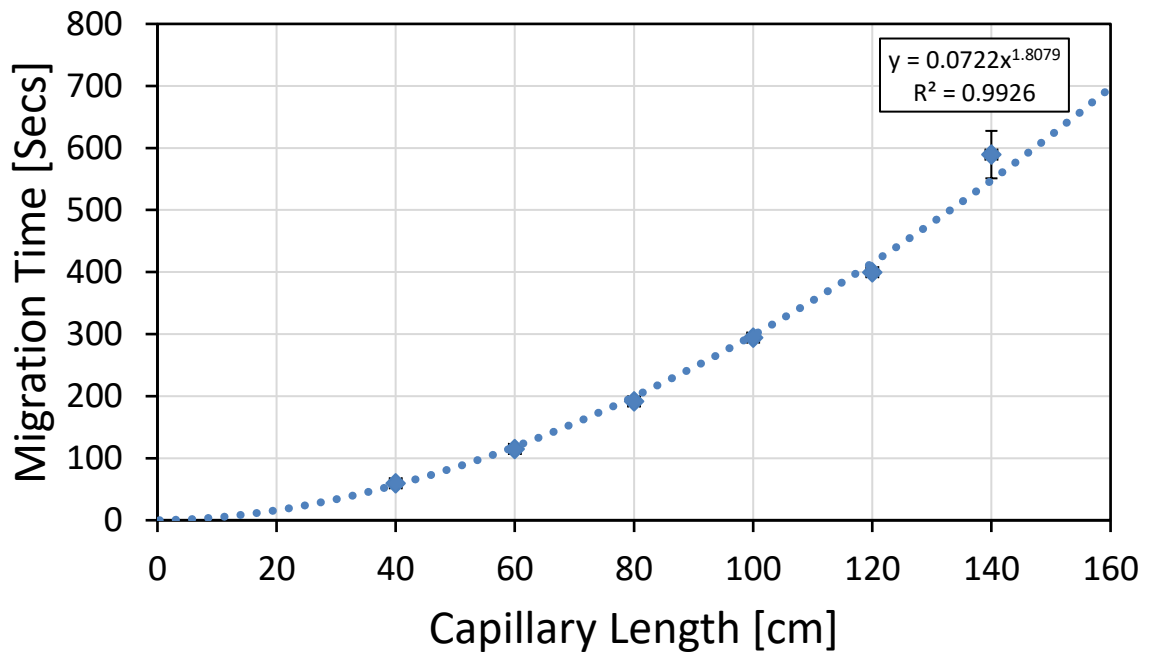


Support Figure 4.4: The insulated cabinet housing the VdG generator. a) Shows the VdG situated in the cabinet. Dry air is flushed in from the top left corner, causing minor over pressure. The inside of the cabinet is painted with a water-resistant polymer paint to reduce the humidity within the cabinet. All internal faces of the cabinet are insulated with foam. b) A humidity and temperature sensor were placed in the box, ensuring that experiments were only performed when the internal humidity was below 20 %. The second amp meter measuring the current drawn by the VdG or outputted 30 kV power supply. c) The first buffer well in the holder. During operation, the holder would be pulled back and flush with the cut hole. Copper wire extends to 5 mm from the surface of the VdG dome. d) The field meter sensor was on the opposing wall (with regards to the buffer well) to avoid discharge to the meter. The holder was 3D printed as well.

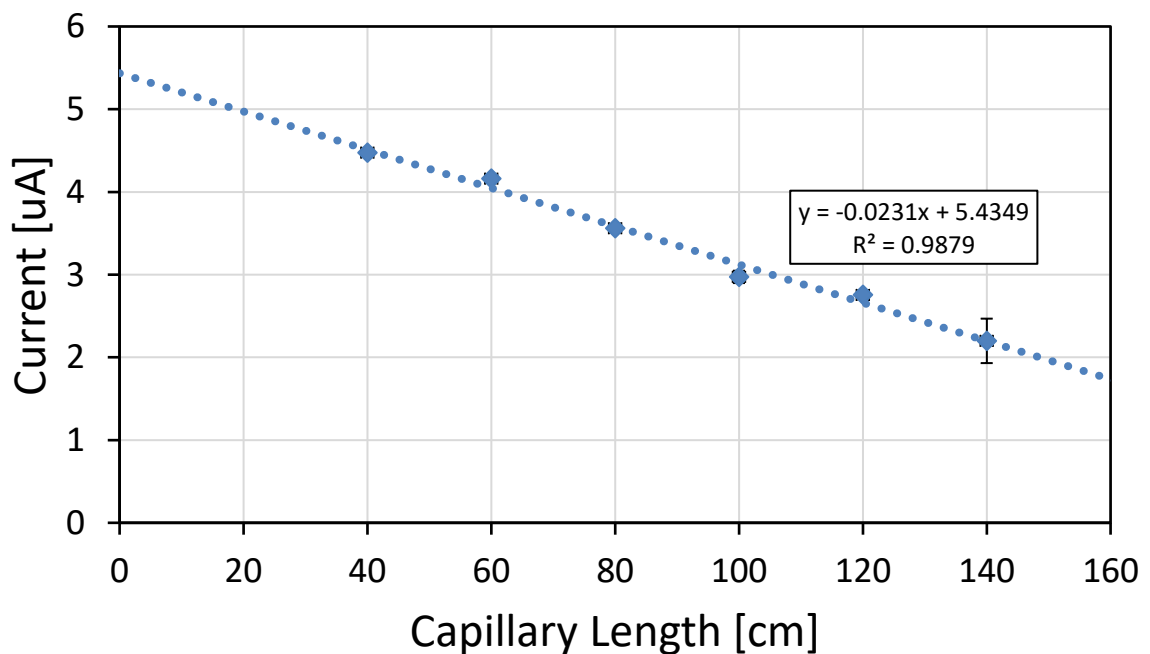
## 5.2 Additional experimental data



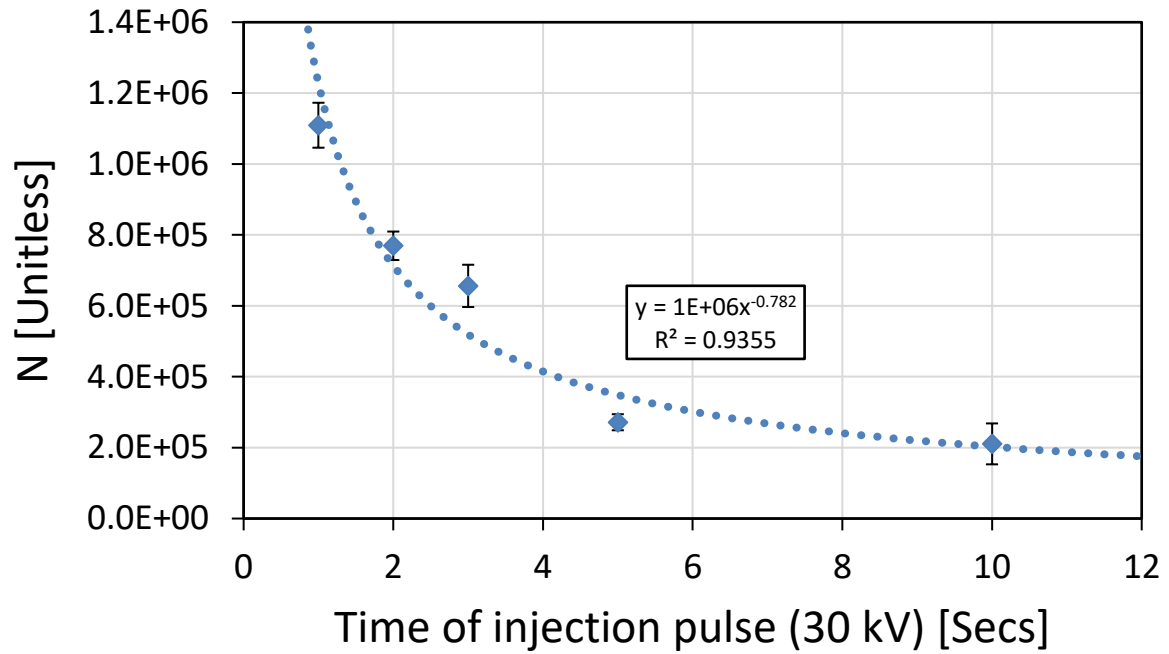
Support Figure 4.5: Field measurements of the capillary exposed to the Van de Graaff generator field. Measurements were at different positions along the capillary. Electric field strength followed the expected inversely related to square of the distance from the source.



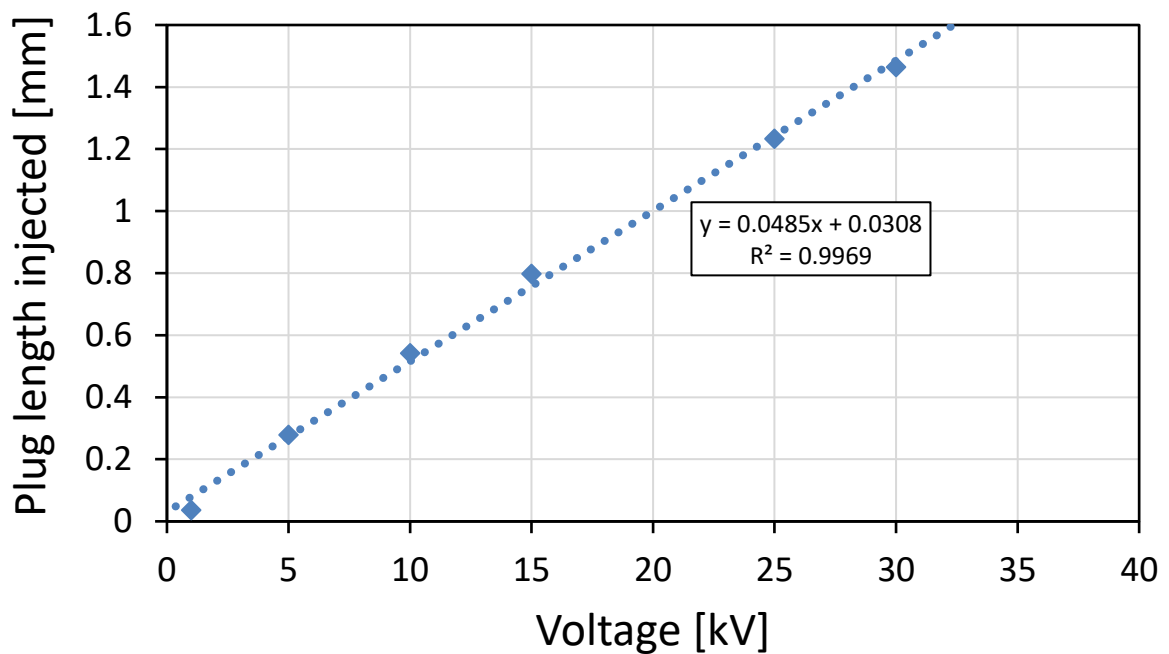
Support Figure 4.6: The time of migration for F in a capillary of varying lengths exposed to the electric field generated by the VdG generator. Migration time has a non-linear relationship between the capillary length and the migration time, in agreement with the electric field relationship. Shorter capillary means a stronger electric field and the faster the migration time.



Support Figure 4.7: VdG generator current observed on the ground side of the capillary as a function of capillary length. Current increases as the length of a resistor decreases to maintain constant voltage, showing the capillary acts as a regular resistor.



Support Figure 4.8: Plate number as a function of time for the injection pulse (30 kV) was applied followed by a separation voltage of 30 kV. The lower the time of the pulse, the thinner the injected plug hence the higher the resultant plate number.



Support Figure 4.9: Plug injection length as a function of a 1 second pulse of a given voltage using the power supply.

## Bibliography

1. Kaplan, F. M. 1959: *The Year Everything Changed*. (Wiley, 2010).
2. Saxena, A. N. *Invention of integrated circuits: untold important facts*. (World Scientific, 2009).
3. Terry, S. C., Herman, J. H. & Angell, J. B. A Gas Chromatographic Air Analyzer Fabricated on a Silicon Wafer. *IEEE Trans. Electron Devices* **26**, 1880–1886 (1979).
4. Voeten, R. L. C., Ventouri, I. K., Haselberg, R. & Somsen, G. W. Capillary Electrophoresis: Trends and Recent Advances. *Anal. Chem.* **90**, 1464–1481 (2018).
5. Ediriweera, M. K., Tennekoon, K. H. & Samarakoon, S. R. In vitro assays and techniques utilized in anticancer drug discovery. *J. Appl. Toxicol.* **39**, 38–71 (2019).
6. Pousti, M., Zarabadi, M. P., Abbaszadeh Amirdehi, M., Paquet-Mercier, F. & Greener, J. Microfluidic bioanalytical flow cells for biofilm studies: a review. *Analyst* **144**, 68–86 (2019).
7. Ahrberg, C. D., Manz, A. & Chung, B. G. Polymerase chain reaction in microfluidic devices. *Lab Chip* **16**, 3866–3884 (2016).
8. Hegab, H. M., ElMekawy, A. & Stakenborg, T. Review of microfluidic microreactor technology for high-throughput submerged microbiological cultivation. *Biomicrofluidics* **7**, (2013).
9. Manz, A., Neuzil, P., O'Connor, J. S. & Simone, G. *Microfluidics and Lab-on-a-chip*. (The Royal Society of Chemistry, 2020).
10. Suh, Y. K. & Kang, S. A review on mixing in microfluidics. *Micromachines* **1**, 82–111 (2010).
11. Alsaeed, B. & Mansour, F. R. Distance-based paper microfluidics; principle, technical aspects and applications. *Microchem. J.* **155**, 104664 (2020).
12. Zhu, Y. & Fang, Q. Analytical detection techniques for droplet microfluidics-A review. *Anal. Chim. Acta* **787**, 24–35 (2013).
13. Grand View Research. Microfluidics Market Size, Share & Trends Analysis Report By Technology (Medical, Non-medical), By Application (Lab-on-a-chip, Organs-on-chips), By Material (Polymer, Silicon, Glass, PDMS), By Region, And Segment Forecasts, 2021 - 2028. *Microfluidics Market Size | Industry Report, 2021-2028* 10 <https://www.unilibrary.org/content/books/9789290687696c002> (2019).
14. Hoskins, W. M. & Craig, R. Uses of bioassay in entomology. *Annu. Rev. Entomol.* **7**, 437–464 (1962).
15. Finney, D. J. *Probit analysis: A statistical treatment of the sigmoid response curve, 2nd ed. Probit analysis: A statistical treatment of the sigmoid response curve, 2nd ed.* (Cambridge University Press, 1952).
16. Adenubi, O. T., McGaw, L. J., Eloff, J. N. & Naidoo, V. In vitro bioassays used in evaluating plant extracts for tick repellent and acaricidal properties: A critical review. *Vet. Parasitol.* **254**, 160–171 (2018).
17. Koenig, R. Indirect ELISA methods for the broad specificity detection of plant viruses. *J. Gen. Virol.* **55**, 53–62 (1981).
18. Dutka, F., Opalski, A. S. & Garstecki, P. Nano-liter droplet libraries from a pipette: Step emulsificator that stabilizes droplet volume against variation in flow rate. *Lab Chip* **16**, 2044–2049 (2016).
19. Kim, D. H., Park, C. G. & Kim, Y. J. Characterizing the potential estrogenic and androgenic activities of two disinfection byproducts, mono-haloacetic acids and haloacetamides, using in vitro bioassays. *Chemosphere* **242**, 125198 (2020).
20. Haarbarger, D. & Pillay, T. S. Historical perspectives in diagnostic clinical pathology: Development of the pregnancy test. *J. Clin. Pathol.* **64**, 546–548 (2011).
21. Johnson, J. E. Use of a commercial ELISA test for the diagnosis of infection by the AIDS virus, HIV, in a patient population. *Diagn. Microbiol. Infect. Dis.* **6**, 267–271 (1987).
22. Wu, J. L. *et al.* Four point-of-care lateral flow immunoassays for diagnosis of COVID-19 and for assessing dynamics of antibody responses to SARS-CoV-2. *J. Infect.* **81**, 435–442 (2020).

23. Breslin, S. & O'Driscoll, L. Three-dimensional cell culture: The missing link in drug discovery. *Drug Discov. Today* **18**, 240–249 (2013).
24. Combs, C. A. Fluorescence Microscopy: A Concise Guide to Current Imaging Methods. *Curr. Protoc. Neurosci.* **50**, 1–14 (2010).
25. Schneider, G. Automating drug discovery. *Nat. Rev. Drug Discov.* **17**, (2018).
26. Baker, B. M. & Chen, C. S. Deconstructing the third dimension-how 3D culture microenvironments alter cellular cues. *J. Cell Sci.* **125**, 3015–3024 (2012).
27. Pampaloni, F., Reynaud, E. G. & Stelzer, E. H. K. Air-liquid interface Growth medium Apoptosis/anoikis Aggregation Polarization Differentiation. *Nat. Rev. Mol. Cell Biol.* **8**, 839–845 (2007).
28. MJ, B., Aylin, R. & I Saira, M. Tissue architecture: the ultimate regulator of breast epithelial function. *Curr. Opin. Cell Biol.* **15**, 753–762 (2003).
29. Kilian, K. A., Bugarija, B., Lahn, B. T. & Mrksich, M. Geometric cues for directing the differentiation of mesenchymal stem cells. *Proc. Natl. Acad. Sci. U. S. A.* **107**, 4872–4877 (2010).
30. Griffith, L. G. & Swartz, M. A. Capturing complex 3D tissue physiology in vitro. *Nat. Rev. Mol. Cell Biol.* **7**, 211–224 (2006).
31. Frieboes, H. B. *et al.* An integrated computational/experimental model of tumor invasion. *Cancer Res.* **66**, 1597–1604 (2006).
32. Gómez-Lechón, M. J. *et al.* Long-term expression of differentiated functions in hepatocytes cultured in three-dimensional collagen matrix. *J. Cell. Physiol.* **177**, 553–562 (1998).
33. Marushima, H. *et al.* Three-dimensional culture promotes reconstitution of the tumor-specific hypoxic microenvironment under TGF $\beta$  stimulation. *Int. J. Oncol.* **39**, 1327–1336 (2011).
34. Aggarwal, B. B., Danda, D., Gupta, S. & Gehlot, P. Models for prevention and treatment of cancer: Problems vs promises. *Biochem. Pharmacol.* **78**, 1083–1094 (2009).
35. Khetan, S. & Burdick, J. A. Patterning network structure to spatially control cellular remodeling and stem cell fate within 3-dimensional hydrogels. *Biomaterials* **31**, 8228–8234 (2010).
36. Hickman, J. A. *et al.* Three-dimensional models of cancer for pharmacology and cancer cell biology: Capturing tumor complexity in vitro/ex vivo. *Biotechnol. J.* **9**, 1115–1128 (2014).
37. Sodunke, T. R. *et al.* Micropatterns of Matrigel for three-dimensional epithelial cultures. *Biomaterials* **28**, 4006–4016 (2007).
38. Ort, C., Chen, Y., Ghagre, A., Ehrlicher, A. & Moraes, C. Bioprintable, Stiffness-Tunable Collagen-Alginate Microgels for Increased Throughput 3D Cell Culture Studies. *ACS Biomater. Sci. Eng.* **7**, 2814–2822 (2021).
39. Nandi, S. *et al.* Platelet-like particles improve fibrin network properties in a hemophilic model of provisional matrix structural defects. *J. Colloid Interface Sci.* **577**, 406–418 (2020).
40. Schindler, M. *et al.* Agarose microgel culture delineates lumenogenesis in naive and primed human pluripotent stem cells. *Stem Cell Reports* **16**, 1347–1362 (2021).
41. Yuan, H. *et al.* Hand-Powered Microfluidics for Parallel Droplet Digital Loop-Mediated Isothermal Amplification Assays. *ACS Sensors* (2021) doi:10.1021/acssensors.1c00184.
42. Piras, C. C., Kay, A. G., Genever, P. G. & Smith, D. K. Self-assembled low-molecular-weight gelator injectable microgel beads for delivery of bioactive agents. *Chem. Sci.* **12**, 3958–3965 (2021).
43. Lum, Z., Krestow, M., Tai, I. T., Vacek, I. & Sun, A. M. Xenografts of rat islets into diabetic mice. *Transplantation* **53**, 1180–1183 (1992).
44. Sarker, B. *et al.* Oxidized Alginate-Gelatin Hydrogel: A Favorable Matrix for Growth and Osteogenic Differentiation of Adipose-Derived Stem Cells in 3D. *ACS Biomater. Sci. Eng.* **3**, 1730–1737 (2017).
45. Karoubi, G., Ormiston, M. L., Stewart, D. J. & Courtman, D. W. Single-cell hydrogel

- encapsulation for enhanced survival of human marrow stromal cells. *Biomaterials* **30**, 5445–5455 (2009).
46. Young, S., Wong, M., Tabata, Y. & Mikos, A. G. Gelatin as a delivery vehicle for the controlled release of bioactive molecules. *J. Control. Release* **109**, 256–274 (2005).
  47. Kawai, K., Suzuki, S., Tabata, Y., Ikada, Y. & Nishimura, Y. Accelerated tissue regeneration through incorporation of basic fibroblast growth factor-impregnated gelatin microspheres into artificial dermis. *Biomaterials* **21**, 489–499 (2000).
  48. Yao, C. H., Liu, B. S., Hsu, S. H., Chen, Y. S. & Tsai, C. C. Biocompatibility and biodegradation of a bone composite containing tricalcium phosphate and genipin crosslinked gelatin. *J. Biomed. Mater. Res. - Part A* **69**, 709–717 (2004).
  49. Suvarnapathaki, S. *et al.* Generation of cell-laden hydrogel microspheres using 3D printing-enabled microfluidics. *J. Mater. Res.* **33**, 2012–2018 (2018).
  50. Kerscher, P. *et al.* Direct Production of Human Cardiac Tissues by Pluripotent Stem Cell Encapsulation in Gelatin Methacryloyl. *ACS Biomater. Sci. Eng.* **3**, 1499–1509 (2017).
  51. Chawla, D., Kaur, T., Joshi, A. & Singh, N. 3D bioprinted alginate-gelatin based scaffolds for soft tissue engineering. *Int. J. Biol. Macromol.* **144**, 560–567 (2020).
  52. Hasturk, O., Jordan, K. E., Choi, J. & Kaplan, D. L. Enzymatically crosslinked silk and silk-gelatin hydrogels with tunable gelation kinetics, mechanical properties and bioactivity for cell culture and encapsulation. *Biomaterials* **232**, 119720 (2020).
  53. Yoo, K. M., Murphy, S. V. & Skardal, A. A rapid crosslinkable maleimide-modified hyaluronic regenerative applications. *Gels* **7**, (2021).
  54. Goto, R. *et al.* Gelatin Methacryloyl – Riboflavin ( GelMA – RF ) Hydrogels for Bone Regeneration. (2021).
  55. Xu, Y. *et al.* Liquid–Liquid Phase-Separated Systems from Reversible Gel–Sol Transition of Protein Microgels. *Adv. Mater.* **33**, (2021).
  56. Osorio, F. A., Bilbao, E., Bustos, R. & Alvarez, F. Effects of concentration, bloom degree, and pH on gelatin melting and gelling temperatures using small amplitude oscillatory rheology. *Int. J. Food Prop.* **10**, 841–851 (2007).
  57. Lieben, F. On the Hydrolysis of Proteins and Peptones at High Temperatures and on the Catalytic Effect of Metal Ions on the Rate of Hydrolysis. *J. Biol. Chem.* **151**, 117–121 (1943).
  58. De France, K. J., D’Emilio, E., Cranston, E. D., Geiger, T. & Nyström, G. Dual physically and chemically crosslinked regenerated cellulose – Gelatin composite hydrogels towards art restoration. *Carbohydr. Polym.* **234**, (2020).
  59. Yang, G. *et al.* Assessment of the characteristics and biocompatibility of gelatin sponge scaffolds prepared by various crosslinking methods. *Sci. Rep.* **8**, 1–13 (2018).
  60. Isaschar-Ovdat, S. & Fishman, A. Crosslinking of food proteins mediated by oxidative enzymes – A review. *Trends Food Sci. Technol.* **72**, 134–143 (2018).
  61. Bigi, A., Cojazzi, G., Panzavolta, S., Roveri, N. & Rubini, K. Stabilization of gelatin films by crosslinking with genipin. *Biomaterials* **23**, 4827–4832 (2002).
  62. Sung, B., Krieger, J., Yu, B. & Kim, M. H. Colloidal gelatin microgels with tunable elasticity support the viability and differentiation of mesenchymal stem cells under pro-inflammatory conditions. *J. Biomed. Mater. Res. - Part A* **106**, 2753–2761 (2018).
  63. Sugiura, S. *et al.* Size control of calcium alginate beads containing living cells using micro-nozzle array. *Biomaterials* **26**, 3327–3331 (2005).
  64. Mora-Boza, A. *et al.* Microfluidics generation of chitosan microgels containing glycerylphytate crosslinker for in situ human mesenchymal stem cells encapsulation. *Mater. Sci. Eng. C* **120**, 111716 (2021).
  65. Kim, S., Oh, J. & Cha, C. Enhancing the biocompatibility of microfluidics-assisted fabrication of cell-laden microgels with channel geometry. *Colloids Surfaces B Biointerfaces* **147**, 1–8 (2016).
  66. Guerzoni, L. P. B. *et al.* Cell Encapsulation in Soft, Anisometric Poly(ethylene) Glycol

- Microgels Using a Novel Radical-Free Microfluidic System. *Small* **15**, 1–8 (2019).
67. Samandari, M., Alipanah, F., Haghjooy Javanmard, S. & Sanati-Nezhad, A. One-step wettability patterning of PDMS microchannels for generation of monodisperse alginate microbeads by in Situ external gelation in double emulsion microdroplets. *Sensors Actuators, B Chem.* **291**, 418–425 (2019).
  68. Vladislavljević, G. T., Kobayashi, I. & Nakajima, M. Production of uniform droplets using membrane, microchannel and microfluidic emulsification devices. *Microfluid. Nanofluidics* **13**, 151–178 (2012).
  69. Wang, S. *et al.* High-Throughput Functional Screening of Antigen-Specific T Cells Based on Droplet Microfluidics at a Single-Cell Level. *Anal. Chem.* (2021) doi:10.1021/acs.analchem.1c03678.
  70. Klaus, M. *et al.* Ultrahigh-Throughput Detection of Enzymatic Alcohol Dehydrogenase Activity in Microfluidic Droplets with a Direct Fluorogenic Assay. *ChemBioChem* **22**, 3292–3299 (2021).
  71. Farahat, W. A. *et al.* Ensemble analysis of angiogenic growth in three-dimensional microfluidic cell cultures. *PLoS One* **7**, (2012).
  72. Brouzes, E. *et al.* Droplet microfluidic technology for single-cell high-throughput screening. *Proc. Natl. Acad. Sci. U. S. A.* **106**, 14195–14200 (2009).
  73. Vaithiyanathan, M. *et al.* Luminescent nanomaterials for droplet tracking in a microfluidic trapping array. *Anal. Bioanal. Chem.* **411**, 157–170 (2019).
  74. Nestor, B. A. *et al.* Digital microfluidic platform for dielectrophoretic patterning of cells encapsulated in hydrogel droplets. *RSC Adv.* **6**, 57409–57416 (2016).
  75. Shi, Y. *et al.* High throughput generation and trapping of individual agarose microgel using microfluidic approach. *Microfluid. Nanofluidics* **15**, 467–474 (2013).
  76. Lin, C. H., Lee, G. Bin, Lin, Y. H. & Chang, G. L. A fast prototyping process for fabrication of microfluidic systems on soda-lime glass. *J. Micromechanics Microengineering* **11**, 726–732 (2001).
  77. Yuen, P. K. & Goral, V. N. Low-Cost Rapid Prototyping of Whole-Glass Microfluidic Devices. (2012).
  78. Kotz, F. *et al.* Rapid prototyping of glass microfluidic chips. *Microfluid. BioMEMS, Med. Microsystems XIII* **9320**, 932003 (2015).
  79. Walsh, D. I., Kong, D. S., Murthy, S. K. & Carr, P. A. Enabling Microfluidics: from Clean Rooms to Makerspaces. *Trends Biotechnol.* **35**, 383–392 (2017).
  80. Faustino, V., Catarino, S. O., Lima, R. & Minas, G. Biomedical microfluidic devices by using low-cost fabrication techniques: A review. *J. Biomech.* **49**, 2280–2292 (2016).
  81. Dewanda, F., Ahsan, M. S. & Lee, M. S. Fabrication of micro/nano-fluidic channels by single-beam direct femtosecond laser writing. *Microfluid. BioMEMS, Med. Microsystems XI* **8615**, 86150H (2013).
  82. McDonald, J. C. *et al.* Prototyping of microfluidic devices in poly(dimethylsiloxane) using solid-object printing. *Anal. Chem.* **74**, 1537–1545 (2002).
  83. Felton, H., Hughes, R. & Diaz-Gaxiola, A. Negligible-cost microfluidic device fabrication using 3D-printed interconnecting channel scaffolds. *PLoS One* **16**, 1–22 (2021).
  84. Sun, M., Xie, Y., Zhu, J., Li, J. & Eijkel, J. C. T. Improving the Resolution of 3D-Printed Molds for Microfluidics by Iterative Casting-Shrinkage Cycles. *Anal. Chem.* **89**, 2227–2231 (2017).
  85. Zhu, F. *et al.* Three-dimensional printed millifluidic devices for zebrafish embryo tests. *Biomicrofluidics* **9**, (2015).
  86. Kamei, K. ichiro *et al.* 3D printing of soft lithography mold for rapid production of polydimethylsiloxane-based microfluidic devices for cell stimulation with concentration gradients. *Biomed. Microdevices* **17**, (2015).
  87. Colin, V. G., Travers, T., Gindre, D., Barillé, R. & Loumaigne, M. Cheap, versatile, and turnkey fabrication of microfluidic master molds using consumer-grade LCD stereolithography 3D

- printing. *Int. J. Adv. Manuf. Technol.* **116**, 537–544 (2021).
88. Tovar, M. *et al.* 3D-glass molds for facile production of complex droplet microfluidic chips. *Biomicrofluidics* **12**, (2018).
  89. Venzac, B. *et al.* PDMS Curing Inhibition on 3D-Printed Molds: Why? Also, How to Avoid It? *Anal. Chem.* **93**, 7180–7187 (2021).
  90. Zhu, P. & Wang, L. Passive and active droplet generation with microfluidics: a review. *Lab Chip* **17**, 34–75 (2017).
  91. Toor, A., Lamb, S., Helms, B. A. & Russell, T. P. Reconfigurable Microfluidic Droplets Stabilized by Nanoparticle Surfactants. *ACS Nano* **12**, 2365–2372 (2018).
  92. Trantidou, T., Elani, Y., Parsons, E. & Ces, O. Hydrophilic surface modification of pdms for droplet microfluidics using a simple, quick, and robust method via pva deposition. *Microsystems Nanoeng.* **3**, (2017).
  93. Hering, I. *et al.* Evaluation of potential environmental toxicity of polymeric nanomaterials and surfactants. *Environ. Toxicol. Pharmacol.* **76**, 103353 (2020).
  94. Johnson, P., Trybala, A., Starov, V. & Pinfield, V. J. Effect of synthetic surfactants on the environment and the potential for substitution by biosurfactants. *Adv. Colloid Interface Sci.* **288**, 102340 (2021).
  95. Bhattacharya, R., Chatterjee, A., Chatterjee, S. & Saha, N. C. Acute toxicity and impact of sublethal exposure to commonly used surfactants sodium dodecyl sulphate, cetylpyridinium chloride and sodium laureth sulphate on oxidative stress enzymes in oligochaete worm *Branchiura sowerbyi* (Beddard, 1892). *Aquac. Res.* **52**, 6367–6379 (2021).
  96. Niu, X., Gulati, S., Edel, J. B. & Demello, A. J. Pillar-induced droplet merging in microfluidic circuits. *Lab Chip* **8**, 1837–1841 (2008).
  97. Nakagawa, K., Iwamoto, S., Nakajima, M., Shono, A. & Satoh, K. Microchannel emulsification using gelatin and surfactant-free coacervate microencapsulation. *J. Colloid Interface Sci.* **278**, 198–205 (2004).
  98. Liu, M., Sun, X. T., Yang, C. G. & Xu, Z. R. On-chip preparation of calcium alginate particles based on droplet templates formed by using a centrifugal microfluidic technique. *J. Colloid Interface Sci.* **466**, 20–27 (2016).
  99. Nguyen, N. T. *et al.* Thermally mediated droplet formation in microchannels. *Appl. Phys. Lett.* **91**, 89–92 (2007).
  100. Stan, C. A., Tang, S. K. Y. & Whitesides, G. M. Independent control of drop size and velocity in microfluidic flow-focusing generators using variable temperature and flow rate. *Anal. Chem.* **81**, 2399–2402 (2009).
  101. Parmar, I. A., Shedge, A. S., Badiger, M. V., Wadgaonkar, P. P. & Lele, A. K. Thermo-reversible sol-gel transition of aqueous solutions of patchy polymers. *RSC Adv.* **7**, 5101–5110 (2017).
  102. Shinoda, K. & Saito, H. The effect of temperature on the phase equilibria and the types of dispersions of the ternary system composed of water, cyclohexane, and nonionic surfactant. *J. Colloid Interface Sci.* **26**, 70–74 (1968).
  103. Fujii, K. B., Kobayashi, I., Uemura, K. & Nakajima, M. Temperature effect on microchannel oil-in-water emulsification. *Microfluid. Nanofluidics* **10**, 773–783 (2011).
  104. Cui, W., Yesiloz, G. & Ren, C. L. Microwave heating induced on-demand droplet generation in microfluidic systems. *Anal. Chem.* **93**, 1266–1270 (2021).
  105. Khater, A., Mohammadi, M., Mohamad, A. & Nezhad, A. S. Dynamics of temperature-actuated droplets within microfluidics. *Sci. Rep.* **9**, 1–11 (2019).
  106. Apushkinskaya, N. Mikrofluidische Herstellung von Gelatine-Mikrogelen für die Mikroverkapselung von probiotischen Bakterien: Physiochemische Eigenschaften und ihr Einfluss auf die biologische Stabilität. (Fulda University of Applied Sciences, Germany, 2022).

107. Gwag, E., Abelman, L., Manz, A. & Sung, B. Tissue-mimicking Gelatin Microgels Implement 3D In Vitro Nanotoxicity Screening. in *31st Annual Conference of the European Society of Biomaterials (Virtual)*.
108. Wagner, S. *et al.* Novel Strategies for the Treatment of *Pseudomonas aeruginosa* Infections. *J. Med. Chem.* **59**, 5929–5969 (2016).
109. Govan, J. R. & Deretic, V. Microbial pathogenesis in cystic fibrosis: mucoid *Pseudomonas aeruginosa* and *Burkholderia cepacia*. *Microbiol. Rev.* **60**, 539–574 (1996).
110. Finch, R. G. *Antibiotic & chemotherapy*. (Elsevier, 2010).
111. Olivares, E. *et al.* Clinical Impact of Antibiotics for the Treatment of *Pseudomonas aeruginosa* Biofilm Infections. *Front. Microbiol.* **10**, 1–12 (2020).
112. Dos Santos Ramos, M. A. *et al.* Nanotechnology-based drug delivery systems for control of microbial biofilms: A review. *Int. J. Nanomedicine* **13**, 1179–1213 (2018).
113. Bharali, D. J. *et al.* Nanoparticle delivery of natural products in the prevention and treatment of cancers: Current status and future prospects. *Cancers (Basel)*. **3**, 4024–4045 (2011).
114. Tomlinson, E. Theory and practice of site-specific drug delivery. *Adv. Drug Deliv. Rev.* **1**, 87–198 (1987).
115. Khosa, A., Reddi, S. & Saha, R. N. Nanostructured lipid carriers for site-specific drug delivery. *Biomed. Pharmacother.* **103**, 598–613 (2018).
116. Yeh, Y. C., Huang, T. H., Yang, S. C., Chen, C. C. & Fang, J. Y. Nano-Based Drug Delivery or Targeting to Eradicate Bacteria for Infection Mitigation: A Review of Recent Advances. *Front. Chem.* **8**, 1–22 (2020).
117. Lee, S. H., Sato, Y., Hyodo, M. & Harashima, H. Topology of surface ligands on liposomes: Characterization based on the terms, incorporation ratio, surface anchor density, and reaction yield. *Biol. Pharm. Bull.* **39**, 1983–1994 (2016).
118. Diggle, S. P. *et al.* The galactophilic lectin, LecA, contributes to biofilm development in *Pseudomonas aeruginosa*. *Environ. Microbiol.* **8**, 1095–1104 (2006).
119. Lepenies, B., Lee, J. & Sonkaria, S. Targeting C-type lectin receptors with multivalent carbohydrate ligands. *Adv. Drug Deliv. Rev.* **65**, 1271–1281 (2013).
120. Busold, S. *et al.* Various Tastes of Sugar: The Potential of Glycosylation in Targeting and Modulating Human Immunity via C-Type Lectin Receptors. *Front. Immunol.* **11**, 1–12 (2020).
121. de Oliveira Figueiroa, E. *et al.* Lectin-Carbohydrate Interactions: Implications for the Development of New Anticancer Agents. *Curr. Med. Chem.* **24**, 3667–3680 (2017).
122. Cecioni, S., Imbert, A. & Vidal, S. Glycomimetics versus multivalent glycoconjugates for the design of high affinity lectin ligands. *Chem. Rev.* **115**, 525–561 (2015).
123. Meyer, M. T., Roy, V., Bentley, W. E. & Ghodssi, R. Development and validation of a microfluidic reactor for biofilm monitoring via optical methods. *J. Micromechanics Microengineering* **21**, (2011).
124. Thomas, A. *et al.* Characterization of vascular permeability using a biomimetic microfluidic blood vessel model. *Biomicrofluidics* **11**, 1–17 (2017).
125. Ejiugwo, M., Rochev, Y., Gethin, G. & O'Connor, G. Toward Developing Immunocompetent Diabetic Foot Ulcer-on-a-Chip Models for Drug Testing. *Tissue Eng. Part C Methods* **27**, 77–88 (2021).
126. Helps, E. P. W. & McDonald, D. A. Observations on laminar flow in veins. *J. Physiol.* **124**, 631–639 (1954).
127. Klarhöfer, M., Csapo, B., Balassy, C., Szeles, J. C. & Moser, E. High-resolution blood flow velocity measurements in the human finger. *Magn. Reson. Med.* **45**, 716–719 (2001).
128. Majhy, B., Priyadarshini, P. & Sen, A. K. Effect of surface energy and roughness on cell adhesion and growth-facile surface modification for enhanced cell culture. *RSC Adv.* **11**, 15467–15476 (2021).

129. Dominical, V. M. *et al.* In vitro microfluidic model for the study of vaso-occlusive processes. *Exp. Hematol.* **43**, 223–228 (2015).
130. Kim, J. *et al.* Hydrodynamic effects on bacterial biofilm development in a microfluidic environment. *Lab Chip* **13**, 1846–1849 (2013).
131. Liu, Y. & Tay, J.-H. The essential role of hydrodynamic shear force in the formation of biofilm and granular sludge. *Water Res.* **36**, 1653–1665 (2002).
132. Stoodley, P., Wefel, J., Gieseke, A. & Ohle, C. Von. mass transfer , fluoride delivery and caries ABSTRACT. *Crit. Rev.* (2010).
133. Brito, A. G. & Melo, L. F. Mass transfer coefficients within anaerobic biofilms: Effects of external liquid velocity. *Water Res.* **33**, 3673–3678 (1999).
134. De Beer, D., Stoodley, P. & Lewandowski, Z. Liquid flow and mass transport in heterogeneous biofilms. *Water Res.* **30**, 2761–2765 (1996).
135. Zhang, X., Lu, H., Qian, M. & Zeng, X. Fabrication of microfluidic devices using photopatternable hybrid sol-gel coatings. *J. Sol-Gel Sci. Technol.* **48**, 143–147 (2008).
136. Kim, B. Y., Hong, L. Y., Chung, Y. M., Kim, D. P. & Lee, C. S. Solvent-resistant PDMS microfluidic devices with hybrid inorganic/organic polymer coatings. *Adv. Funct. Mater.* **19**, 3796–3803 (2009).
137. Sun, D. & Böhringer, K. F. Self-cleaning: From bio-inspired surface modification to MEMS/microfluidics system integration. *Micromachines* **10**, (2019).
138. Annabi, N. *et al.* Hydrogel-coated microfluidic channels for cardiomyocyte culture. *Lab Chip* **13**, 3569–3577 (2013).
139. Pitingolo, G., Riaud, A., Nastruzzi, C. & Taly, V. Gelatin-coated microfluidic channels for 3D microtissue formation: On-chip production and characterization. *Micromachines* **10**, (2019).
140. Allcock, H. R., Phelps, M. V. B., Barrett, E. W., Pishko, M. V. & Koh, W. G. Ultraviolet photolithographic development of polyphosphazene hydrogel microstructures for potential use in microarray biosensors. *Chem. Mater.* **18**, 609–613 (2006).
141. Ayala, P., Lopez, J. I. & Desai, T. A. Microtopographical cues in 3D attenuate fibrotic phenotype and extracellular matrix deposition: Implications for tissue regeneration. *Tissue Eng. - Part A* **16**, 2519–2527 (2010).
142. Revzin, A. *et al.* Fabrication of poly(ethylene glycol) hydrogel microstructures using photolithography. *Langmuir* **17**, 5440–5447 (2001).
143. Chou, W. L., Lee, P. Y., Yang, C. L., Huang, W. Y. & Lin, Y. S. Recent advances in applications of droplet microfluidics. *Micromachines* **6**, 1249–1271 (2015).
144. Neethirajan, S. *et al.* Microfluidics for food, agriculture and biosystems industries. *Lab Chip* **11**, 1574–1586 (2011).
145. Neumann, W. P., Winkel, J., Medbo, L., Magneberg, R. & Mathiassen, S. E. Production system design elements influencing productivity and ergonomics: A case study of parallel and serial flow strategies. *Int. J. Oper. Prod. Manag.* **26**, 904–923 (2006).
146. Jeon, J. *et al.* SERS-based droplet microfluidics for high-throughput gradient analysis. *Lab Chip* **19**, 674–681 (2019).
147. Rho, H. S. *et al.* Programmable droplet-based microfluidic serial dilutor. *J. Ind. Eng. Chem.* **91**, 231–239 (2020).
148. Ménétrier-Deremble, L. & Tabeling, P. Droplet breakup in microfluidic junctions of arbitrary angles. *Phys. Rev. E - Stat. Nonlinear, Soft Matter Phys.* **74**, 1–4 (2006).
149. Li, W. *et al.* Simultaneous generation of droplets with different dimensions in parallel integrated microfluidic droplet generators. *Soft Matter* **4**, 258 (2008).
150. Mulligan, M. K. & Rothstein, J. P. Scale-up and control of droplet production in coupled microfluidic flow-focusing geometries. *Microfluid. Nanofluidics* **13**, 65–73 (2012).
151. Tetradis-Meris, G. *et al.* Novel parallel integration of microfluidic device network for emulsion formation. *Ind. Eng. Chem. Res.* **48**, 8881–8889 (2009).

152. Nakashima, T., Shimizu, M. & Kukizaki, M. Membrane emulsification by microporous glass. *Inorg. Membr. ICIM2-91* 513–516 (1991) doi:10.4028/www.scientific.net/kem.61-62.513.
153. Cheng, J. *et al.* Pore structure design of NFES PTFE membrane for membrane emulsification. *J. Memb. Sci.* **611**, 118365 (2020).
154. El-Hawari, L. & Bunjes, H. Premix membrane emulsification: Preparation and stability of medium-chain triglyceride emulsions with droplet sizes below 100 nm. *Molecules* **26**, (2021).
155. Li, W., Greener, J., Voicu, D. & Kumacheva, E. Multiple modular microfluidic (M3) reactors for the synthesis of polymer particles. *Lab Chip* **9**, 2715–2721 (2009).
156. Kikutani, Y., Ueno, M., Hisamoto, H., Tokeshi, M. & Kitamori, T. Continuous-flow chemical processing in three-dimensional microchannel network for on-chip integration of multiple reactions in a combinatorial mode. *QSAR Comb. Sci.* **24**, 742–757 (2005).
157. Shen, Q. *et al.* Numbering-up strategies of micro-chemical process: Uniformity of distribution of multiphase flow in parallel microchannels. *Chem. Eng. Process. - Process Intensif.* **132**, 148–159 (2018).
158. Han, T., Zhang, L., Xu, H. & Xuan, J. Factory-on-chip: Modularised microfluidic reactors for continuous mass production of functional materials. *Chem. Eng. J.* **326**, 765–773 (2017).
159. Headen, D. M., García, J. R. & García, A. J. Parallel droplet microfluidics for high throughput cell encapsulation and synthetic microgel generation. *Microsystems Nanoeng.* **4**, 1–9 (2018).
160. Morgan, A. J. L. *et al.* Simple and versatile 3D printed microfluidics using fused filament fabrication. *PLoS One* **11**, 1–17 (2016).
161. Duarte, L. C., Chagas, C. L. S., Ribeiro, L. E. B. & Coltro, W. K. T. 3D printing of microfluidic devices with embedded sensing electrodes for generating and measuring the size of microdroplets based on contactless conductivity detection. *Sensors Actuators, B Chem.* **251**, 427–432 (2017).
162. Nelson, M. D., Ramkumar, N. & Gale, B. K. Flexible, transparent, sub-100  $\mu\text{m}$  microfluidic channels with fused deposition modeling 3D-printed thermoplastic polyurethane. *J. Micromechanics Microengineering* **29**, (2019).
163. Bressan, L. P., Adamo, C. B., Quero, R. F., de Jesus, D. P. & da Silva, J. A. F. A simple procedure to produce FDM-based 3D-printed microfluidic devices with an integrated PMMA optical window. *Anal. Methods* **11**, 1014–1020 (2019).
164. Lee, J. M., Zhang, M. & Yeong, W. Y. Characterization and evaluation of 3D printed microfluidic chip for cell processing. *Microfluid. Nanofluidics* **20**, 1–15 (2016).
165. Gong, H., Bickham, B. P., Woolley, A. T. & Nordin, G. P. Custom 3D printer and resin for 18  $\mu\text{m}$   $\times$  20  $\mu\text{m}$  microfluidic flow channels. *Lab Chip* **17**, 2899–2909 (2017).
166. Warr, C. A. *et al.* 3D-Printed Microfluidic Droplet Generator With Hydrophilic and Hydrophobic Polymers. *Micromachines* **12**, 1–13 (2021).
167. Bacha, T. W., Manuguerra, D. C., Marano, R. A. & Stanzione, J. F. Hydrophilic modification of SLA 3D printed droplet generators by photochemical grafting. *RSC Adv.* **11**, 21745–21753 (2021).
168. Rusling, J. F. Developing Microfluidic Sensing Devices Using 3D Printing. *ACS Sensors* **3**, 522–526 (2018).
169. Mohamed, M. *et al.* Rapid and Inexpensive Fabrication of Multi-Depth Microfluidic Device using High-Resolution LCD Stereolithographic 3D Printing. *J. Manuf. Mater. Process.* **3**, 26 (2019).
170. Bahrami, M., Yovanovich, M. M. & Culham, J. R. Pressure drop of fully-developed, laminar flow in microchannels of arbitrary cross-section. in *Proceedings of ICMM 2005 3rd International Conference on Microchannels and Minichannels* 12 (2017).
171. Liu, D. *et al.* Assessment of energy requirement for the retinal arterial network in normal and hypertensive subjects. *J. Biomech. Eng.* **134**, 1–8 (2012).

172. Hu, R. *et al.* Microfluidic analysis of pressure drop and flow behavior in hypertensive microvessels. *Biomed. Microdevices* **17**, 1–9 (2015).
173. Tiselius, A. A new apparatus for electrophoretic analysis of colloidal mixtures. *Trans. Faraday Soc.* **33**, 524–531 (1937).
174. Tiselius, A. Electrophoresis of purified antibody preparations. *J. Exp. Med.* **65**, 641–646 (1937).
175. Tiselius, A. Electrophoresis of serum globulin: Electrophoretic analysis of normal and immune sera. *Biochem. J.* **31**, 1464–77 (1937).
176. Tiselius, A. & Kabat, E. A. An Electrophoretic Study of Immune Sera and Purified Antibody Preparations. *J. Exp. Med.* **69**, 119–31 (1939).
177. Swerdlow, H. *et al.* Three DNA sequencing methods using capillary gel electrophoresis and laser-induced fluorescence. *Anal. Chem.* **63**, 2835–41 (1991).
178. Oukacine, F. *et al.* Simultaneous electrokinetic and hydrodynamic injection for high sensitivity bacteria analysis in capillary electrophoresis. *Anal. Chem.* **83**, 4949–4954 (2011).
179. Kuban, P., Pirmohammadi, R. & Karlberg, B. Flow injection analysis-capillary electrophoresis system with hydrodynamic injection. *Anal. Chim. Acta* **378**, 55–62 (1999).
180. Andrus, A. Oligonucleotide analysis by gel capillary electrophoresis. *Methods* **4**, 213–226 (1992).
181. Durney, B. C., Crihfield, C. L. & Holland, L. A. Capillary electrophoresis applied to DNA: determining and harnessing sequence and structure to advance bioanalyses (2009–2014). *Anal. Bioanal. Chem.* **407**, 6923–6938 (2015).
182. Anazawa, T., Takahashi, S. & Kambara, H. A capillary array gel electrophoresis system using multiple laser focusing for DNA sequencing. *Anal. Chem.* **68**, 2699–2704 (1996).
183. Mischak, H. *et al.* Capillary Electrophoresis-mass spectrometry as a powerful tool in biomarker discovery and clinical diagnosis: an update of recent developments. *Mass Spectrom Rev.* **28**, 703–724 (2009).
184. Cai, J., Henion, J., Toxicology, A. & Drive, W. Capillary electrophoresis-mass spectrometry. *J. Chromatogr. A* **703**, 667–692 (1995).
185. Vesterberg, O. A short history of electrophoretic methods. *Electrophoresis* **14**, 1243–1249 (1993).
186. Hjertén, S. Free zone electrophoresis. *Chromatogr. Rev.* **9**, 122–219 (1967).
187. Hjertén, S. High-performance electrophoresis: the electrophoretic counterpart of high-performance liquid chromatography. *J. Chromatogr. A* **270**, 1–6 (1983).
188. Jorgenson, J. W. & Lukacs, K. D. Free-zone electrophoresis in glass capillaries. *Clin. Chem.* **27**, 1551–1553 (1981).
189. Jorgenson, J. W. & Lukacs, K. D. A. High-resolution separations based on electrophoresis and electroosmosis. *J. Chromatogr. A* **218**, 209–216 (1981).
190. Jorgenson, J. W. & Lukacs, K. D. A. Zone Electrophoresis in Open-Tubular Glass Capillaries. *Anal. Chem.* **53**, 1298–1302 (1981).
191. Hutterer, K. M. & Jorgenson, J. W. Ultrahigh-voltage capillary zone electrophoresis. *Anal. Chem.* **71**, 1293–7 (1999).
192. Henley, W. H. & Ramsey, J. M. High electric field strength two-dimensional peptide separations using a microfluidic device. *Electrophoresis* **33**, 2718–2724 (2012).
193. Lukacs, K. D. & Jorgenson, J. W. Capillary zone electrophoresis: Effect of physical parameters on separation efficiency and quantitation. *J. High Resolut. Chromatogr.* **8**, 407–411 (1985).
194. Giddings, J. C. The Theoretical Plate as a Measure of Column Efficiency. *J. Chromatogr. Sci.* **2**, 167–169 (1964).
195. Hjertén, S. Zone broadening in electrophoresis with special reference to high-performance electrophoresis in capillaries: An interplay between theory and practice. *Electrophoresis* **11**, 665–690 (1990).

196. Grushka, E., McCormick, R. M. & Kirkland, J. J. Effect of Temperature Gradients on the Efficiency of Capillary Zone Electrophoresis Separations. *Anal. Chem.* **61**, 241–246 (1989).
197. Evenhuis, C. J., Guijt, R. M., Macka, M., Marriott, P. J. & Haddad, P. R. Temperature profiles and heat dissipation in capillary electrophoresis. *Anal. Chem.* **78**, 2684–2693 (2006).
198. Kashanipour, M. *et al.* Evaluation of the reactivity of vinyl monomers by catalytic thermometric titrimetry. *Anal. Proc.* **23**, 436–454 (1986).
199. Lee, S. J., Castro, E. R., Guijt, R. M., Tarn, M. D. & Manz, A. Van de Graaff generator for capillary electrophoresis. *J. Chromatogr. A* **1517**, 195–202 (2017).
200. Henley, W. H. *et al.* High resolution separations of charge variants and disulfide isomers of monoclonal antibodies and antibody drug conjugates using ultra-high voltage capillary electrophoresis with high electric field strength. *J. Chromatogr. A* **1523**, 72–79 (2017).

## Acknowledgements

Andreas, you have been my supervisor for the past four years and I learnt so much about what it means to be a scientist. I was advised before starting my PhD that choosing the right supervisor was more important than the project, because the project would change anyway. You gave me so much freedom and confidence to investigate my PhD topics in the way I did. You provided so much support and opportunities to discuss my work. We also co-authored a book, something I never thought I would ever have been a part of. It has been a joy to be your student and thank you for a once in a life opportunity.

Leon, thank for the years of support during my PhD. You were always around for a chat about anything, research or otherwise. Some of my favourite memories of KIST were when a bunch of us would go for lunch and have such insightful discussions. You've also tattooed "what is the research question?" on my brain, which will be invaluable to me for the rest of my career. I owe a lot of my growth as a PhD student to you. You are also an incredibly creative individual who I have had the experience to work alongside, and it was all so much fun.

I also had the fortunate opportunity to work with so many people at KIST Europe. Thank you, Nina, and Heesoo. It was an absolute pleasure to share a lab with you both and be a part of your master's studies. I really appreciate having the opportunity to both teach and learn from you. Thank you Baekyoung for bringing the droplet generation topic to the team. I always enjoyed our discussions about travel, food and the UK. Matthias; scientist, chef, cultural and German translator and most importantly, my friend. Thank you for every shared story, beer and random fact about Germany. Sabrina, I could not have done anything at KIST without you. You helped me so so so much, and I am grateful for every little bit of it. Susanne, you were always there with some wise words when I was a bit lost in it all. Jaeho, being a supportive team leader for all of us in the Biosensors team. Jungtae, for sharing your 3D printer with me. Thank you to Eunheui, Carsten, Nuriye, Holger, Rudiger, Daniella, Yu mi, and M.J. for all of your help and chats over the years. Additionally, I'd like to thank Olga, Benedikt and Alex from HIPS, who I had the complete pleasure of collaborating with during my PhD. Also, thank you to Claudia Kemmer of the University PPB team. There were some incredibly difficult times during my PhD, and our appointments really let me understand, gain perspectives and keep my head straight.

I was also fortunate to make a lot of friends during my PhD. Marc. You mad lad. You were a constant source of creativity and free thinking. You introduced me to the breakers in SB, shared a fascination for Hearthstone, beers at Murphy's, fried chicken, travelling and sharing having random stories. Thanks for always being a "productive" distraction and having so many random things to always talk about. Tijmen, an exemplar PhD student and my friend. Early days of sharing the office and watching you write your thesis has helped me a lot through writing mine. Also hiding Pickle Rick on the wall is still the funniest thing I've ever seen, even 4 years later. Whenever we talk it has always spanned so many topics and I appreciated every one of them. We will beat cup head, someday. Galina, you are an incredibly strong and free-spirited person who has always inspired me with the way you could think far beyond the PhD. That this life isn't just about being in the lab, but also about how to enjoy a life outside of it. I look forward to the next beer we can grab in some random jazz bar. Chang Gyun, My longest office mate. Thank you for teaching me some important Korean phrases. Sorry about your table getting a hole burnt in it. I really did

appreciate that birthday grill and think about it every birthday. Loved trading random snacks with you and our chats. Wish you the best for your PhD and what comes after. Felix, without you, I wouldn't have known we even had a 3D printer at KIST Europe. So, I really owe you one for that.

Saarbrücken has been such a special place for me and I will always be grateful to the friends I made here. David, you always made time for a beer and stroll along the Saar. We both got to think and vent a lot. During the peak of the pandemic, you always stayed in touch and made time to check in on me. I appreciate it all. To all the other friends I made here; Samir, Alex, Marcus, Stephanie, Jaideep, Jasmine, Sebastian, Eva and everyone else, thank you for all the good times. Knowing each of you made me my time in SB better and I'll treasure our time always. Also, shout out to all my BBoys and Krumperz at the Jugendzentrum. Always felt better whenever we trained together.

Thank you to all of my beloved friends in the UK. Alex, Dan, Tasha, Ben, Niamh, Victor, Chris, Tom, Vazi, Greg, Lucy, Albert and everyone else who I get to visit whenever I am home. You have all truly made me a happier and better person. I am sorry that I have done you all an injustice with such a short mention, because you deserve so much more for what you mean to me. From the bottom of my heart, thank you for every moment we have ever shared. Of course, I have to also give a shout out to the Blind Fury Monks and HUBS crew. I owe a part of my stage confidence to you guys and I can't wait to tell you about all the mad stuff I've seen and how much a scientific conference is like a cypher.

I would not be here today without Amy Ansell. You understood me and recognised a kid that just needed the right space to go a little crazy in a constructive way. You will always be an inspiration to me and thank you. Martins Arbidans, you helped me by showing me what a B-Boy is. I get to share so many experiences with an incredible community because you opened the door for me. Rohanna also deserves so much recognition for her hard work with me in my early years. I have dyslexia and dyspraxia. I struggled a lot with that as a child but thanks to all of your tutoring, I learnt strategies, understood how I think and turned it all into my strengths. I have to do a lot of writing these days, and it's all possible because of you.

I have to say my most sincere thank you to Prof. Nicole Pamme. You were the one who recommended me to Andreas and encouraged me to come to SB. I have had the experience of a lifetime, thank you. I also have to say thank you to Dr. Alex Iles, Dr. Michael Riethofer and Dr. Jia Min Chin. You all mentored me during my Bachelor and Masters projects and shaped my scientific approach so that I could complete my PhD.

Mum, Dad and Daniel. My incredible family. I truly do not have the words to ever express what you mean to me. But here's a crack at it. I am so lucky to be your son and brother. There have been so many times during my PhD where I was really struggling and frustrated and you kept me going. It means we get to share every victory, big or small, along the way. We had to go through a lot with me living abroad, a pandemic, Brexit and all sorts of unexpected difficulties. But no matter what, you were always there for me in whatever way you could be. I dearly cherish you all.

Now, I've been fortunate to have so many important people in my life and I'm so sorry if you are reading this and I missed you out. Feel free to shout at me if I did. I'm happy to have more kind words for you, but I'd like a little break from writing and catch up on some sleep.